

NASA  
TP  
1767  
c.1

NASA Technical Paper 1767

LOAN COPY:  
AFWL TECHN  
KIRTLAND AF

109470



TECH LIBRARY KAFB, NM

Experimental and Theoretical Aerodynamic  
Characteristics of Two Hypersonic  
Cruise Aircraft Concepts at Mach  
Numbers of 2.96, 3.96, and 4.63

Jimmy L. Pittman and Gregory D. Riebe

DECEMBER 1980

NASA



0134901

## NASA Technical Paper 1767

# Experimental and Theoretical Aerodynamic Characteristics of Two Hypersonic Cruise Aircraft Concepts at Mach Numbers of 2.96, 3.96, and 4.63

Jimmy L. Pittman and Gregory D. Riebe  
*Langley Research Center*  
*Hampton, Virginia*



National Aeronautics  
and Space Administration

**Scientific and Technical  
Information Branch**

1980

## SUMMARY

The longitudinal and lateral-directional aerodynamic characteristics for two Mach 5 cruise aircraft concepts have been determined for test Mach numbers of 2.96, 3.96, and 4.63. The test articles consisted of a fuselage with lenticular cross section, two geometrically similar wings, one set of horizontal tails sized for each wing, a wedge-center vertical tail, a set of fuselage-mounted twin vertical tails, a flow-through body-mounted nacelle, and a set of flow-through wing-mounted nacelles. Estimates from hypersonic impact theory and first-order supersonic linearized theory were compared with data to indicate the usefulness of these methods. The method which applied tangent-cone empirical theory to the body and tangent-wedge theory to the wings and to the horizontal and vertical tails provided the best estimates. Comparisons for the configuration buildup showed, however, that the estimates for the various components could be significantly different from the data. The tangent-cone empirical theory applied to all components showed consistently poor agreement with data, and the linear theory estimates were accurate only for lift coefficient and drag coefficient at low angles of attack.

## INTRODUCTION

Many past investigations in the hypersonic speed regime have focused on transports designed to cruise at Mach 6 to 8 (e.g., refs. 1 and 2). Liquid hydrogen is an attractive fuel for these transports primarily because its high energy content results in a greatly improved range compared with that of JP-fueled aircraft of the same gross weight. The high temperatures of this hypersonic flight regime preclude the use of conventional aluminum or titanium structures unless the maximum temperature in the load-carrying members can somehow be limited. Reference 1 discusses the merits of an actively cooled structure in relation to shielded or insulated structures for the long-duration heat loads typical of Mach 8 cruise. Although active cooling of the airframe may not be necessary, the engine will almost certainly require a circulating coolant because of the extremely high temperature in the combustor. The most efficient propulsion concept for cruise has been identified as the supersonic combustion ramjet fueled by liquid hydrogen (ref. 2). This concept would also operate in the subsonic combustion mode at off-design speeds. In addition, a turbine engine is required for subsonic-supersonic flight. The efficient integration of the turbine with the ramjet and with the airframe is one of the most difficult problems of hypersonic flight.

Recent studies have indicated that at somewhat lower cruise speeds ( $M = 5$ ), considerable vehicle design simplification is possible. One report (ref. 3) showed the feasibility of shielded and insulated structural concepts for liquid-hydrogen-fueled aircraft at a design speed of Mach 5. An important advantage of hot or insulated structures over an actively cooled structure is that the integrity of the airframe is not dependent on a mechanical system. At the lower cruise speed, the engine design is also simplified, since the supersonic combus-

tion mode of the ramjet is not necessary. Another study (ref. 4) indicated a significant reduction in airframe weight for constant range when JP fuel is stored in the wings of a liquid-hydrogen-fueled aircraft and burned in the turbojet. Therefore, several concepts for long-range cruise flight at Mach 5 have evolved. This report discusses an investigation of two of these concepts.

In order to establish the credibility of the performance estimates, the aerodynamics of the concepts must be verified experimentally. The difficulty of testing nacelle configurations which accurately simulate the spillage, exhaust pressure ratios, and exhaust plume effects of a propulsion system is well known. Therefore, because of the preliminary nature of this experiment, the test model nacelles simulated only the external lines of the study nacelles. Also, the nacelle ducts did not contract or expand.

The purpose of this investigation was to initiate an experimental data base for Mach 5 cruise aircraft concepts. A second objective was to compare appropriate analysis methods with the test data. Hypersonic impact theory and supersonic linearized theory were chosen for the comparison since both could be effective between Mach 3 and Mach 5. The tests were conducted in the Langley Unitary Plan Wind Tunnel at Mach numbers of 2.96, 3.96, and 4.63. Longitudinal and lateral force and moment data were obtained over an angle-of-attack range of  $-4^\circ$  to  $20^\circ$  at a Reynolds number of  $6.6 \times 10^6$  per meter ( $2.0 \times 10^6$  per foot).

#### SYMBOLS

The longitudinal characteristics are presented about the stability-axis system and the lateral-directional characteristics are presented about the body-axis system. The moment reference point was at a longitudinal station 61.4 percent of the fuselage length and at a vertical location 1.7 percent of the fuselage length above the reference line. Measurements and calculations were made in the U.S. Customary Units. They are presented herein in SI Units and in U.S. Customary Units.

b	wing span, cm (in.)
$C_D$	drag coefficient, Drag/qS
$C_{D,0}$	zero-lift drag coefficient
$\frac{\partial C_D}{\partial C_L^2}$	drag-due-to-lift parameter
$C_L$	lift coefficient, Lift/qS
$C_{L,0}$	lift coefficient at $\alpha = 0^\circ$
$C_{L\alpha}$	lift-curve slope, $\alpha C_L / \partial \alpha$ at $C_L = 0$ , deg $^{-1}$
$C_l$	rolling-moment coefficient, Rolling moment/qSb

$C_l\beta$	change of $C_l$ with angle of sideslip, $\frac{C_{l\beta=3^\circ} - C_{l\beta=0^\circ}}{3}$ , deg $^{-1}$
$C_{l\delta_v}$	change of $C_l$ with vertical-tail deflection, $\frac{C_{l\delta_v=5^\circ} - C_{l\delta_v=0^\circ}}{5}$ , deg $^{-1}$
$C_m$	pitching-moment coefficient, Pitching moment/qS $\ell$
$C_{m,0}$	pitching moment at $C_L = 0$
$\frac{\partial C_m}{\partial C_L}$	static margin at $C_m = 0$
$C_n$	yawing-moment coefficient, Yawing moment/qS $b$
$C_{n\beta}$	change of $C_n$ with angle of sideslip, $\frac{C_{n\beta=3^\circ} - C_{n\beta=0^\circ}}{3}$ , deg $^{-1}$
$C_{n\delta_v}$	change of $C_n$ with vertical tail deflection, $\frac{C_{n\delta_v=5^\circ} - C_{n\delta_v=0^\circ}}{5}$ , deg $^{-1}$
$C_p, \text{vac}$	vacuum pressure coefficient, $- \frac{2}{\gamma M_\infty^2}$
$C_Y$	side-force coefficient, Side force/qS
$C_{Y\beta}$	change of $C_Y$ with angle of sideslip, $\frac{C_{Y\beta=3^\circ} - C_{Y\beta=0^\circ}}{3}$ , deg $^{-1}$
$C_{Y\delta_v}$	change of $C_Y$ with vertical tail deflection, $\frac{C_{Y\delta_v=5^\circ} - C_{Y\delta_v=0^\circ}}{5}$ , deg $^{-1}$
L/D	lift-drag ratio
$l$	body length, 78.92 cm (31.07 in.)
M	Mach number
q	dynamic pressure, Pa (psia)
r	fuselage cross-sectional radius, cm (in.) (see table II)
S	reference area, cm $^2$ (in $^2$ )

x axial distance along fuselage centerline from the nose, cm (in.)  
(see table II)

y spanwise distance from plane of symmetry, cm (in.) (see table II)

z vertical distance from reference line, cm (in.) (see table II and  
fig. 2(a))

$\alpha$  angle of attack, deg

$\beta$  sideslip angle, deg

$\gamma$  ratio of specific heats (1.4 for air)

$\delta_h$  horizontal-tail deflection, deg

$\delta_v$  vertical-tail deflection, deg

$\delta_e$  toe-in angle of twin vertical tails, deg

Subscripts:

max maximum

t trim

$\infty$  free-stream conditions

Model nomenclature:

B body

$H_1$  horizontal tails sized for  $W_1$

$H_2$  horizontal tails sized for  $W_2$

$N_1$  wing-mounted flow-through nacelle for  $W_1$

$N_2$  body-mounted flow-through nacelle for  $W_2$

$V_C$  center vertical tail

$V_S$  body-mounted twin vertical tails

$W_1$  large wing

$W_2$  small wing

## MODEL DESCRIPTION

Photographs of the stainless steel wind tunnel models of the two study concepts investigated in this report are shown in figure 1. Important geometric characteristics of the various model parts are listed in table I, and a complete description of the model fuselage is contained in table II. The fuselage is

lenticular through body station  $\frac{x}{l} = 0.73$  but aft of that point, a flat surface

is imposed between the upper and lower surface circular arcs. The location of the flat surface, which begins near the intersection of the wing trailing edge and the fuselage, can be seen in figure 2. The large wing ( $W_1$ ) airfoil has a circular arc upper surface and a flat lower surface. The small wing ( $W_2$ ) airfoil and the horizontal-tail airfoils are symmetric circular arcs. The airfoil of the twin vertical tails is flat on the outboard surface and circular arc on the inboard surface. The maximum thickness location of the above-mentioned wings and tails is at 50 percent of the local chord.

The fuselage-mounted twin vertical tails were constructed in order to compare the effectiveness of this arrangement with the more conventional wedge center vertical tail. The twin vertical tails were designed by the tangent-wedge impact theory to provide the same directional stability as the wedge center vertical tail at  $M = 5$  and  $\alpha = 0^\circ$ . This simple design process indicated that a toe-in angle of  $1^\circ$  was desirable, and changes to the toe-in angle are referenced to this baseline position. The vertical tails as well as the horizontal tails are all-moving. The vertical-tail hinge lines are labeled in figure 2. The horizontal-tail hinge lines are coincident with the fuselage-tail intersection chords.

## TEST CONDITIONS

Tests were conducted in the Langley Unitary Plan Wind Tunnel at Mach numbers of 2.96, 3.96, and 4.63. The tests were conducted under the following conditions:

Mach number	Stagnation pressure		Stagnation temperature		Reynolds number	
	kPa	lb/ft <sup>2</sup>	K	°R	per meter	per foot
2.96	97.6	2039	325	585	$6.6 \times 10^6$	$2.0 \times 10^6$
3.96	173.7	3627	339	610	6.6	2.0
4.63	236.6	4941	339	610	6.6	2.0

To insure fully turbulent boundary-layer flow over the model, transition inducing strips of No. 35 sand grit (ref. 5) were applied 1.02 cm (measured

streamwise) behind the leading edge of all wings, vertical and horizontal tails, and nacelles including the nacelle ducts. These strips were also applied to the body 3.05 cm aft of the nose.

Forces and moments on the model were measured by means of a six-component strain gage balance contained within the model. The balance was connected through a supporting sting to the permanent model actuating system in the wind tunnel. Two balance cavity pressure measurements were made throughout the test program and the average of the two cavity pressures was applied to the model base area to correct the axial force to a condition of free-stream static pressure on the base. The angle of attack ranged from -4° to 20° at 0° and 3° sideslip. The angle of attack was corrected for tunnel airflow misalignment and for deflection of the sting and balance under load. No correction was made for the internal flow in the nacelle ducts.

#### PRESENTATION OF RESULTS

The results of this investigation are shown in the following figures:

#### Figure

Longitudinal aerodynamic characteristics for the configuration buildup . . . . .	3
Effect of horizontal-tail deflection on the longitudinal aerodynamic characteristics of the BW <sub>1</sub> H <sub>1</sub> V <sub>C</sub> configuration . . . . .	4
Comparison of the BW <sub>1</sub> H <sub>1</sub> V <sub>C</sub> and the BW <sub>2</sub> H <sub>2</sub> V <sub>C</sub> configurations . . . . .	5
Nacelle increments for the fuselage and wing-mounted nacelles . . . . .	6
Summary drag data for:	
Configuration buildup . . . . .	7
BW <sub>1</sub> H <sub>1</sub> V <sub>C</sub> and BW <sub>2</sub> H <sub>2</sub> V <sub>C</sub> configurations . . . . .	8
Nacelle-on and nacelle-off configurations . . . . .	9
Lateral-directional characteristics for:	
Configuration buildup . . . . .	10
BW <sub>1</sub> H <sub>1</sub> V <sub>C</sub> and BW <sub>2</sub> H <sub>2</sub> V <sub>C</sub> configurations . . . . .	11
BW <sub>1</sub> H <sub>1</sub> V <sub>C</sub> and BW <sub>1</sub> H <sub>1</sub> V <sub>S</sub> configurations . . . . .	12
Yaw control for the BW <sub>1</sub> H <sub>1</sub> V <sub>C</sub> and BW <sub>1</sub> H <sub>1</sub> V <sub>S</sub> configurations . . . . .	13
Theoretical drag polar construction . . . . .	14
Computer-generated drawing of the BW <sub>1</sub> H <sub>1</sub> V <sub>C</sub> configuration . . . . .	15
Comparison of theoretical and experimental longitudinal aerodynamic parameters for:	
B configuration . . . . .	16
BW <sub>1</sub> configuration . . . . .	17
BW <sub>1</sub> H <sub>1</sub> configuration . . . . .	18

Figure

BW <sub>1</sub> H <sub>1</sub> V <sub>C</sub> configuration . . . . .	19
BW <sub>1</sub> H <sub>1</sub> V <sub>C</sub> , $\delta_h = -10^\circ$ configuration . . . . .	20
BW <sub>1</sub> H <sub>1</sub> V <sub>C</sub> , $\delta_h = -20^\circ$ configuration . . . . .	21
Comparison of theoretical and experimental characteristics:	
Lift-curve slope with Mach number . . . . .	22
Static margin with Mach number . . . . .	23
Zero-lift drag coefficient with Mach number . . . . .	24
Maximum lift-drag ratio with Mach number . . . . .	25
Trim parameters for the BW <sub>1</sub> H <sub>1</sub> V <sub>C</sub> configuration . . . . .	26
Comparison of theoretical and experimental lateral-directional aerodynamic parameters for:	
B configuration . . . . .	27
BW <sub>1</sub> configuration . . . . .	28
BW <sub>1</sub> H <sub>1</sub> configuration . . . . .	29
BW <sub>1</sub> H <sub>1</sub> V <sub>C</sub> configuration . . . . .	30
Evaluation of supersonic linearized theory for the BW <sub>1</sub> H <sub>1</sub> V <sub>C</sub> configuration . . . . .	31
Actual and equivalent circular fuselage planforms for the BW <sub>1</sub> H <sub>1</sub> V <sub>C</sub> configuration . . . . .	32

DISCUSSION

Experimental Results

Longitudinal aerodynamic characteristics.- In figure 3, the static longitudinal aerodynamic characteristics for the BW<sub>1</sub>H<sub>1</sub>V<sub>C</sub> configuration buildup are presented. The trends of the buildup are as expected: increased  $C_{L\alpha}$  with

increased planform area, the occurrence of longitudinal stability with the addition of the wing, increased stability with addition of aft lifting area, increased  $C_{D,\alpha}$  for each added component, greatly increased  $(L/D)_{max}$  with the addition of the wing, and decreased  $(L/D)_{max}$  with subsequent component additions. The trends with increasing Mach number are also as anticipated in this Mach number range: decreased  $C_{L\alpha}$ , decreased longitudinal stability, decreased

$C_{D,\alpha}$ , decreased  $(L/D)_{max}$ , and increased  $\partial C_D / \partial C_L^2$ . The magnitudes of  $C_{m,\alpha}$  and  $C_{L,\alpha}$  are small because of the relatively flat mean camber surface.

Figure 4 presents horizontal-tail deflections for the BW<sub>1</sub>H<sub>1</sub>V<sub>C</sub> configuration, and figure 5 is a comparison of the BW<sub>1</sub>H<sub>1</sub>V<sub>C</sub> and BW<sub>2</sub>H<sub>2</sub>V<sub>C</sub> configurations. The coefficients of each concept are based on its respective wing area. Figure 6 shows the effects of the nacelles on their respective nacelle-off configurations. The coefficients are based on the reference area of  $W_1$ . Model components not needed to support the nacelles physically were removed in order to provide nacelle increments with the minimum amount of interference. Note

the large effect of  $N_1$  on the lift and pitching-moment coefficients in addition to the expected increase in drag coefficient. This effect is due to the lifting area included in this nacelle concept (see fig. 2). Figures 7, 8, and 9 show  $C_{D,0}$  and  $(L/D)_{\max}$  vs  $M$  of the configuration buildup, the  $BW_1H_1V_C$  and  $BW_2H_2V_C$  configurations, and the nacelle configurations, respectively. Note that  $BW_2H_2V_C$  attains a value of  $(L/D)_{\max}$  that is approximately one-half unit less than that of  $BW_1H_1V_C$  (see fig. 8).

Lateral-directional aerodynamic characteristics.- The lateral-directional characteristics for the configuration buildup are shown in figure 10. The wing and horizontal tail create small directionally stabilizing moments throughout the  $M$  and  $\alpha$  range, but small laterally destabilizing moments below  $\alpha = 8^\circ$ . The center vertical tail provides lateral and directional stability throughout the  $M$  and  $\alpha$  range. In figure 11, the effect of wing span on the lateral-directional characteristics is shown. The  $BW_2H_2V_C$  data plotted are based on the reference area and span of  $W_2$  and also on the reference area and span of  $W_1$ . As anticipated, the 28-percent reduction in wing span did not have a large effect on the dimensional lateral-directional characteristics.

Figure 12 compares a set of fuselage-mounted twin vertical tails with a wedge center vertical tail. The twin vertical tails were tested in the nominal position ( $1^\circ$  toe-in) and with each tail toed in an additional  $5^\circ$ . The main benefit of the twin tail arrangement is a more constant level of directional stability across the  $\alpha$  range, although the  $\delta_E = 5^\circ$  case did not differ significantly in lateral-directional characteristics from the nominal twin vertical-tail arrangement. The center vertical tail is more effective than the twin vertical tails at low  $\alpha$ , but the body-generated expansion field increasingly dominates the flow around the center vertical tail for increasing  $\alpha$ ; a loss of directional stability consequently results. Figure 7 shows the center vertical tail to have a slightly greater  $C_{D,0}$  than the twin vertical tails at  $M = 2.96$  and  $3.96$ , but the  $C_{D,0}$  penalty vanishes at  $M = 4.63$ . However, the  $(L/D)_{\max}$  of  $BW_1H_1V_C$  approximately equals or exceeds that of  $BW_1H_1V_S$  which indicates that the outward canted twin vertical tails provide an increment in lift and drag due to lift to the  $BW_1H_1$  configuration. The lateral-directional characteristics caused by a vertical-tail deflection of  $5^\circ$  are shown in figure 13 for both twin vertical tail (the leading edge of both tails deflected in the same direction) and center vertical-tail arrangements. The magnitudes of the derivatives are approximately equal for both vertical-tail arrangements.

#### Theoretical Methods

The integrated supersonic linear-theory analysis code identified as the Boeing program (refs. 6, 7, and 8) was selected for comparison with data. This program is based on the technology developed at the Langley Research Center (LaRC) (refs. 9 and 10) combined with the Sommer and Short skin friction method (ref. 11); the Boeing program however, contains several useful extensions of the basic methods. Some of the extensions are addition of a near-field (thickness pressure) wave drag program, an improved lift analysis program which provides for separate modeling of fuselage lift, and the addition of expansion pressure limiting to constrain the linear theory solution. The following Boeing program options were selected for the  $BW_1H_1$  lift analysis: the effect of the

fuselage upwash field on the wing and horizontal tails, the effect of wing downwash on the fuselage and horizontal tails, the asymmetric body volume term, and the smoothing-as-computed pressures. In addition, the linear theory results presented in the body of this paper are constrained to an upper surface pressure limit of 0.7 vacuum pressure coefficient. This constraint accounts for the non-linearity of the  $C_L$  and  $C_m$  estimates. The linear theory drag polar construction is illustrated in figure 14(a). A more thorough discussion of linear theory methods is included in the appendix.

Two impact theories found in references 12 and 13 are also evaluated. The tangent-cone empirical theory is applied to all configuration components and compared with data. The tangent-cone empirical calculation in references 12 and 13 has been significantly improved by C. L. W. Edwards of LaRC (see appendix of ref. 14) and has been substituted into the computer code. Furthermore, the tangent-cone empirical theory is applied to the fuselage; the tangent-wedge theory is applied to the wing, horizontal tail, and vertical tail; and the summation is compared with data. Expansion fields are calculated by the Prandtl-Meyer theory with the minimum expansion limited to 0.7 vacuum pressure coefficient. The skin friction calculation is that of Spalding and Chi (ref. 15), which is included in the computer program of references 12 and 13. The hypersonic impact theory drag polar is shown in figure 14(b). The numerical representation of the wind tunnel model geometry was specified according to the method of reference 16 and additional coding is available to translate the surface geometry to the appropriate input format for each particular computer program. A computer-generated three-view drawing from the program of reference 16 for the  $BW_1H_1V_C$  configuration is shown in figure 15.

#### COMPARISON OF DATA WITH THEORY

##### Longitudinal Characteristics

Figures 16 to 19 compare configuration buildup data with tangent-cone theory and with tangent-cone/tangent-wedge theory. Also, the supersonic linearized theory is shown in figure 19 for comparison with  $BW_1H_1V_C$ .

Figure 16 shows that the tangent-cone theory inadequately predicts the body-alone characteristics. For  $\alpha > 4^\circ$ , the lift and drag are overpredicted; this condition probably results from pressure bleed around the edge of the body. At  $M = 4.63$ , the tangent-cone estimate improves visibly, which is an indication that the flow more nearly satisfies impact theory assumptions. It might be presumed that the slenderness and nonconical aspects of the body contribute to the inaccuracy of the tangent-cone estimate.

The tangent-cone predictions of the  $BW_1$ ,  $BW_1H_1$ , and  $BW_1H_1V_C$  aerodynamics (figs. 17, 18, and 19) are also rather poor, but the error occurs in the opposite direction from that of the B estimate. It can be inferred from these comparisons that the tangent-cone pressures on the relatively flat lifting surfaces are much lower than the actual compression pressures on these surfaces. The tangent-wedge estimate for the wing, when added to the tangent-cone estimate for the body, produces good results. This same trend holds for the rest of the configuration buildup (figs. 18 and 19). The tangent-wedge pressures, which are

greater than those for the tangent-cone for equivalent conditions, also seem to be somewhat less than the actual pressures, since the large overpredictions from tangent-cone theory for the body are not maintained with component additions.

The linear theory estimates presented in figure 19 are generally poor, especially at the high angles of attack where the small angle and small disturbance assumptions are not valid. The use of upper surface pressure limiting resulted in significant degradation in the agreement of data with theory (see appendix). The nonlinearity of the  $C_L$  and  $C_m$  estimates results from upper surface pressure limiting. Since the upper surface pressures are constrained to physical realism, the error in the linear theory estimates seems to result from underestimation of compression surface pressures. Supporting evidence for this statement can be found in reference 17, which presents static pressure data and supersonic linear theory estimates for several delta wings at high supersonic Mach numbers.

Figures 20 and 21 present data and estimates from supersonic linear theory and the tangent-cone/tangent-wedge analysis for horizontal-tail deflections of  $-10^\circ$  and  $-20^\circ$ , respectively. The comments for figure 19 apply to these figures as well, except that the agreement with the tangent-cone/tangent-wedge prediction is visibly degraded for the  $-20^\circ$  case. Figures 22 to 25 are summary comparison plots for the configuration buildup. These figures tend to confirm the superiority of the tangent-cone/tangent-wedge estimates over those obtained from tangent-cone and supersonic linear theory, although the tangent-cone/tangent-wedge method must be used with caution for any level of analysis beyond preliminary design. It should be noted that the value of the skin friction drag obtained from Spalding-Chi (ref. 15) is greater than that obtained from Sommer and Short (ref. 11), the disparity increasing with increasing Mach number. Substitution of the Spalding-Chi skin friction value for the Sommer and Short value in the linear theory analysis would improve the linear theory estimates of  $C_{D,0}$  and  $(L/D)_{\max}$ .

Figure 26 compares data and theory trim parameters. The tangent-cone/tangent-wedge analysis predicts that horizontal-tail deflection will provide a much wider range of trimmable  $C_L$  than the data suggest. The linear theory trend is for a smaller than actual trimmable  $C_L$  range and for lower values of  $C_L$  at the same horizontal-tail deflection. The discrepancy between data and estimate is greatest for the  $-20^\circ$  case, where the possibility of separated flow on the horizontal tail is quite likely.

#### Lateral-Directional Characteristics

Figures 27 to 30 show comparisons of lateral-directional data and impact theory for the configuration buildup. Generally, the proper sign of the parameter is predicted, but the magnitudes are seldom correct. The error in the estimate tends to decrease with increasing Mach number. Note that the theoretical curves for  $BW_1$  and  $BW_1H_1$  (figs. 28 and 29) are coincident, since neither the wing nor the horizontal-tail contributes significantly to the lateral-directional characteristics. As can be seen by comparing figures 27 and 28, the addition of the wing creates no change in the predicted  $C_{nq}$ ; the experimental data, however, show that the wing produces a directionally stabilizing moment and a laterally stabilizing moment at angles of attack greater than  $8^\circ$ .

The effect of the wing is artificially reduced in the impact analysis because each element is assumed to act independently in free-stream flow; i.e., no interference effects are computed. For the BW<sub>1</sub>H<sub>1</sub>V<sub>C</sub> configuration the two impact theory estimates show large differences with each other. For all three Mach numbers, the tangent-cone/tangent-wedge estimate at  $\alpha = 0^\circ$  corresponds to the data although the agreement is not maintained with increasing  $\alpha$ . This error at the higher angles of attack results because the impact theory analysis does not account for the body-generated expansion field which engulfs the vertical tail and reduces its effectiveness.

#### CONCLUSIONS

The longitudinal and lateral-directional aerodynamic characteristics for two Mach 5 cruise aircraft concepts have been determined for test Mach numbers of 2.96, 3.96, and 4.63. The model components consisted of a fuselage with lenticular cross section, two geometrically similar wings, one set of horizontal tails sized for each wing, a wedge center vertical tail, a set of fuselage-mounted twin vertical tails, a flow-through body-mounted nacelle, and a set of flow-through wing-mounted nacelles. Estimates from hypersonic impact theory and supersonic linearized theory are presented for several of the test configurations without nacelles. The following conclusions can be drawn from this study:

1. The method of analysis which applied tangent-cone empirical theory to the fuselage and tangent-wedge theory to the wing, horizontal tail, and vertical tail provided very good overall agreement with data, but the estimates of the aerodynamics of the individual components were often significantly different from the data.
2. The tangent-cone empirical theory applied to all configuration components provided generally poor estimates. The estimates from first-order supersonic linearized theory were also poor, the only areas of good agreement being for lift coefficient and drag coefficient at low angles of attack.
3. Both the wedge center vertical tail and the body-mounted twin vertical tails provided lateral-directional stability in the test range of Mach number and angle of attack. However, the body-mounted twin vertical tails provided more uniform lateral-directional characteristics with angle of attack than the wedge center vertical tail.
4. The maximum lift-drag ratio of the configuration with the center vertical tail was approximately equal to or greater than that of the same configuration with the twin vertical tails.

Langley Research Center  
National Aeronautics and Space Administration  
Hampton, VA 23665  
October 3, 1980

## APPENDIX

### EVALUATION OF TWO SUPERSONIC LINEARIZED THEORY METHODS

One method of supersonic flow analysis for arbitrary shapes consists of three independent computer codes based on references 9, 10, and 11. Specifically, the three programs are a zero-lift far-field wave drag analysis which combines the supersonic area rule with slender-body theory (ref. 9), a zero volume lift analysis method (ref. 10), and an empirical skin friction calculation (ref. 11). Each program provides a portion of the drag estimate (see fig. 14(a)), while the total lift and pitching-moment estimates are calculated in the lift analysis code. (The lift and pitching-moment increments due to vertical surfaces are not calculated.) This same methodology is the basis for the integrated program of references 6, 7, and 8, which is referred to as the Boeing program. The zero-lift far-field wave drag code and the empirical skin friction code are essentially those of the first method, but the Boeing program provides several advantages over the independent lift analysis code. These advantages are internal generation of a wing-body/vertical-tail camber surface, lifting analysis of an equivalent circular fuselage using slender-body theory, optional fuselage buoyancy field for low- or high-wing configurations, optional application of an upper surface pressure limit, and a zero-lift near-field wave drag analysis which provides the thickness pressures required for pressure limiting.

Figure 31 presents a comparison of data for the BW<sub>1</sub>H<sub>1</sub>V<sub>C</sub> configuration and theory from both the independent (curve A) and Boeing programs. Boeing program estimates are shown for several different methods of input. The first Boeing program estimate (curve B) is for the camber surface input required by the independent lift analysis code. These two linear theory estimates agree with each other and with the data except for the more negative prediction of pitching moment. The reason for the disparity in the pitching-moment estimates from the two programs is not known. An improved estimate should be obtained with an actual surface input (curve C), since the modeling of the fuselage allows body volume effects to be assessed. However, the figure shows that these results are substantially worse than those obtained from a camber surface input. The reason for this discrepancy was found to be due to configuration planform changes which occur when the arbitrary fuselage is converted to an equivalent circular fuselage for slender-body analysis. This conversion occurs internally in the Boeing lift analysis code and is not readily apparent to the user. However, significant planform changes can occur for arbitrary fuselage cross sections as is shown in figure 32. A means of alleviating this problem is to modify the wing input so that it accurately models the actual fuselage-wing planform. The Boeing program estimate utilizing the actual surface input with a modified wing (curve D) is shown in figure 31. The lift and drag estimates are greatly improved, but the pitching-moment estimate is actually degraded.

The estimates presented to this point have lacked one aspect of physical realism; specifically, linearized theory provides no limit on attainable expansion pressures. It is known that under certain Mach number and angle-of-attack combinations, the predicted upper surface pressures can actually be less than vacuum while the real flow generally does not expand beyond 70 to 80 percent of

## APPENDIX

vacuum. The nonlinear lift and pitching-moment estimates (curve E) in figure 31 result because the calculated upper surface pressure coefficients must be greater than  $0.7C_{p,\text{vac}}$  on the actual surface-modified wing input previously discussed. Although the pressure limited linear theory estimate of lift and drag does not agree with data as well as the unlimited case, the flow behavior is physically more realistic. The disagreement with experiment is not unexpected since previous work (ref. 17) has shown that linear theory also tends to underestimate the compression surface pressures at the higher Mach numbers and at high angles of attack.

#### REFERENCES

1. Becker, John V.: New Approaches to Hypersonic Aircraft. Paper presented at the Seventh Congress of the International Council of the Aeronautical Sciences (Rome, Italy), Sept. 1970.
2. Kirkham, Frank S.; and Hunt, James L.: Hypersonic Transport Technology. *Acta Astronaut.*, vol. 4, no. 1/2, Jan./Feb. 1977, pp. 181-199.
3. Taylor, Allan H.; and Jackson, L. Robert: Thermostructural Analyses of Structural Concepts for Hypersonic Cruise Vehicles. AIAA-80-0407, Jan. 1980.
4. Weidner, John P.: The Application of Dual Fuel (JP-LH<sub>2</sub>) for Hypersonic Cruise Vehicles. *J. Aircr.*, vol. 15, no. 10, Oct. 1978, pp. 686-691.
5. Braslow, Albert L.; Hicks, Raymond M.; and Harris, Roy V., Jr.: Use of Grit-Type Boundary-Layer-Transition Trips on Wind-Tunnel Models. NASA TN D-3579, 1966.
6. Middleton, W. D.; and Lundry, J. L.: A Computational System for Aerodynamic Design and Analysis of Supersonic Aircraft. Part 1 - General Description and Theoretical Development. NASA CR-2715, 1976.
7. Middleton, W. D.; Lundry, J. L.; and Coleman, R. G.: A Computational System for Aerodynamic Design and Analysis of Supersonic Aircraft. Part 2 - User's Manual. NASA CR-2716, 1976.
8. Middleton, W. D.; Lundry, J. L.; and Coleman, R. G.: A Computational System for Aerodynamic Design and Analysis of Supersonic Aircraft. Part 3 - Computer Program Description. NASA CR-2717, 1976.
9. Harris, Roy V., Jr.: An Analysis and Correlation of Aircraft Wave Drag. NASA TM X-947, 1964.
10. Carlson, Harry W.; and Miller, David S.: Numerical Methods for the Design and Analysis of Wings at Supersonic Speeds. NASA TN D-7713, 1974.
11. Sommer, Simon C.; and Short, Barbara J.: Free-Flight Measurements of Turbulent-Boundary-Layer Skin Friction in the Presence of Severe Aerodynamic Heating at Mach Numbers From 2.8 to 7.0. NACA TN 3391, 1955.
12. Gentry, Arvel E.: Hypersonic Arbitrary-Body Aerodynamic Computer Program (Mark III Version). Vol. I - User's Manual. Rep. DAC 61552, Vol. I (Air Force Contract Nos. F33615 67 C 1008 and F33615 67 C 1602), McDonnell Douglas Corp., Apr. 1968. (Available from DTIC as AD 851 811.)
13. Gentry, Arvel E.; and Smyth, Douglas N.: Hypersonic Arbitrary-Body Aerodynamic Computer Program (Mark III Version). Vol. II - Program Formulation and Listings. Rep. DAC 61552, Vol. II (Air Force Contract Nos. 33615 67 C 1008 and F33615 67 C 1602), McDonnell Douglas Corp., Apr. 1968. (Available from DTIC as AD 851 812.)

14. Pittman, Jimmy L. (appendix by C. L. W. Edwards): Application of Supersonic Linear Theory and Hypersonic Impact Methods to Three Nonslender Hypersonic Airplane Concepts at Mach Numbers From 1.10 to 2.86. NASA TP-1539, 1979.
15. Spalding, D. B.; and Chi, S. W.: The Drag of a Compressible Turbulent Boundary Layer on a Smooth Flat Plate With and Without Heat Transfer. J. Fluid Mech., vol. 18, pt. 1, Jan. 1964, pp. 117-143.
16. Stack, Sharon, H.; Edwards, C. L. W.; and Small, William J.: GEMPAK: An Arbitrary Aircraft Geometry Generator. NASA TP-1022, 1977.
17. Sorrells, Russell B., III; and Landrum, Emma Jean: Theoretical and Experimental Study of Twisted and Cambered Delta Wings Designed for a Mach Number of 3.5. NASA TN D-8247, 1976.

TABLE I.- GEOMETRIC CHARACTERISTICS OF THE WIND TUNNEL COMPONENTS

Fuselage:

Length, cm (in.) . . . . .	78.92 (31.07)
Maximum height, cm (in.) . . . . .	4.11 (1.62)
Maximum width, cm (in.) . . . . .	8.48 (3.34)
Fineness ratio of equivalent round body . . . . .	14.20
Planform area, $\text{cm}^2$ ( $\text{in}^2$ ) . . . . .	471.87 (73.14)
Wetted area:	
Without components or base, $\text{cm}^2$ ( $\text{in}^2$ ) . . . . .	1150.97 (178.40)
With $W_1$ , $H_1$ , $V_C$ on (no base), $\text{cm}^2$ ( $\text{in}^2$ ) . . . . .	1116.51 (173.06)
Base area, $\text{cm}^2$ ( $\text{in}^2$ ) . . . . .	15.42 (2.39)

$W_1$ :

Planform area including the fuselage intercept, $\text{cm}^2$ ( $\text{in}^2$ ) . . .	594.32 (92.12)
Exposed planform area, $\text{cm}^2$ ( $\text{in}^2$ ) . . . . .	408.39 (63.30)
Wetted area, $\text{cm}^2$ ( $\text{in}^2$ ) . . . . .	841.68 (130.46)
Span, cm (in.) . . . . .	37.03 (14.58)
Aspect ratio . . . . .	2.31
Root chord at fuselage center line, cm (in.) . . . . .	26.04 (10.25)
Tip chord, cm (in.) . . . . .	6.07 (2.39)
Total area mean aerodynamic chord, cm (in.) . . . . .	18.14 (7.14)
Taper ratio . . . . .	0.23
Leading-edge sweepback angle, deg . . . . .	55.0
Trailing-edge sweepback angle, deg . . . . .	20.0
Dihedral angle, deg . . . . .	0.0
Incidence angle, deg . . . . .	0.0
Airfoil thickness ratio . . . . .	0.035
Leading-edge radius, cm (in.) . . . . .	0.013 (0.005)

$W_2$ :

Planform area including the fuselage intercept, $\text{cm}^2$ ( $\text{in}^2$ ) . . .	310.32 (48.10)
Exposed planform area, $\text{cm}^2$ ( $\text{in}^2$ ) . . . . .	177.87 (27.57)
Wetted area, $\text{cm}^2$ ( $\text{in}^2$ ) . . . . .	357.23 (55.37)
Span, cm (in.) . . . . .	26.77 (10.54)
Aspect ratio . . . . .	2.31
Root chord at fuselage centerline, cm (in.) . . . . .	18.80 (7.40)
Tip chord, cm (in.) . . . . .	4.39 (1.73)
Total area mean aerodynamic chord, cm (in.) . . . . .	13.08 (5.15)
Taper ratio . . . . .	0.23
Leading-edge sweepback angle, deg . . . . .	55.0
Trailing-edge sweepback angle, deg . . . . .	20.0
Dihedral angle, deg . . . . .	0.0
Incidence angle, deg . . . . .	0.0
Airfoil thickness ratio . . . . .	0.035
Leading-edge radius, cm (in.) . . . . .	0.013 (0.005)

TABLE I.- Continued

 $H_1$ :

Exposed planform area, $\text{cm}^2$ ( $\text{in}^2$ ) . . . . .	59.03 (9.15)
Wetted area, $\text{cm}^2$ ( $\text{in}^2$ ) . . . . .	118.64 (18.39)
Span, $\text{cm}$ (in.) . . . . .	14.27 (5.62)
Root chord at fuselage intersection, $\text{cm}$ (in.) . . . . .	8.48 (3.34)
Tip chord, $\text{cm}$ (in.) . . . . .	3.91 (1.54)
Taper ratio . . . . .	0.46
Leading-edge sweepback angle, deg . . . . .	55.0
Trailing-edge sweepback angle, deg . . . . .	20.0
Dihedral angle, deg . . . . .	9.0
Incidence angle, deg . . . . .	0.0
Airfoil thickness ratio . . . . .	0.040
Leading-edge radius, $\text{cm}$ (in.) . . . . .	0.013 (0.005)

 $H_2$ :

Exposed planform area, $\text{cm}^2$ ( $\text{in}^2$ ) . . . . .	42.13 (6.53)
Wetted area, $\text{cm}^2$ ( $\text{in}^2$ ) . . . . .	86.19 (13.36)
Span, $\text{cm}$ (in.) . . . . .	12.75 (5.02)
Root chord at fuselage intersection, $\text{cm}$ (in.) . . . . .	7.26 (2.86)
Tip chord, $\text{cm}$ (in.) . . . . .	3.51 (1.38)
Taper ratio . . . . .	0.48
Leading-edge sweepback angle, deg . . . . .	55.0
Trailing-edge sweepback angle, deg . . . . .	20.0
Dihedral angle, deg . . . . .	9.0
Incidence angle, deg . . . . .	0.0
Airfoil thickness ratio . . . . .	0.040
Leading-edge radius, $\text{cm}$ (in.) . . . . .	0.013 (0.005)

 $V_C$ :

Exposed profile area, $\text{cm}^2$ ( $\text{in}^2$ ) . . . . .	69.81 (10.82)
Wetted area, $\text{cm}^2$ ( $\text{in}^2$ ) . . . . .	141.23 (21.89)
Maximum height above root chord, $\text{cm}$ (in.) . . . . .	8.00 (3.15)
Root chord at fuselage intersection, $\text{cm}$ (in.) . . . . .	12.98 (5.11)
Tip chord, $\text{cm}$ (in.) . . . . .	4.47 (1.76)
Taper ratio . . . . .	0.34
Leading-edge sweepback angle, deg . . . . .	55.0
Trailing-edge sweepback angle, deg . . . . .	20.0
Leading-edge wedge angle, deg . . . . .	6.0
Airfoil thickness ratio . . . . .	0.105
Leading-edge radius, $\text{cm}$ (in.) . . . . .	0.013 (0.005)
Projected base area, $\text{cm}^2$ ( $\text{in}^2$ ) . . . . .	7.29 (1.13)

TABLE I.- Concluded

 $V_S$ :

Exposed profile area (each), $\text{cm}^2$ ( $\text{in}^2$ ) . . . . .	44.65 (6.92)
Wetted area (both), $\text{cm}^2$ ( $\text{in}^2$ ) . . . . .	183.03 (28.37)
Maximum height above root chord, $\text{cm}$ ( $\text{in.}$ ) . . . . .	6.73 (2.65)
Root chord at fuselage intersection, $\text{cm}$ ( $\text{in.}$ ) . . . . .	10.13 (3.99)
Tip chord, $\text{cm}$ ( $\text{in.}$ ) . . . . .	2.84 (1.12)
Taper ratio . . . . .	0.28
Leading-edge sweepback angle, deg . . . . .	55.7
Trailing-edge sweepback angle, deg . . . . .	20.4
Cast-out angle measured from the vertical, deg . . . . .	15.0
Toe-in angle measured from the plane of symmetry, deg . . . . .	1.0
Airfoil thickness ratio . . . . .	0.030
Leading-edge radius, $\text{cm}$ ( $\text{in.}$ ) . . . . .	0.013 (0.005)

 $N_1$  (both):

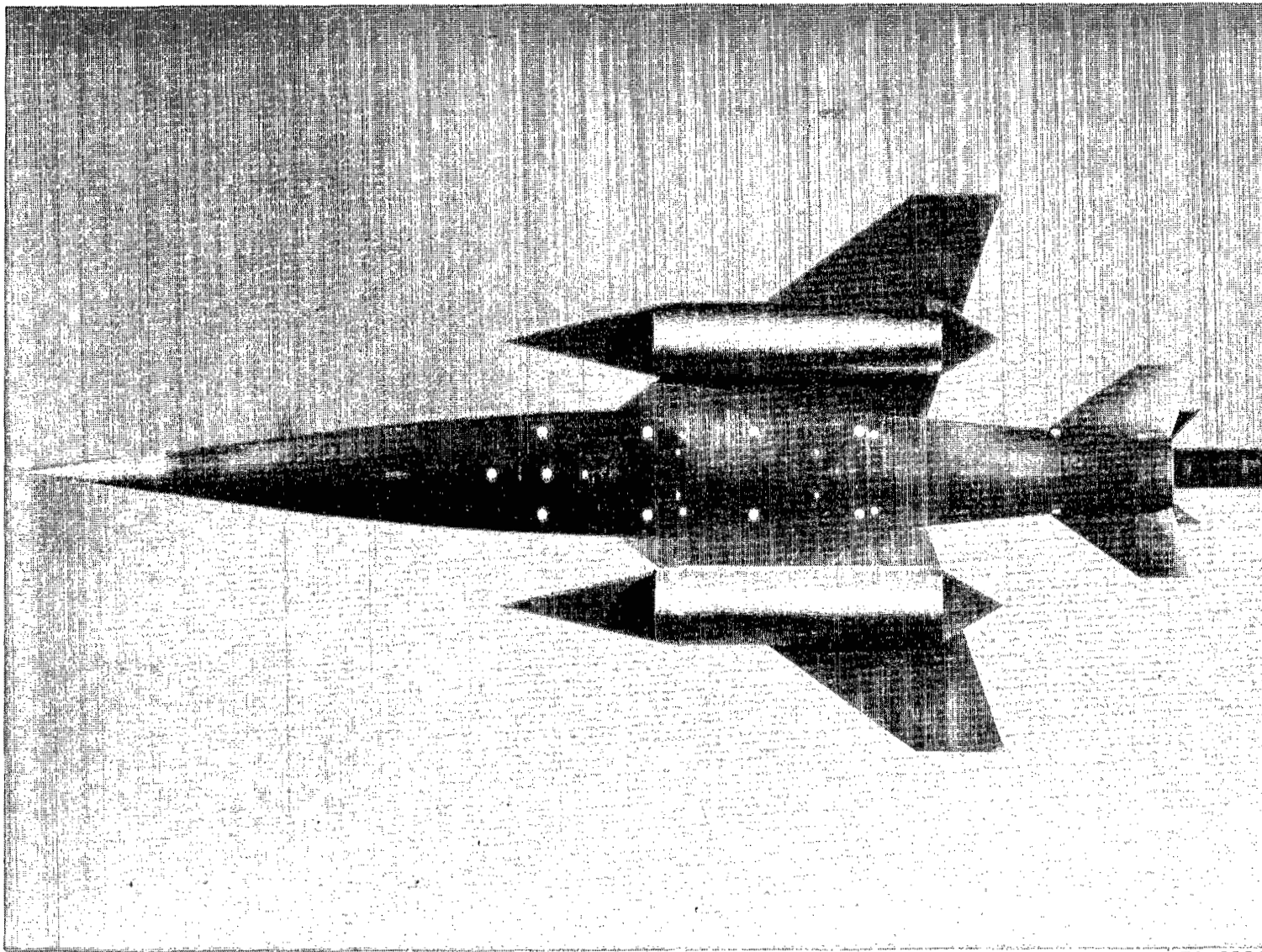
External wetted area, $\text{cm}^2$ ( $\text{in}^2$ ) . . . . .	519.68 (80.55)
Internal wetted area, $\text{cm}^2$ ( $\text{in}^2$ ) . . . . .	478.06 (74.10)
Projected inlet area, $\text{cm}^2$ ( $\text{in}^2$ ) . . . . .	17.94 (2.78)
Projected base area, $\text{cm}^2$ ( $\text{in}^2$ ) . . . . .	1.87 (0.29)
Area of wing covered by the nacelles, $\text{cm}^2$ ( $\text{in}^2$ ) . . . . .	173.16 (26.84)

 $N_2$ :

External wetted area, $\text{cm}^2$ ( $\text{in}^2$ ) . . . . .	140.97 (21.85)
Internal wetted area, $\text{cm}^2$ ( $\text{in}^2$ ) . . . . .	171.94 (26.65)
Projected inlet area, $\text{cm}^2$ ( $\text{in}^2$ ) . . . . .	6.65 (1.03)
Projected base area, $\text{cm}^2$ ( $\text{in}^2$ ) . . . . .	2.26 (0.35)
Area of fuselage covered by the nacelle, $\text{cm}^2$ ( $\text{in}^2$ ) . . . . .	62.06 (9.62)

TABLE II.- FUSELAGE COORDINATES

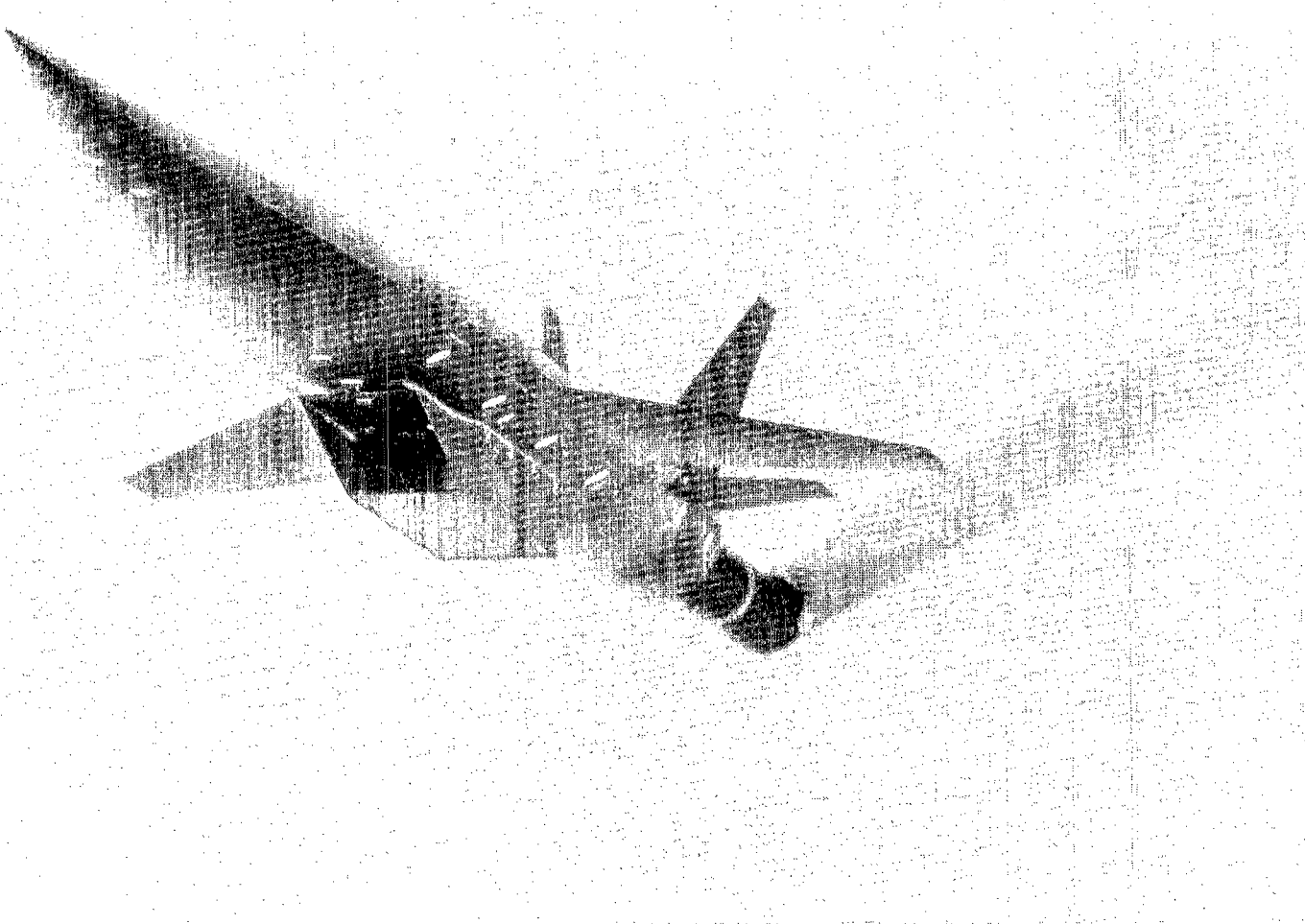
$x/l$	$r_{upper}/l$	$r_{lower}/l$	$z_{upper}/l$ at $y = 0$	$z_{lower}/l$ at $y = 0$	$y_{max}/l$	$z/l$ at $y_{max}/l$
0	0	0	0.0325	0.0325	0	0.0325
.0858	.0123	.0189	.0358	.0204	.0122	.0249
.1502	.0212	.0333	.0383	.0132	.0209	.0206
.2146	.0306	.0483	.0408	.0078	.0296	.0179
.2790	.0394	.0624	.0433	.0040	.0373	.0164
.3434	.0467	.0741	.0458	.0020	.0438	.0154
.4077	.0527	.0821	.0483	.0	.0486	.0159
.4721	.0572	.0889	.0505	.0	.0521	.0169
.5365	.0588	.0923	.0518	.0	.0536	.0172
.6009	.0586	.0923	.0520	.0	.0536	.0172
.6652	.0567	.0883	.0520	.0	.0523	.0172
.7296	.0525	.0797	.0520	.0	.0494	.0172
.7940	.0480	.0658	.0520	.0	.0447	.0175
.8584	.0473	.0461	.0520	.0	.0386	.0209
.8926	.0480	.0389	.0520	.0	.0362	.0248
.9227	.0472	.0355	.0520	.0	.0345	.0269
.9493	.0448	.0332	.0520	.0	.0330	.0298
.9742	.0415	.0319	.0520	.0	.0319	.0319
1.0	.0371	.0307	.0520	.0	.0307	.0307



L-79-8113

(a) Configuration BW<sub>1</sub>H<sub>1</sub>V<sub>S</sub>N<sub>1</sub>.

Figure 1.- Photographs of wind tunnel models.



L-79-8248

(b) Configuration  $BW_2H_2VSN_2$ .

Figure 1.- Concluded.

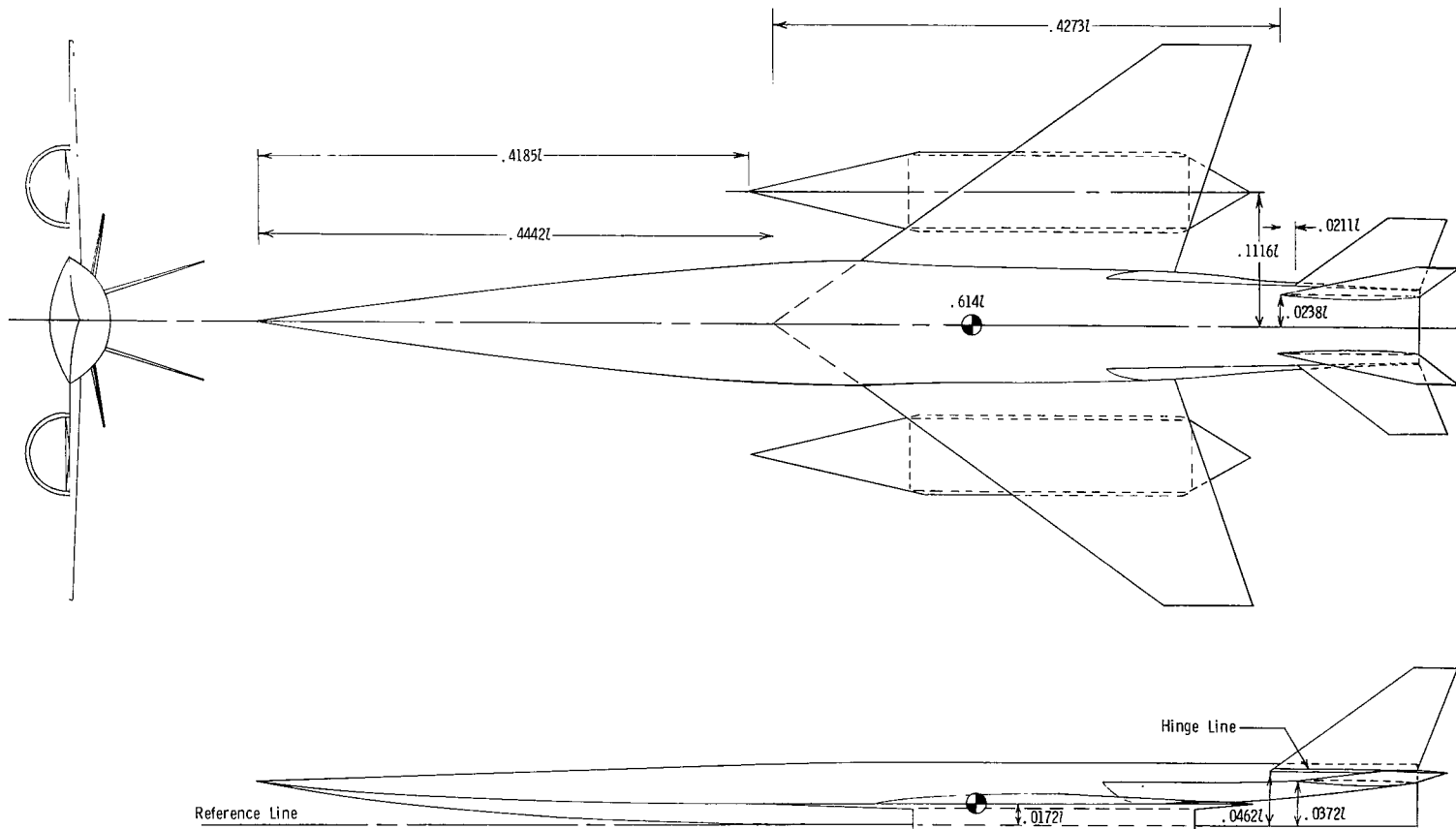
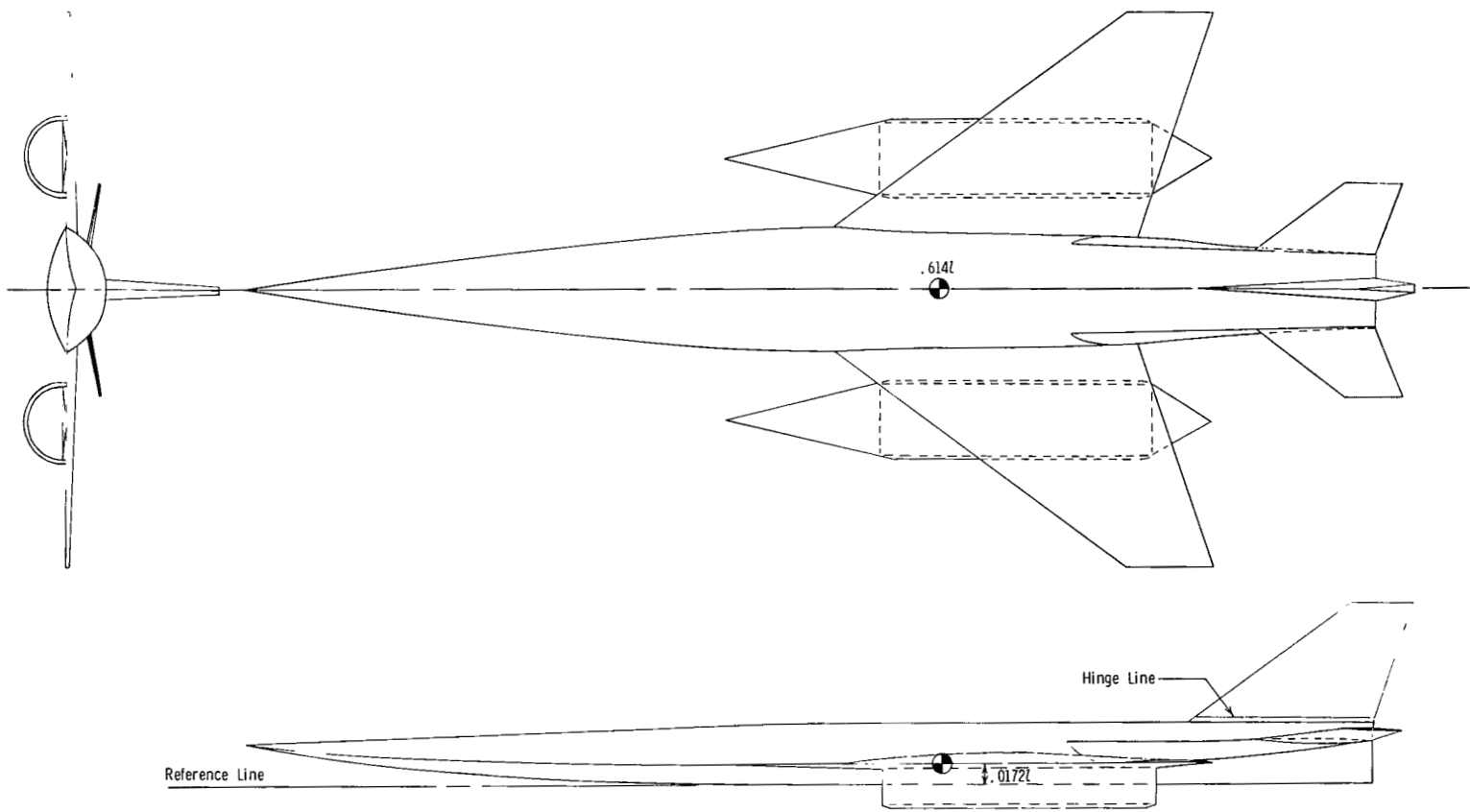
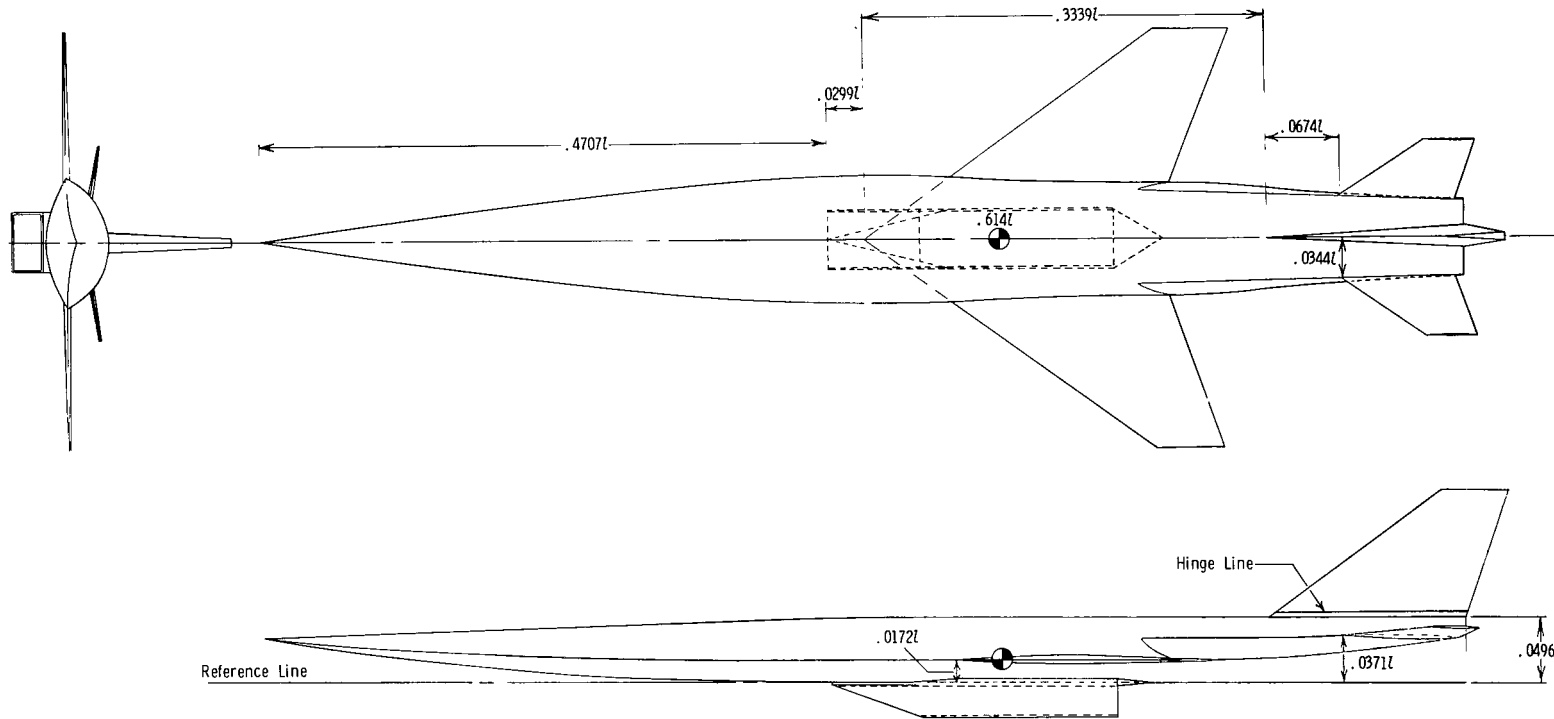
(a) BW<sub>1</sub>H<sub>1</sub>VSN<sub>1</sub>.

Figure 2.- Three-view drawings of configurations.



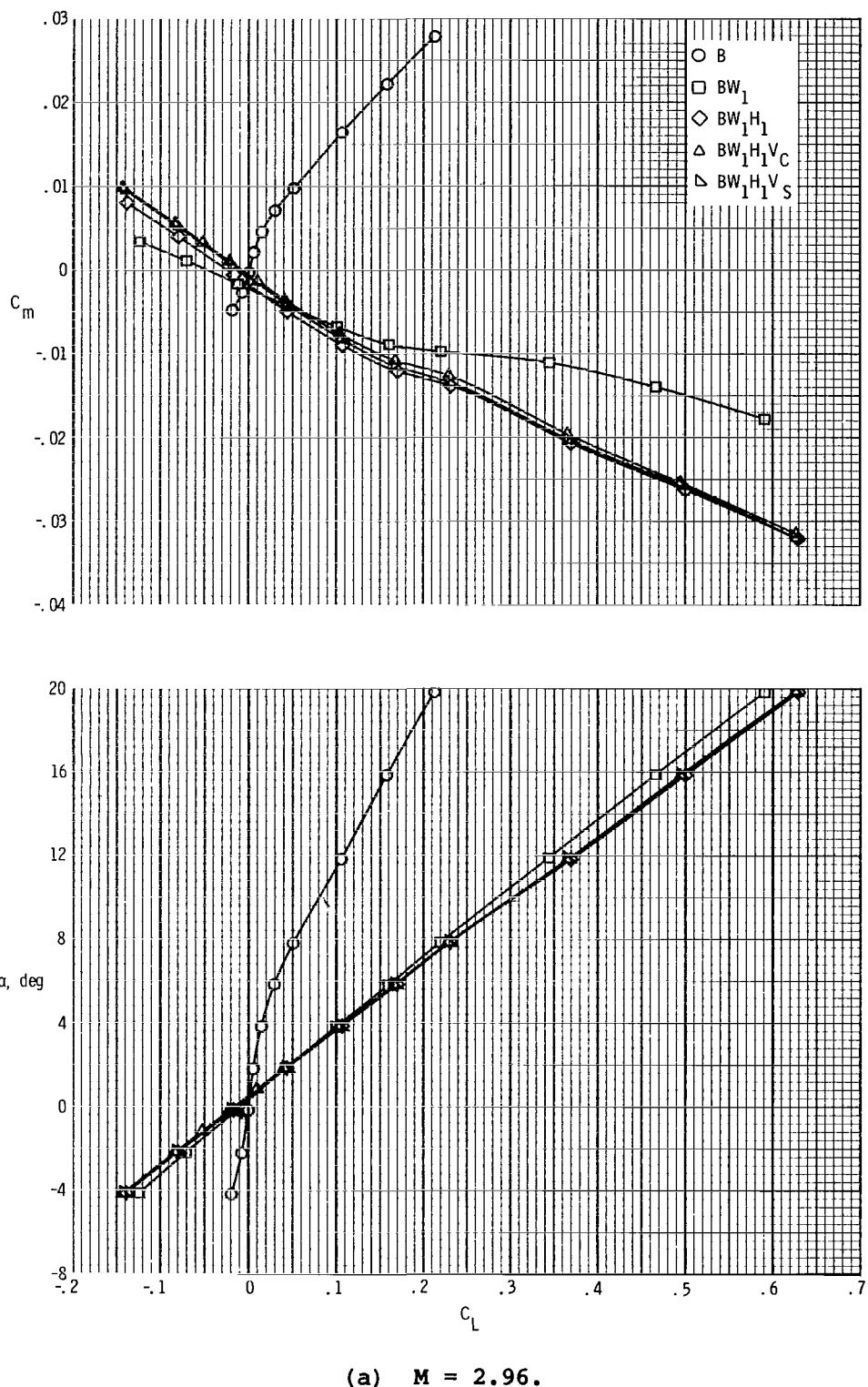
(b)  $BW_1H_1V_CN_1$ .

Figure 2.- Continued.



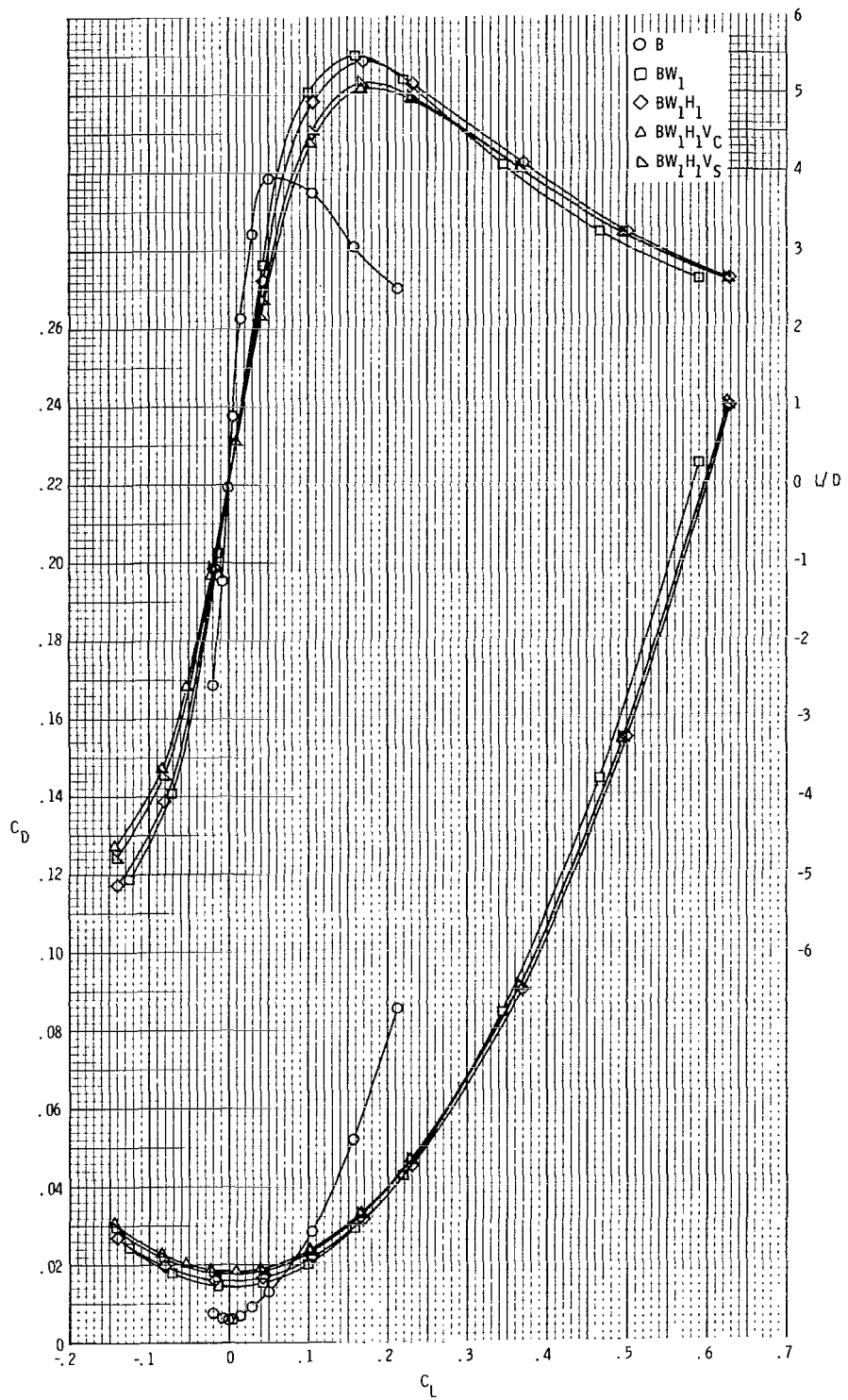
(c) BW<sub>2</sub>H<sub>2</sub>V<sub>C</sub>N<sub>2</sub>.

Figure 2.- Concluded.



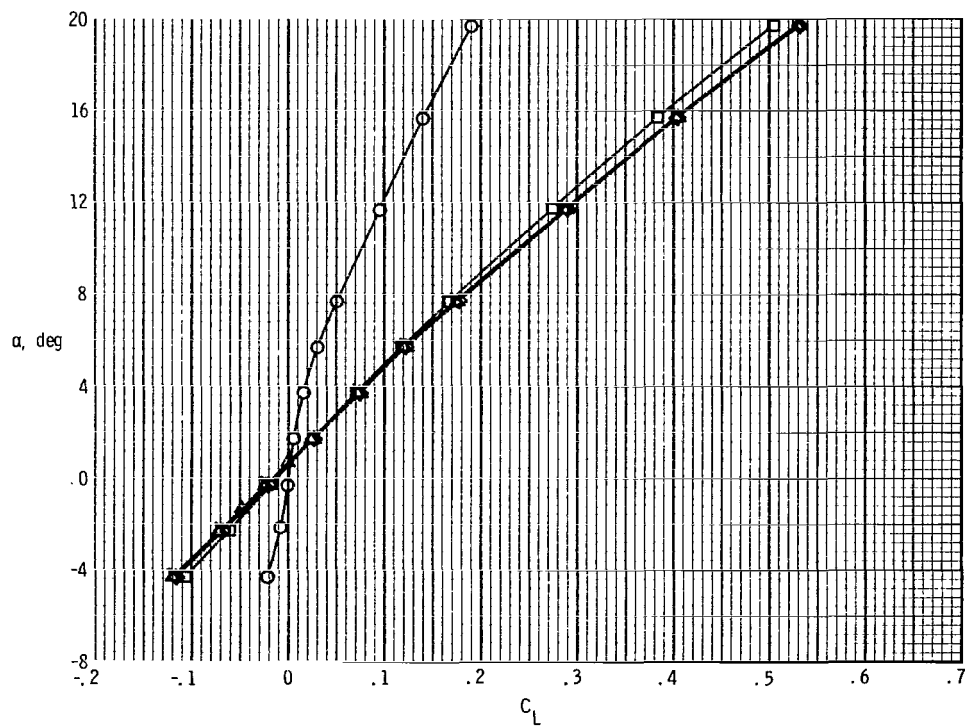
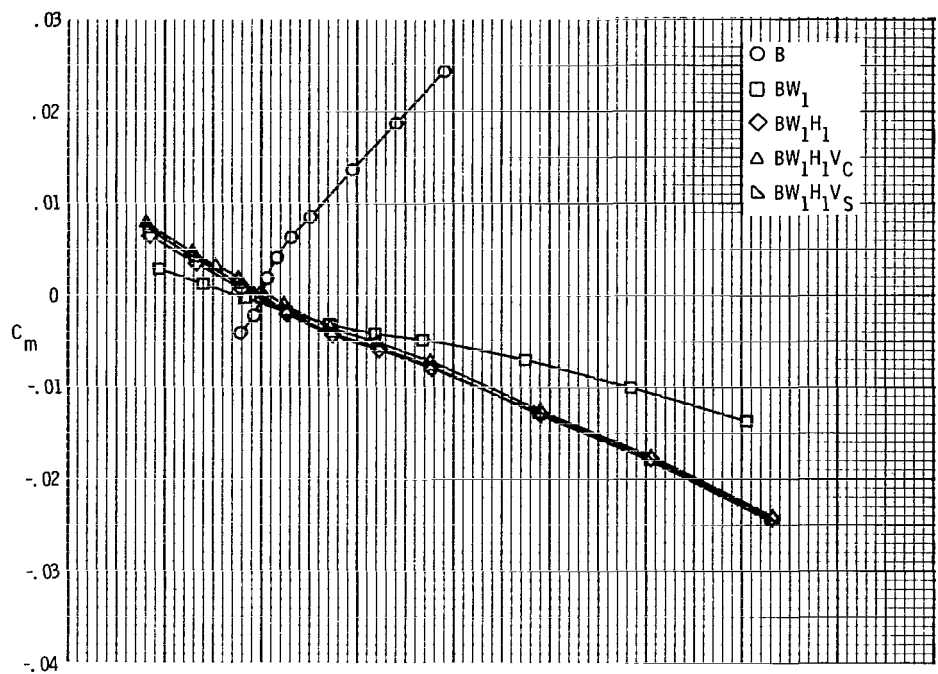
(a)  $M = 2.96.$

**Figure 3.- Longitudinal aerodynamic characteristics for configuration buildup.**



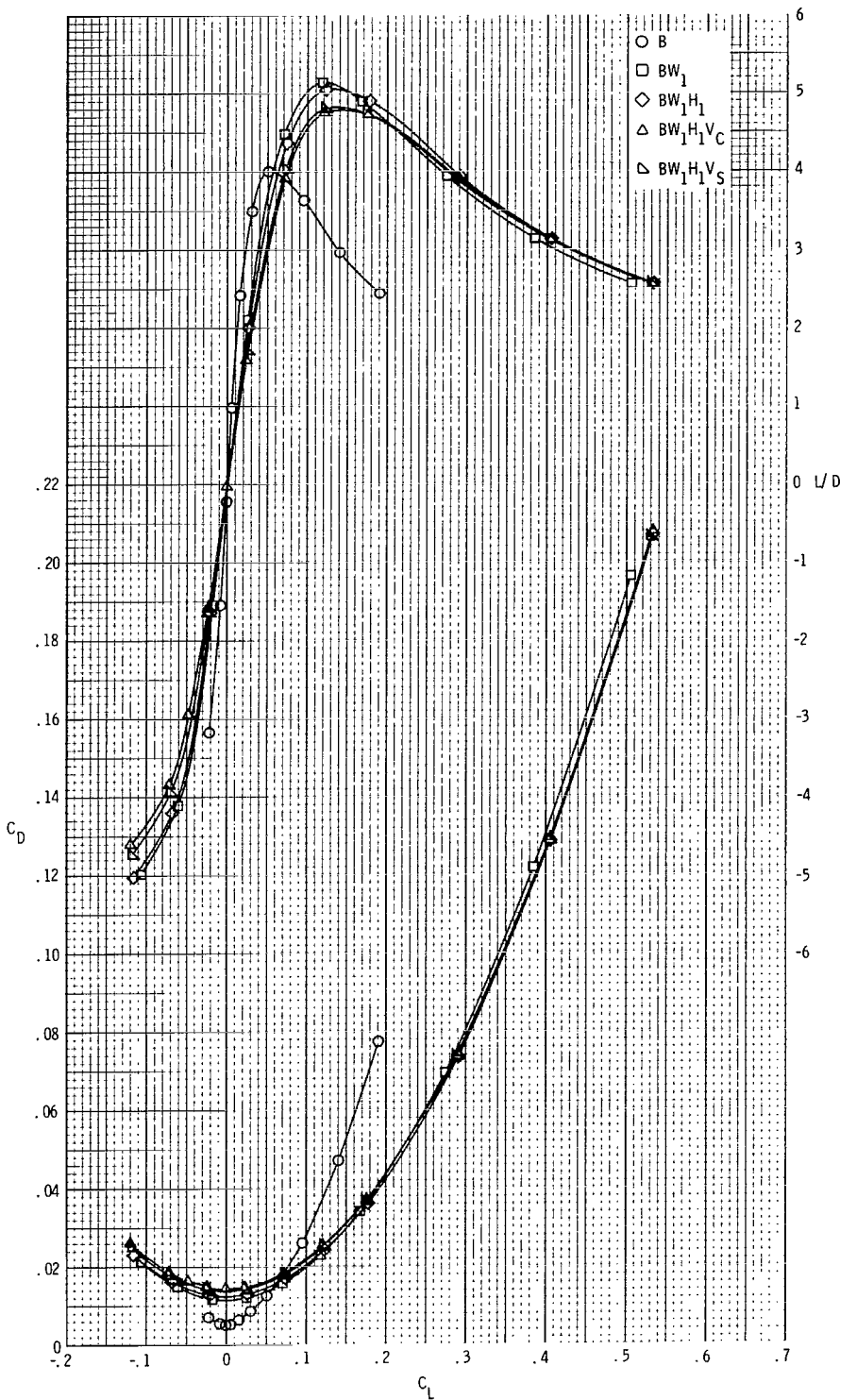
(a) Concluded.

Figure 3.- Continued.



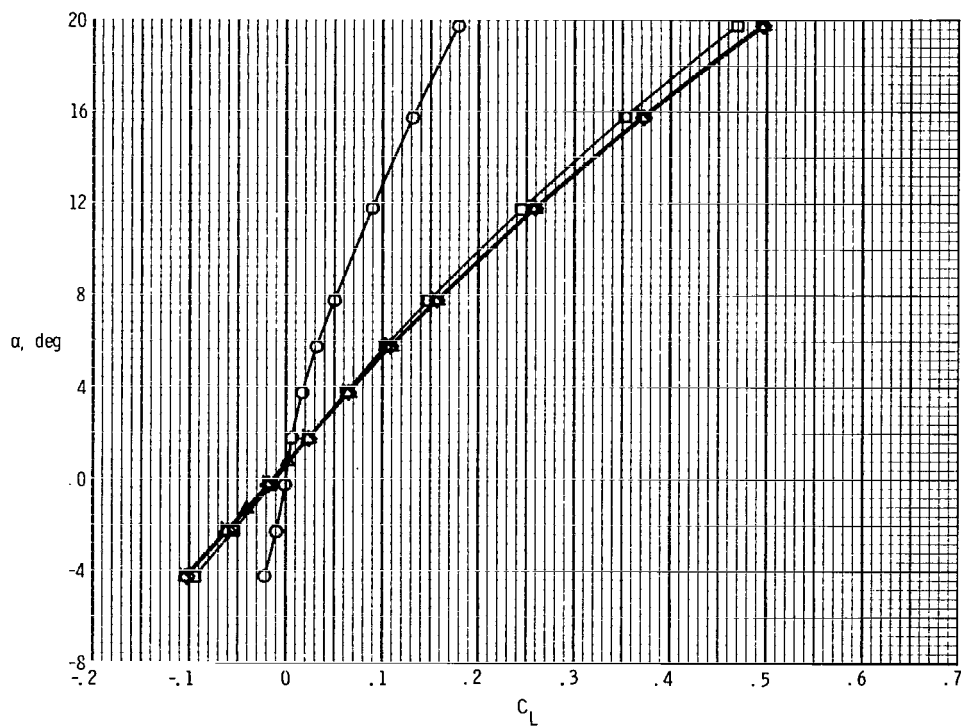
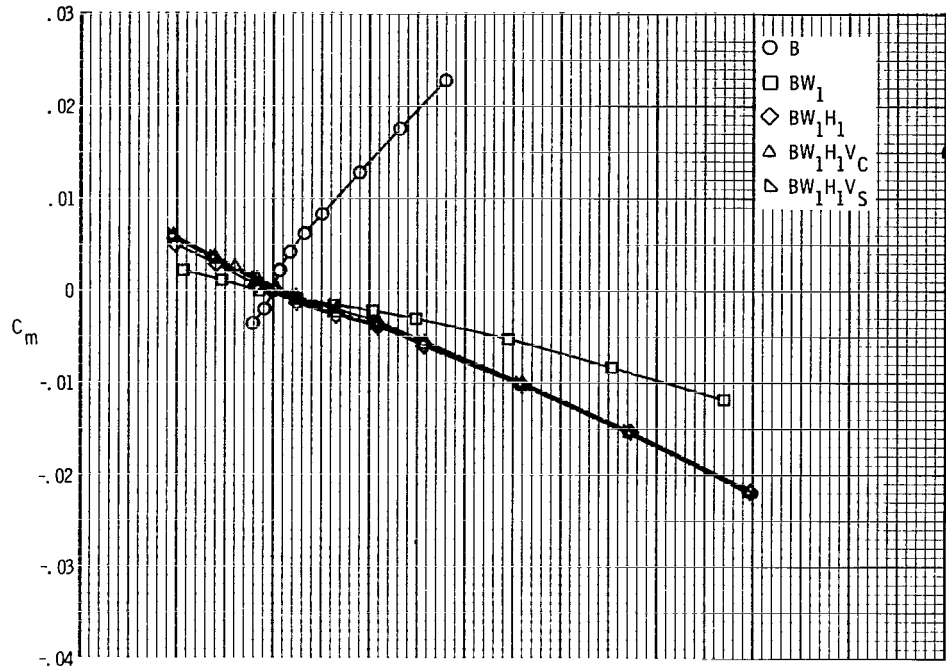
(b)  $M = 3.96.$

**Figure 3.- Continued.**



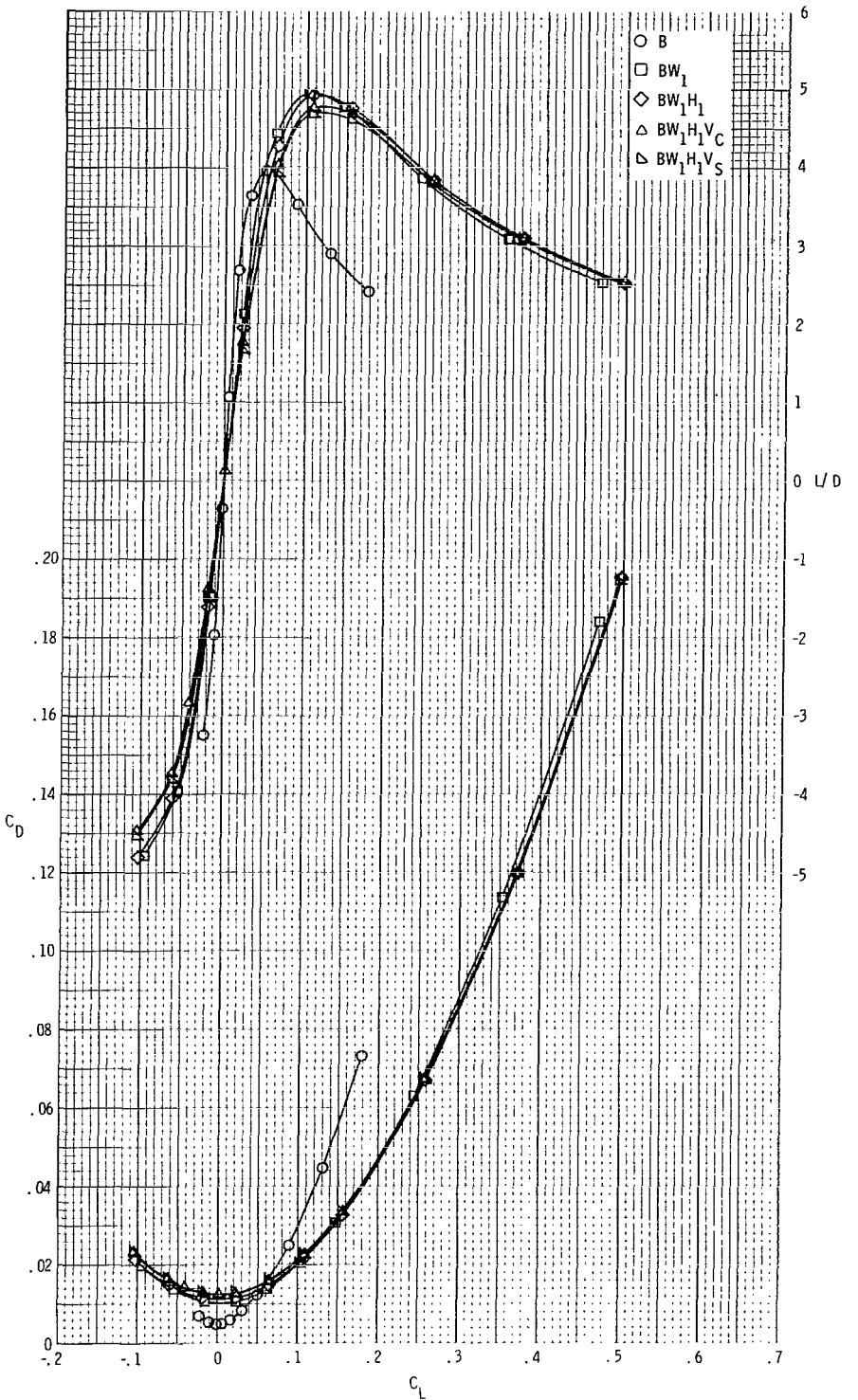
(b) Concluded.

Figure 3.- Continued.



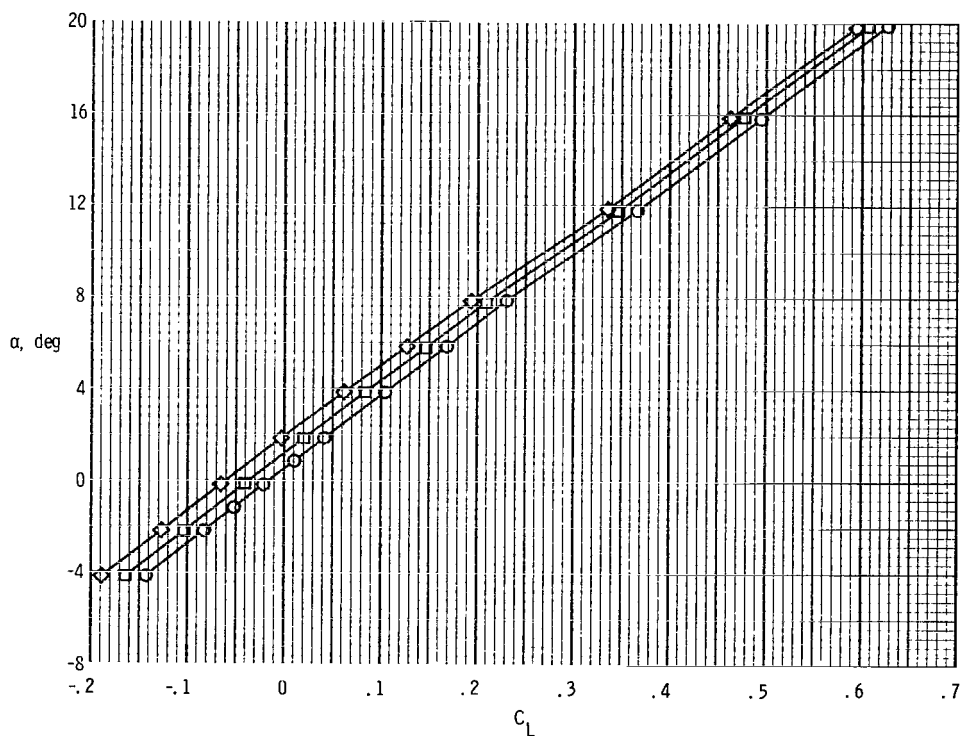
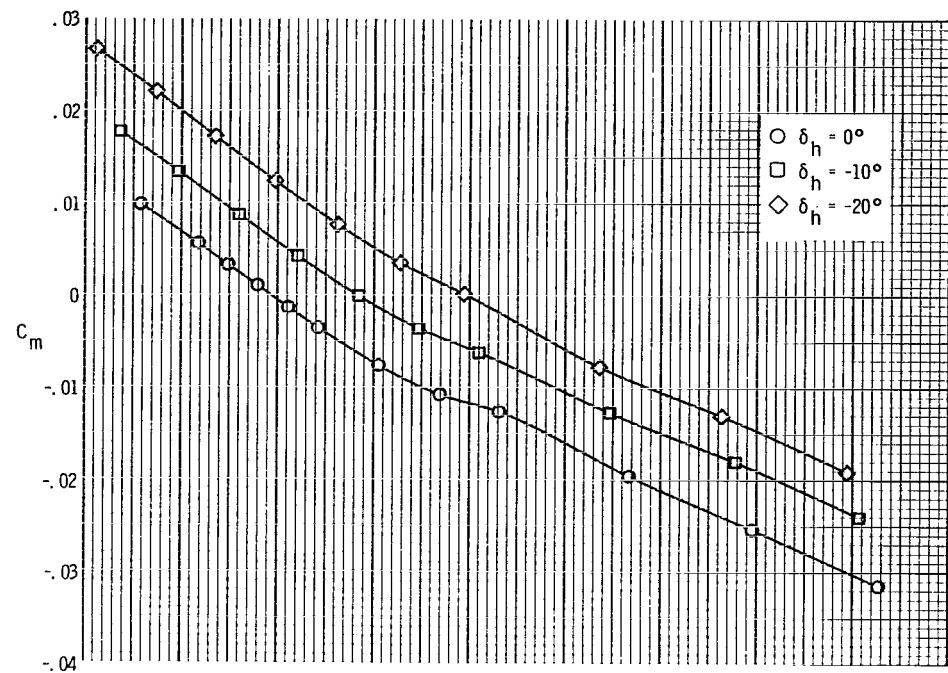
(c)  $M = 4.63.$

Figure 3.- Continued.



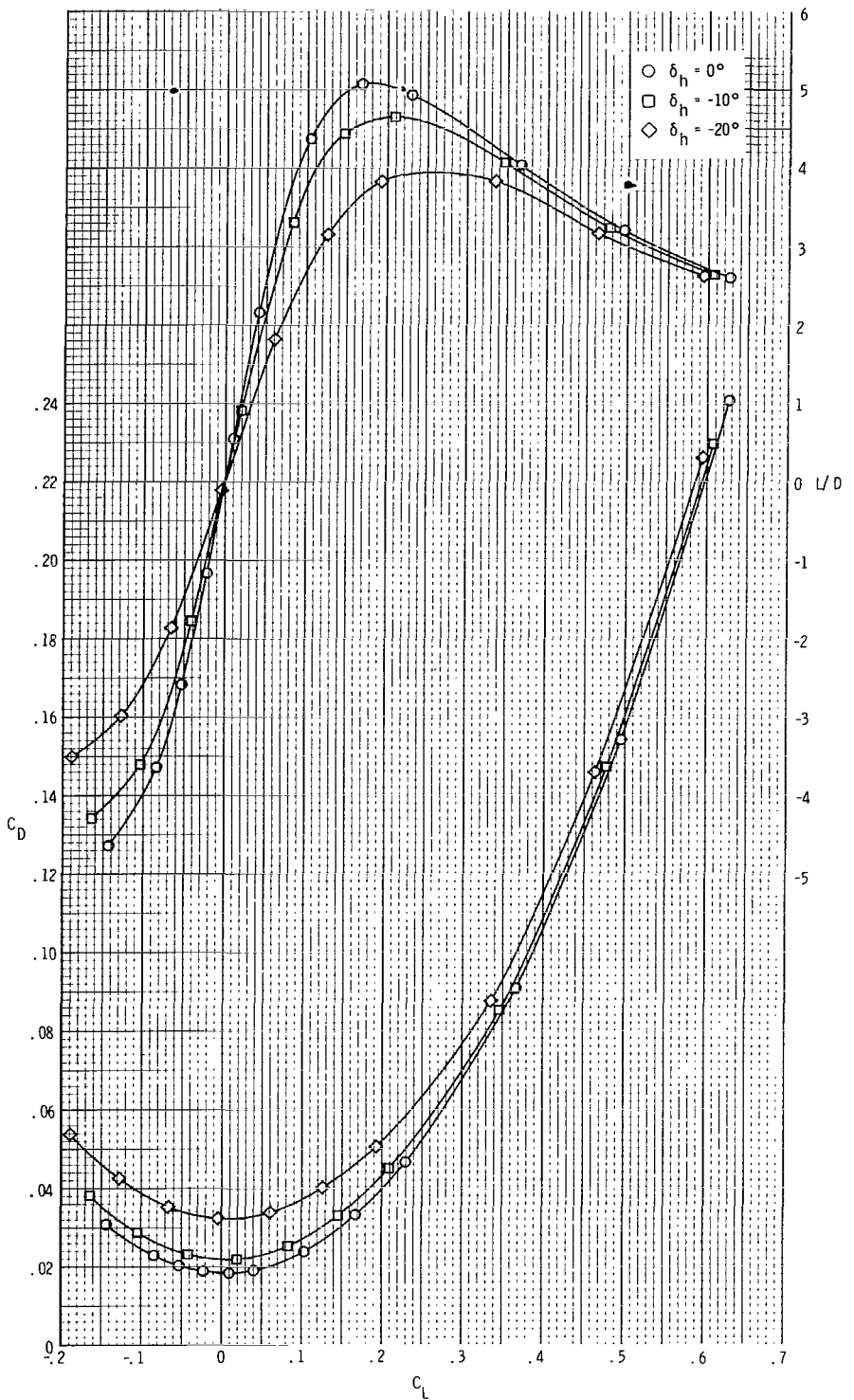
(c) Concluded.

Figure 3.- Concluded.



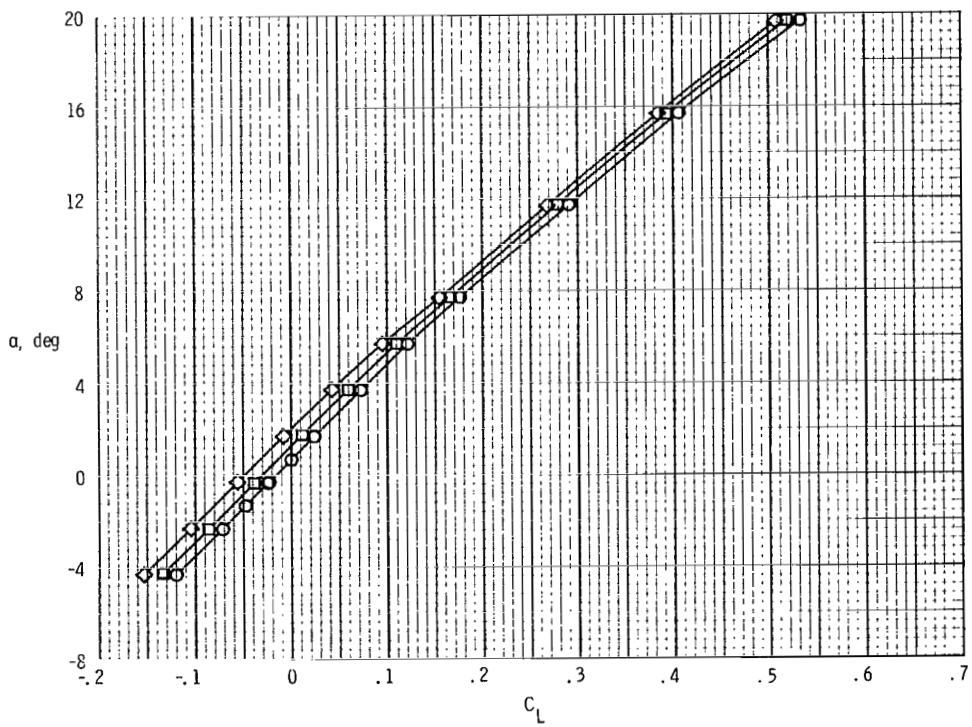
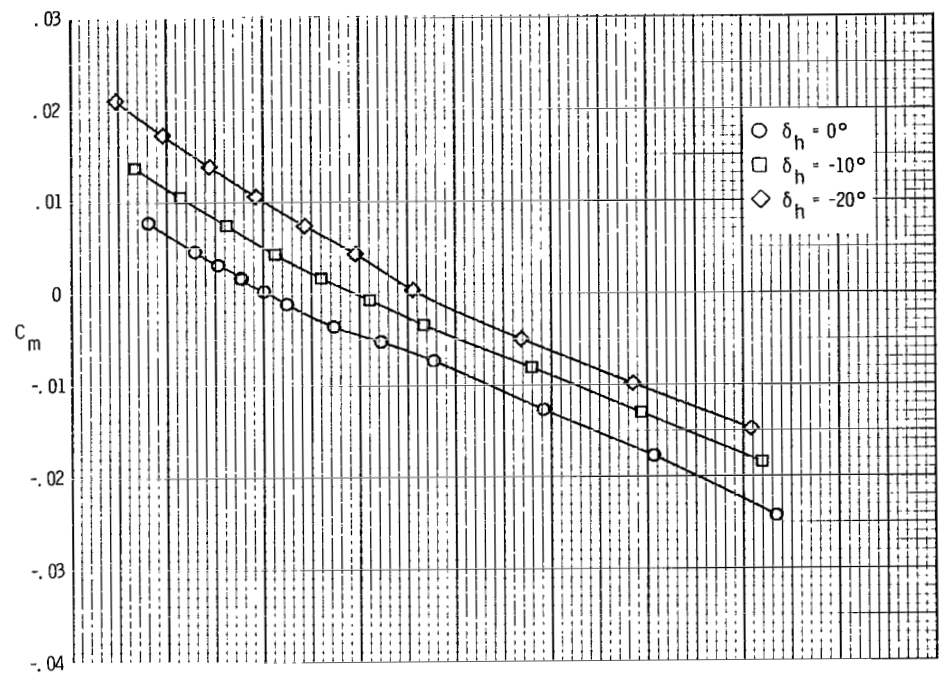
(a)  $M = 2.96$ .

**Figure 4.- Effect of horizontal-tail deflection on longitudinal aerodynamic characteristics of BW<sub>1</sub>H<sub>1</sub>V<sub>C</sub> configuration.**



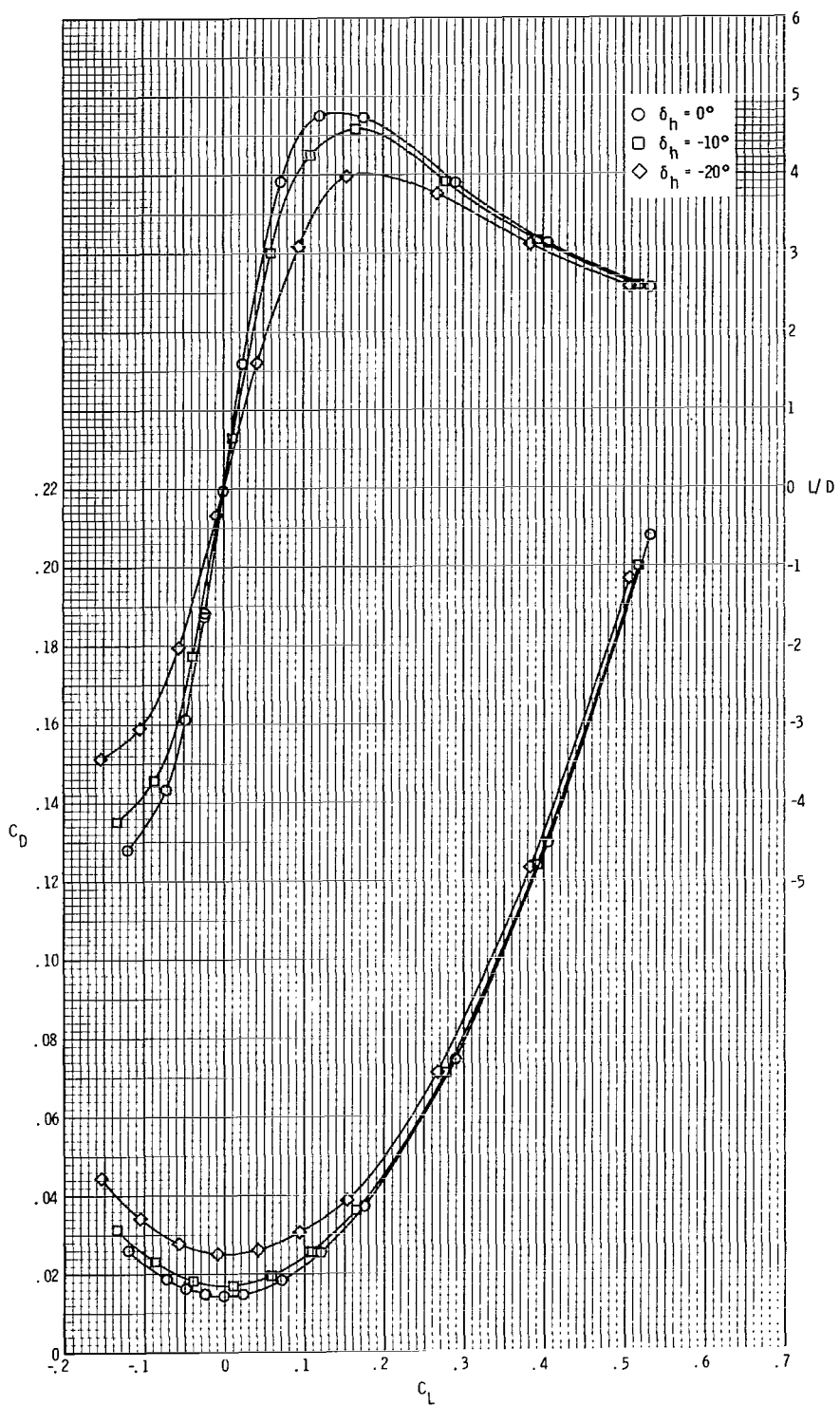
(a) Concluded.

Figure 4.- Continued.



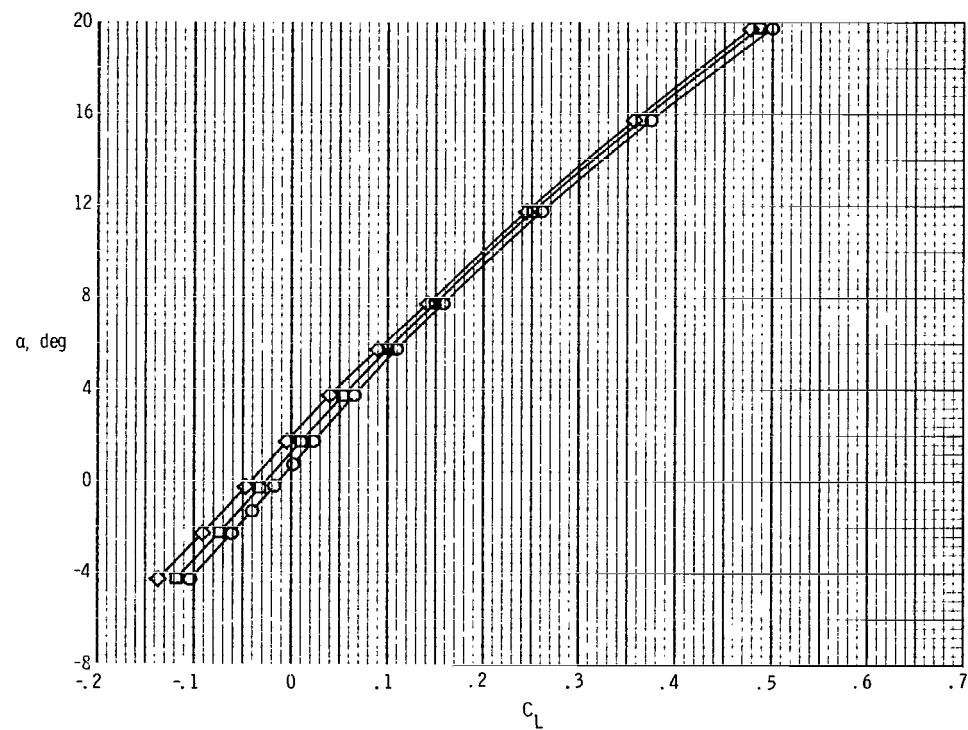
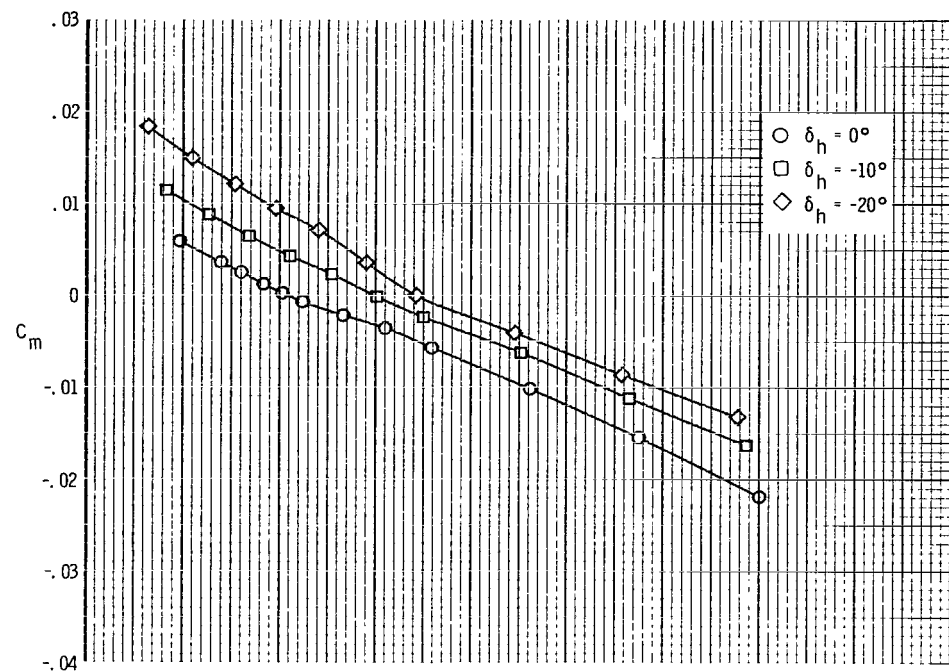
(b)  $M = 3.96.$

**Figure 4.- Continued.**



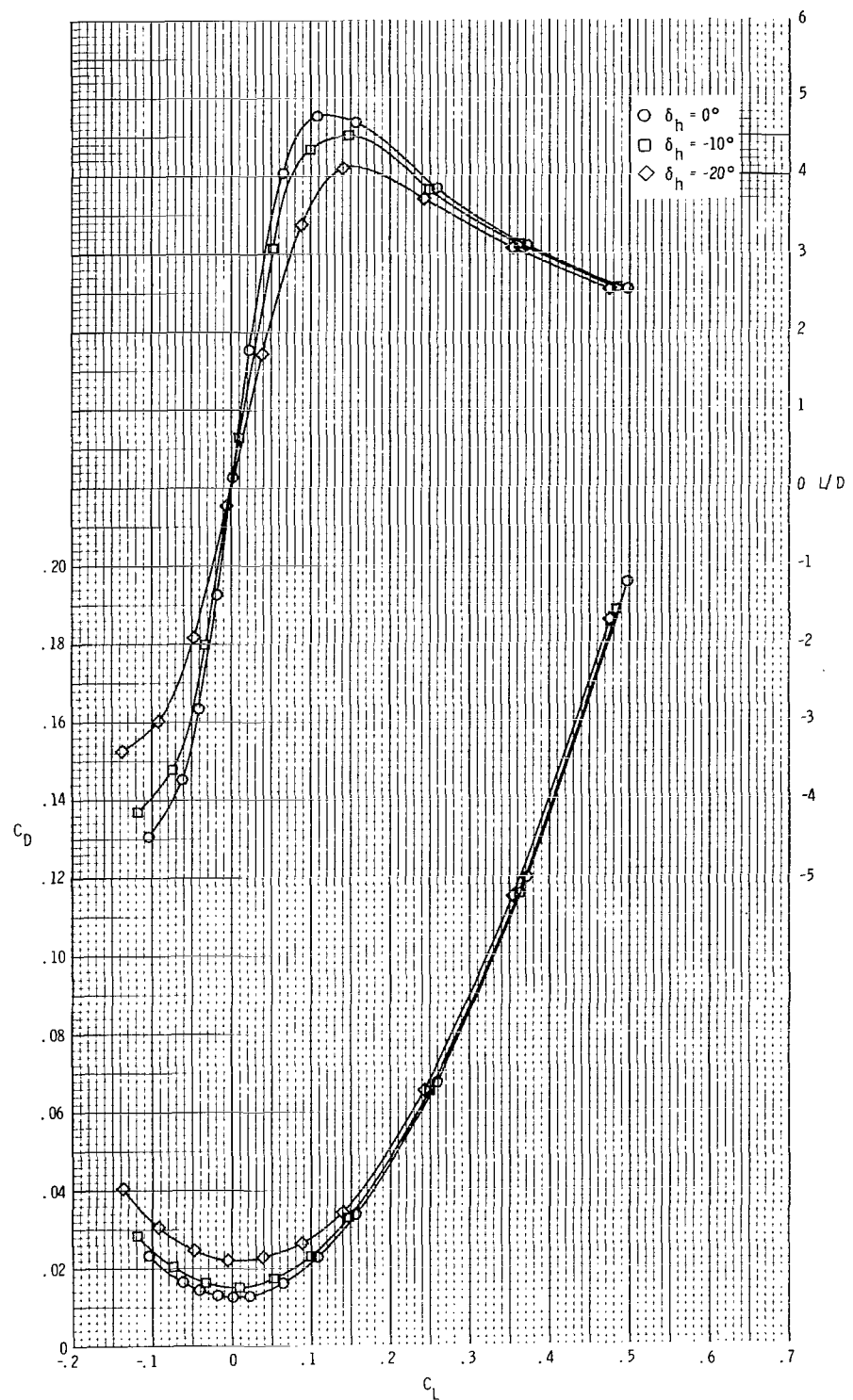
(b) Concluded.

Figure 4.- Continued.



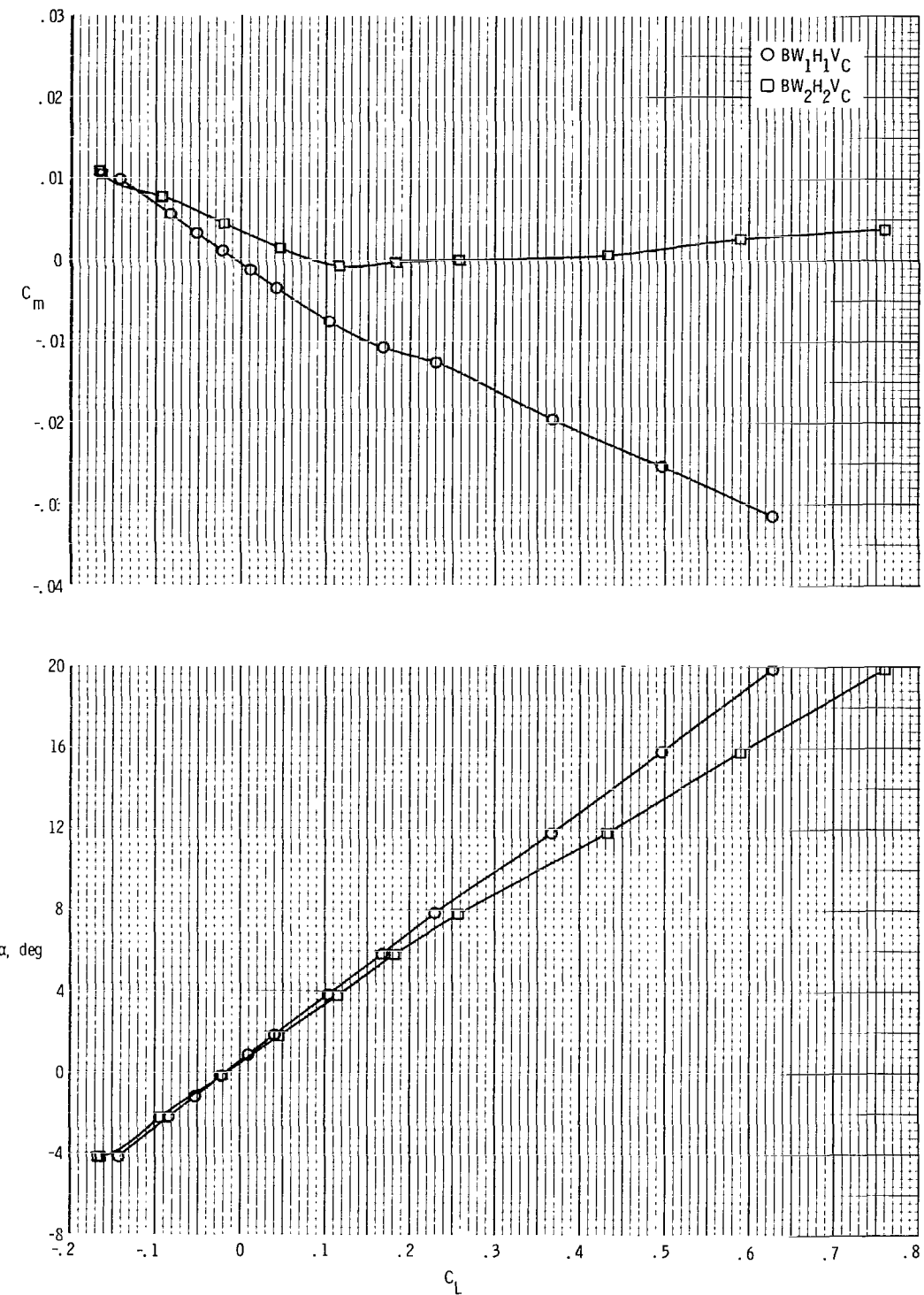
(c)  $M = 4.63.$

Figure 4.- Continued.



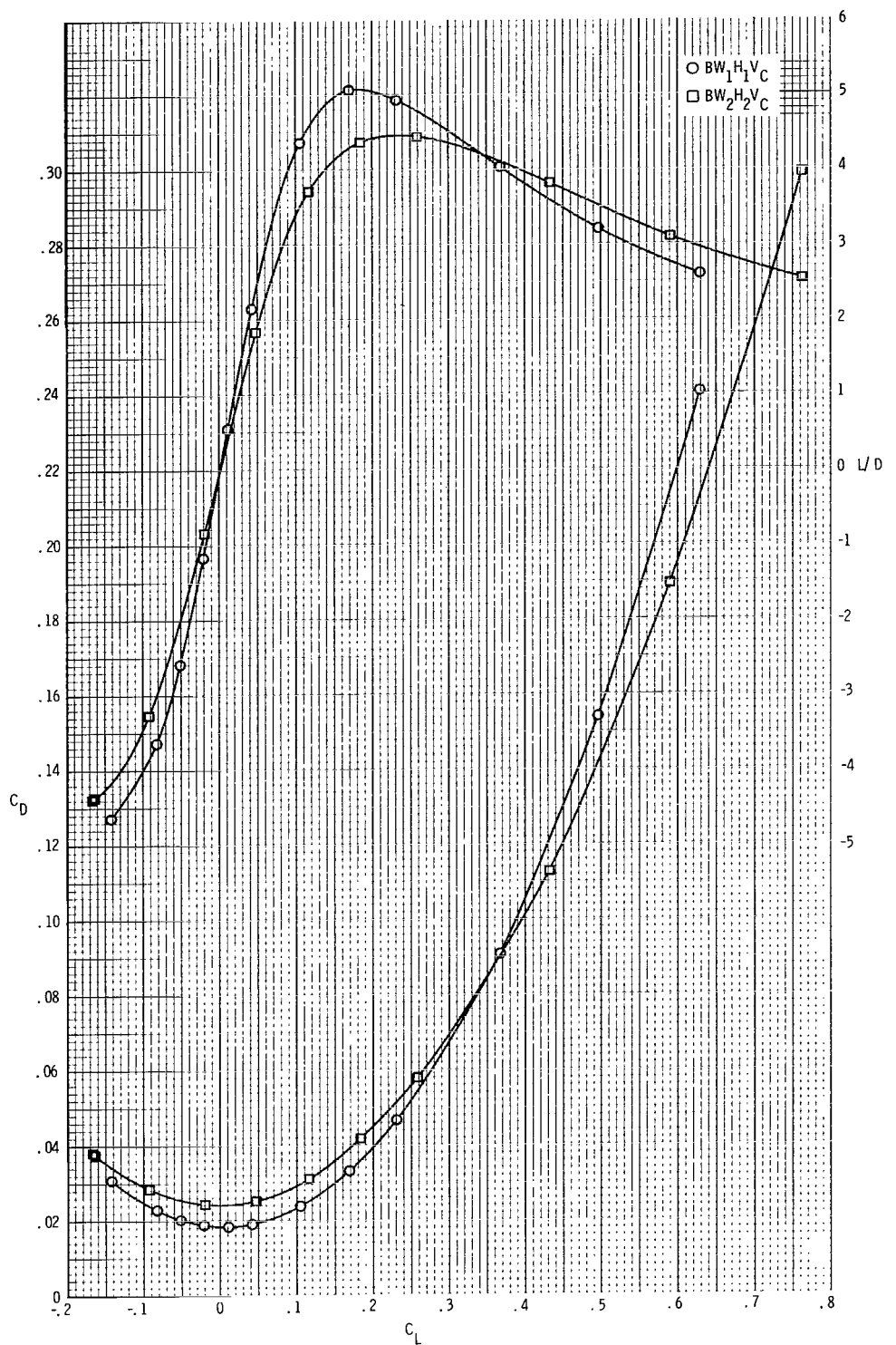
(c) Concluded.

Figure 4.- Concluded.



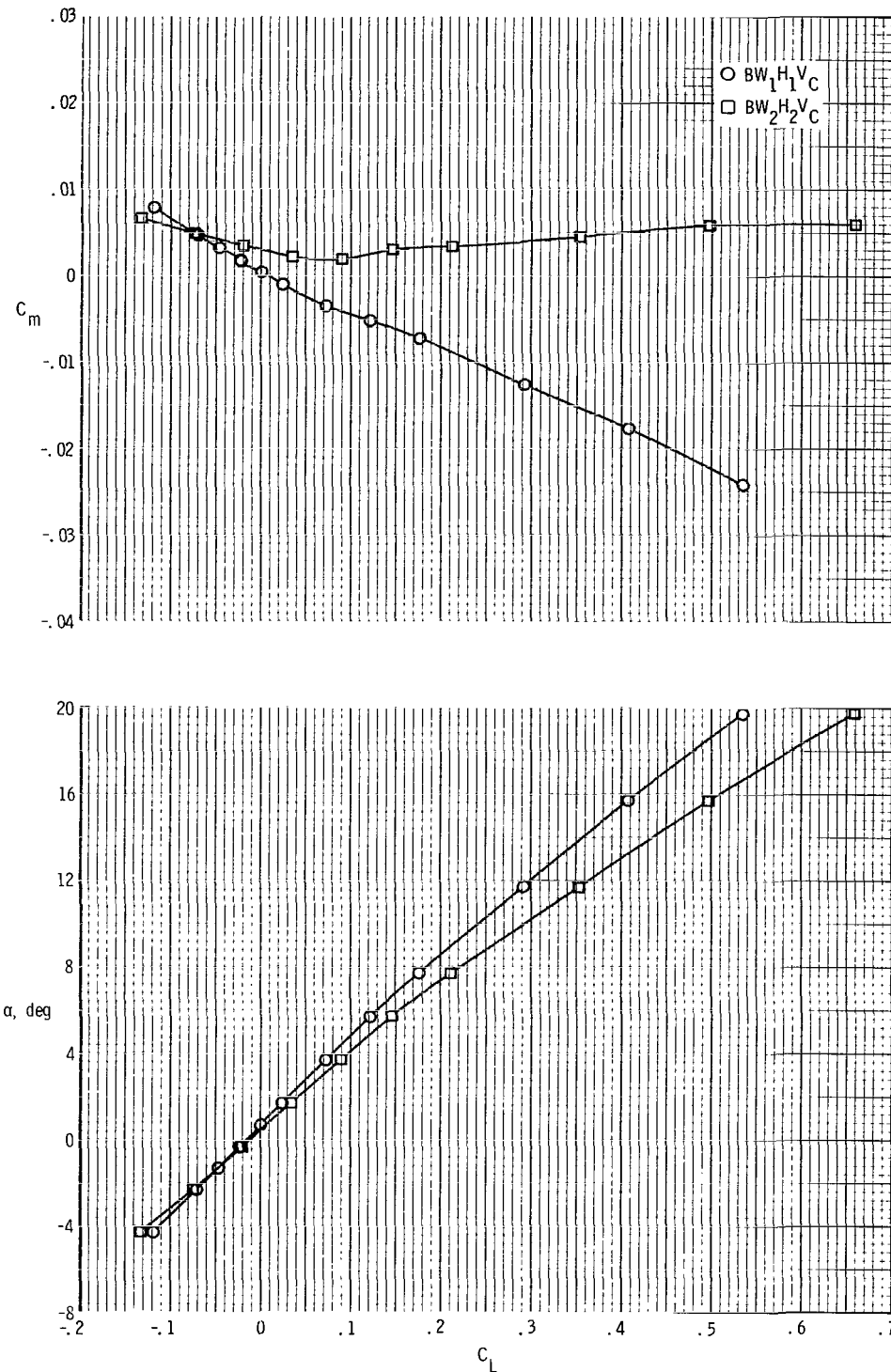
(a)  $M = 2.96$ .

Figure 5.- Comparison of  $BW_1H_1V_C$  and  $BW_2H_2V_C$  configurations.



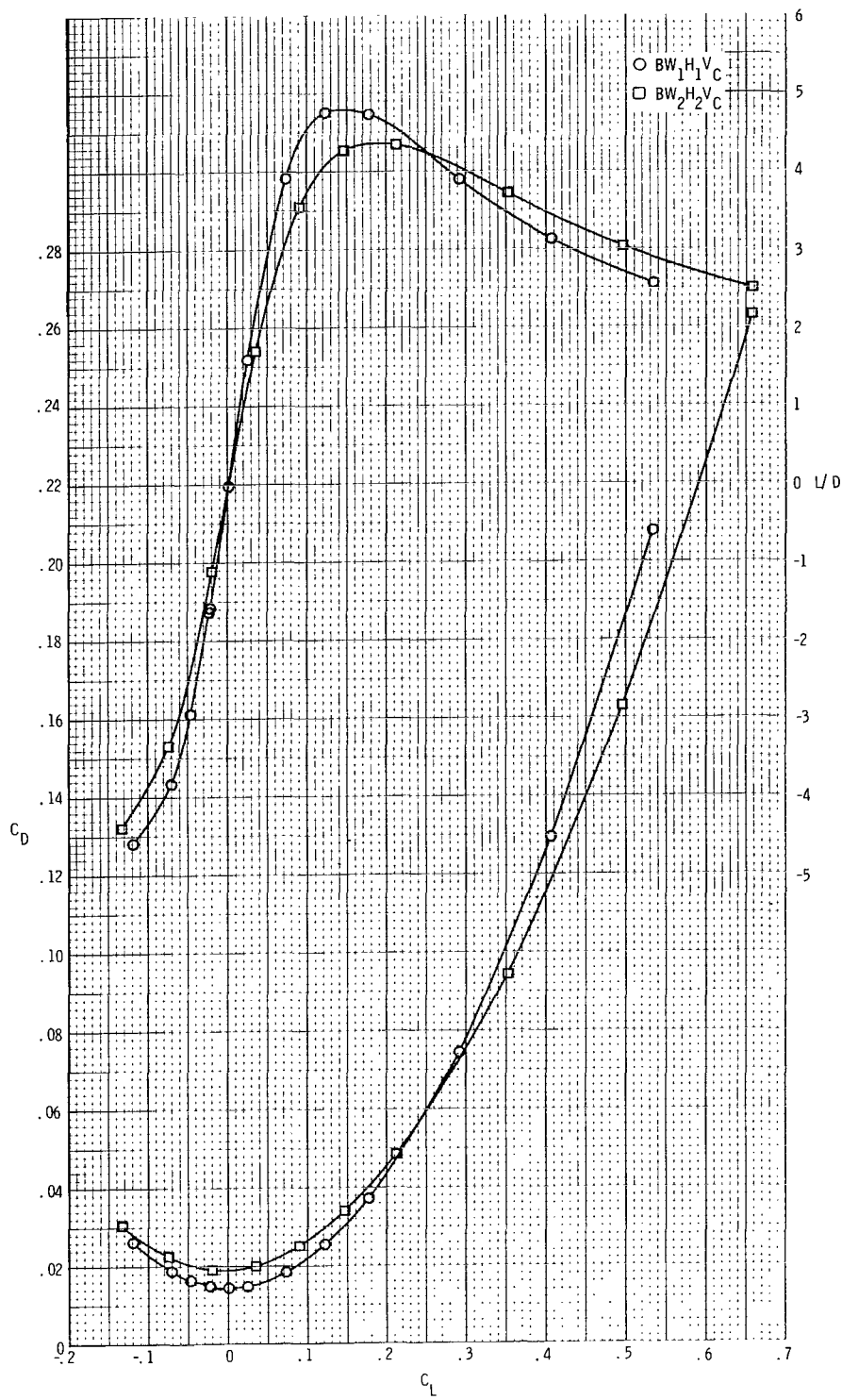
(a) Concluded.

Figure 5.- Continued.



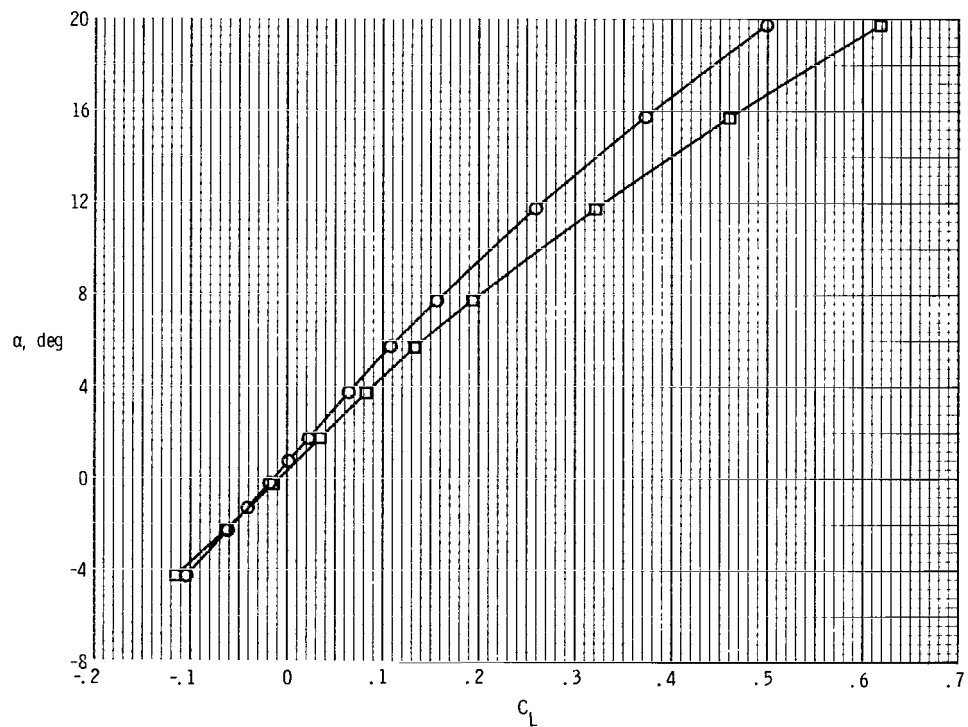
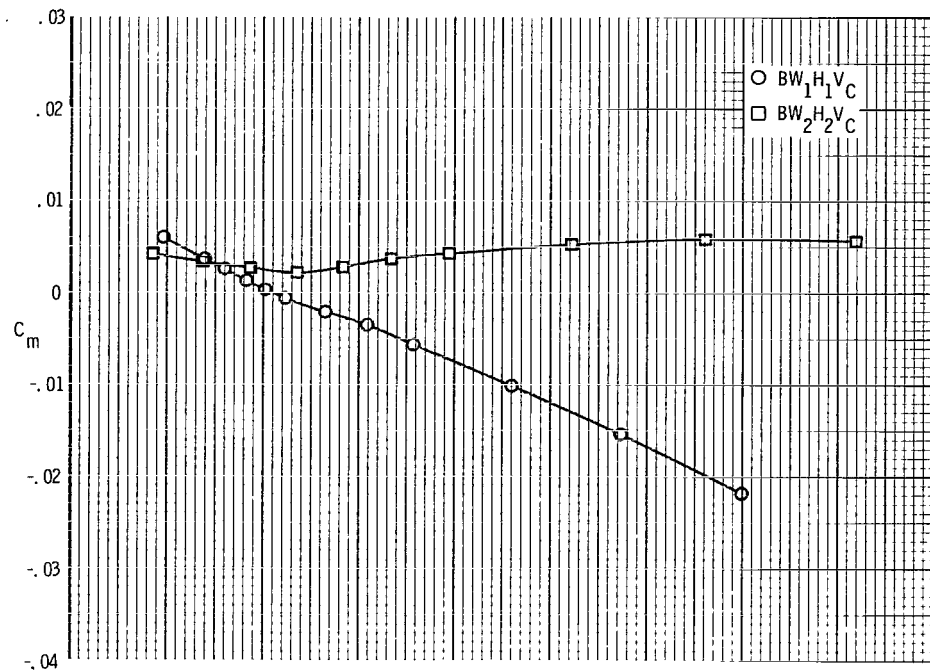
(b)  $M = 3.96.$

Figure 5.- Continued.



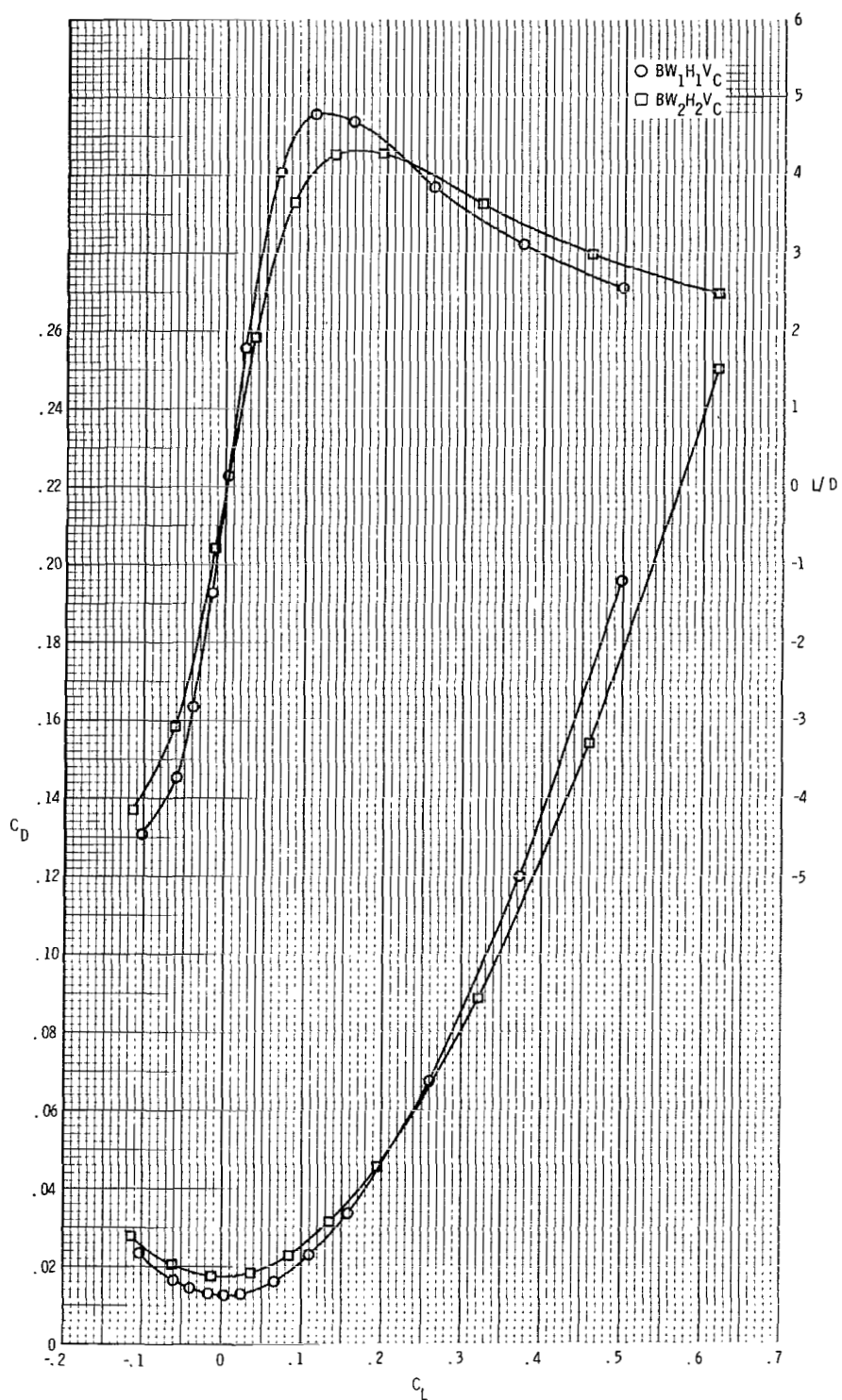
(b) Concluded.

Figure 5.- Continued.



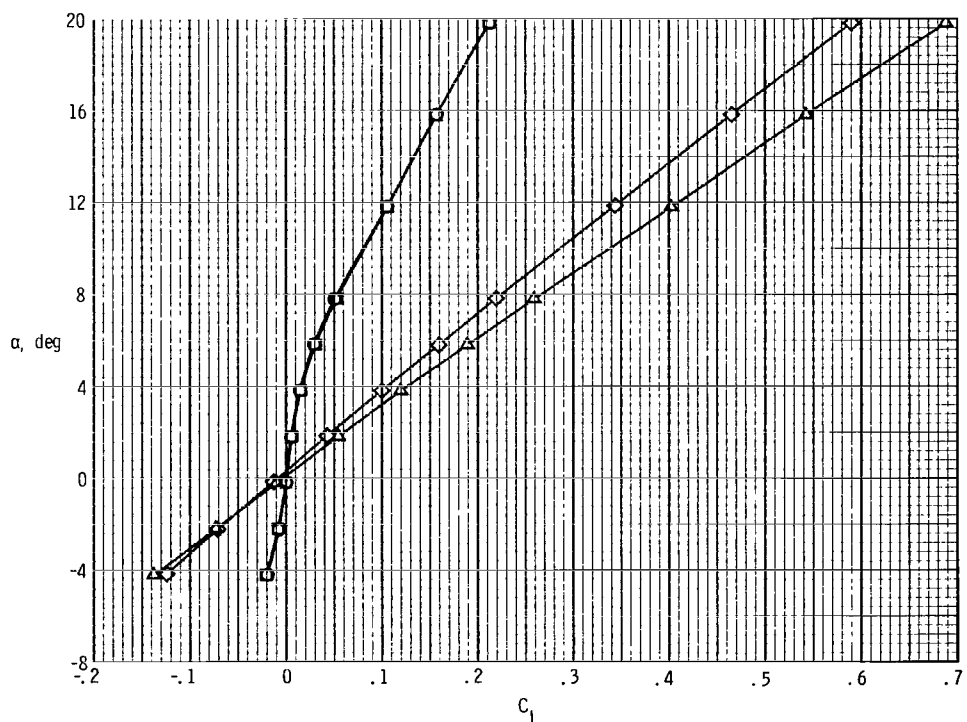
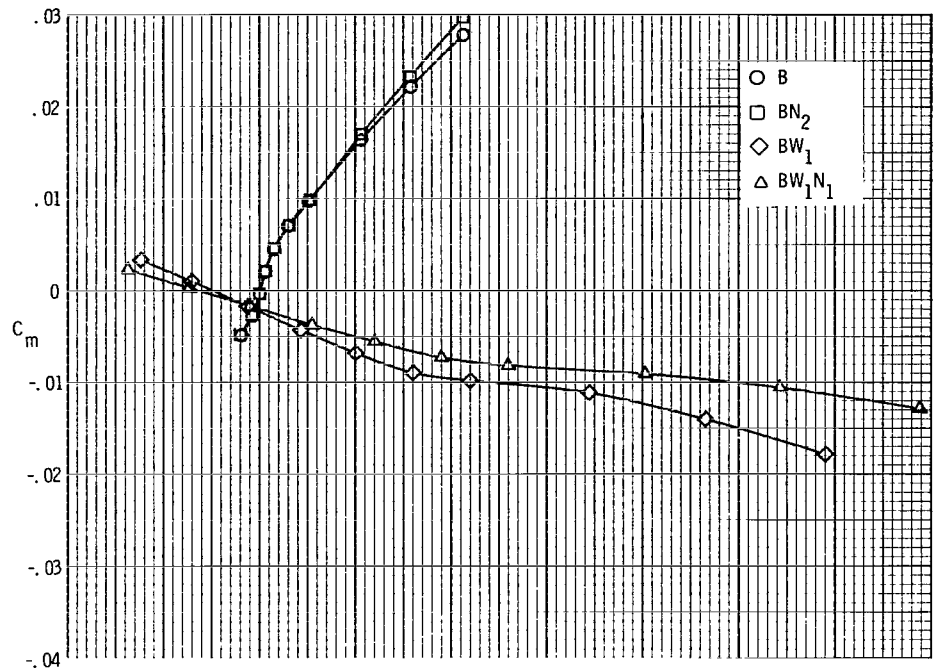
(c)  $M = 4.63.$

Figure 5.- Continued.



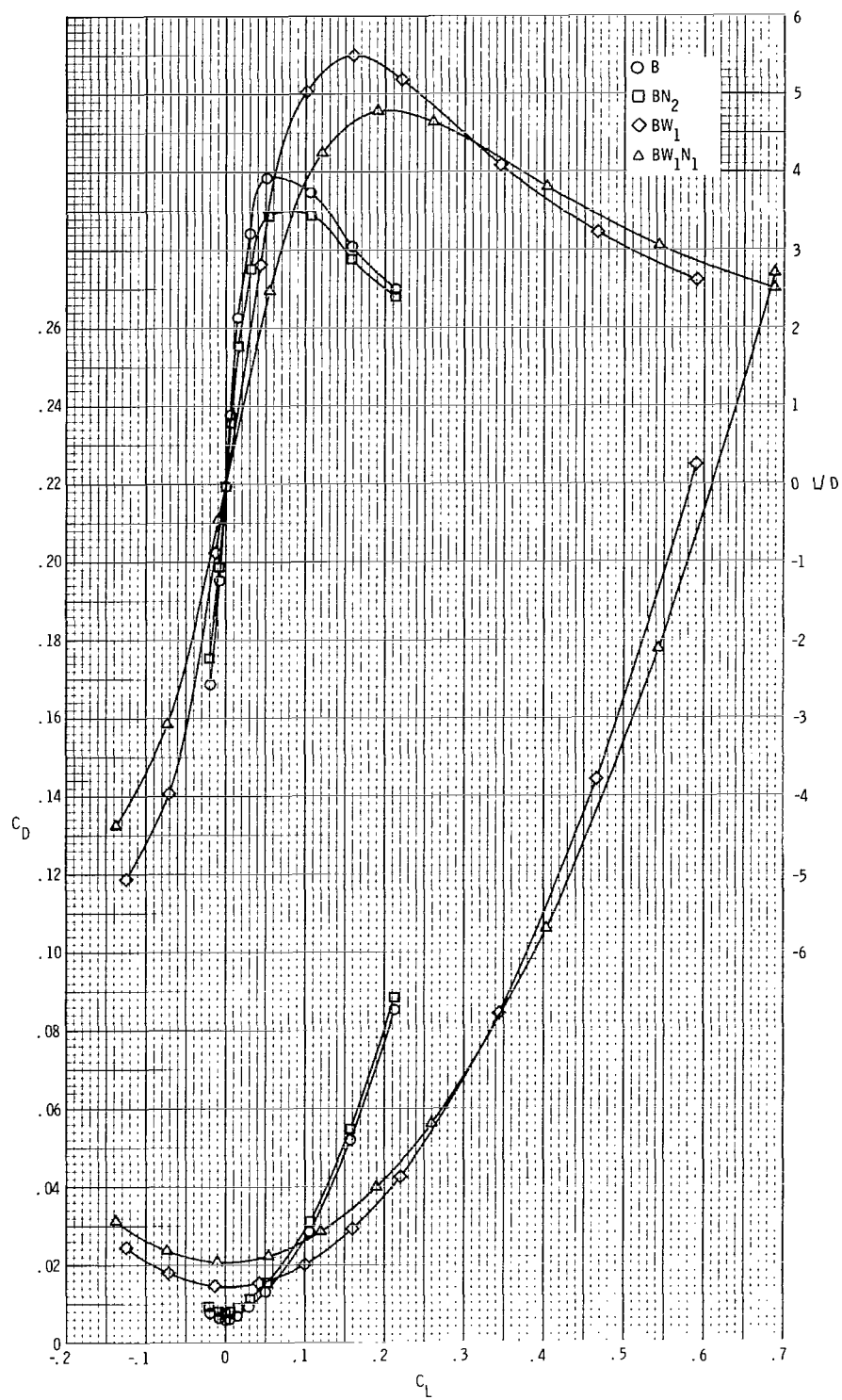
(c) Concluded.

Figure 5.- Concluded.



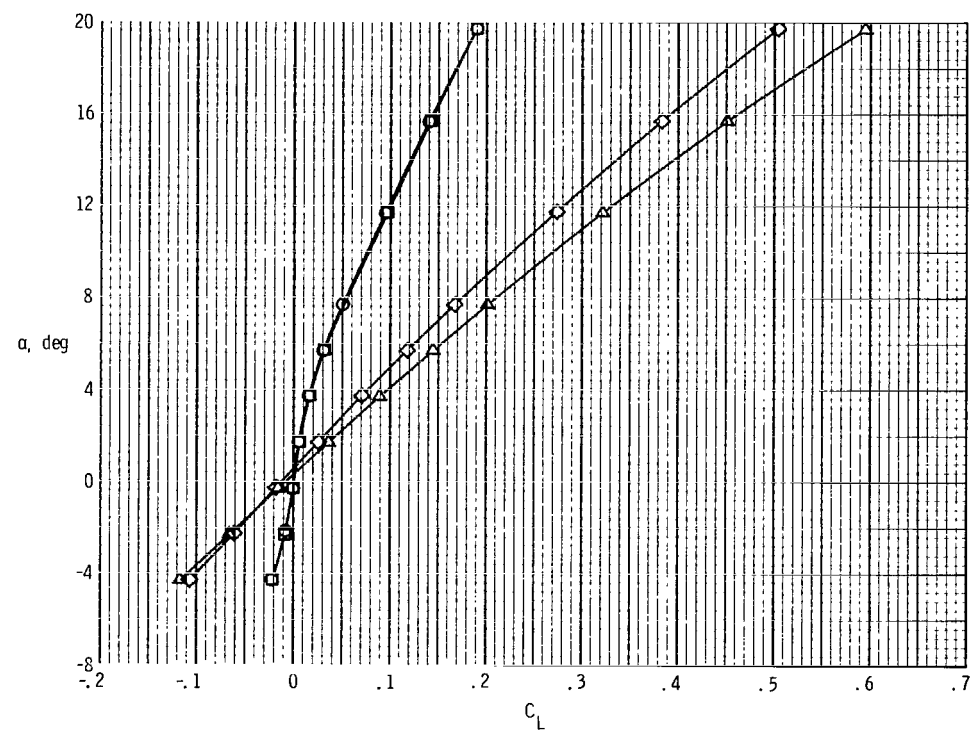
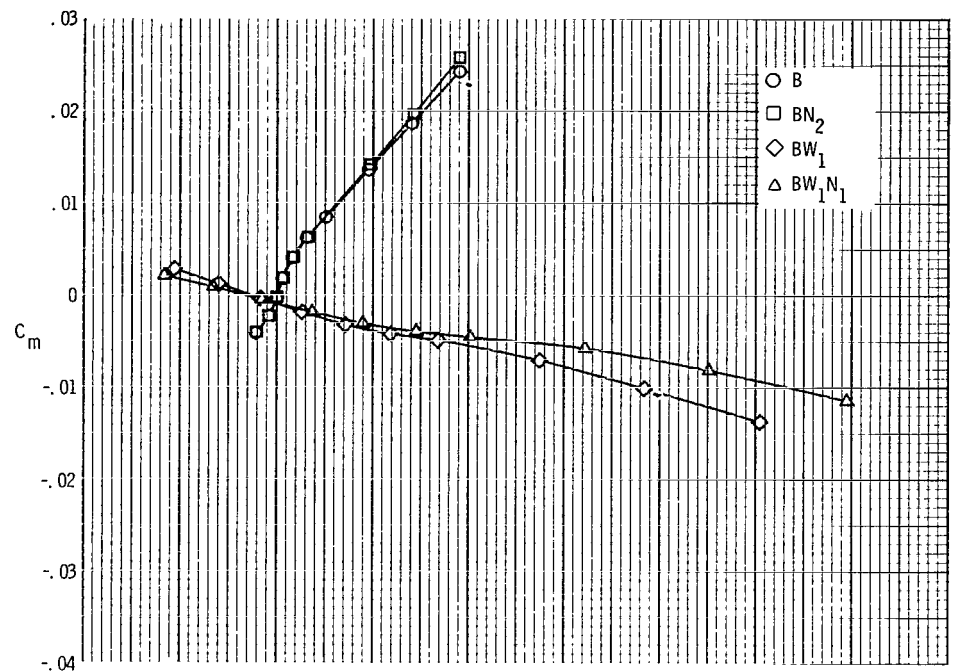
(a)  $M = 2.96$ .

Figure 6.- Nacelle increments for fuselage and wing-mounted nacelles.



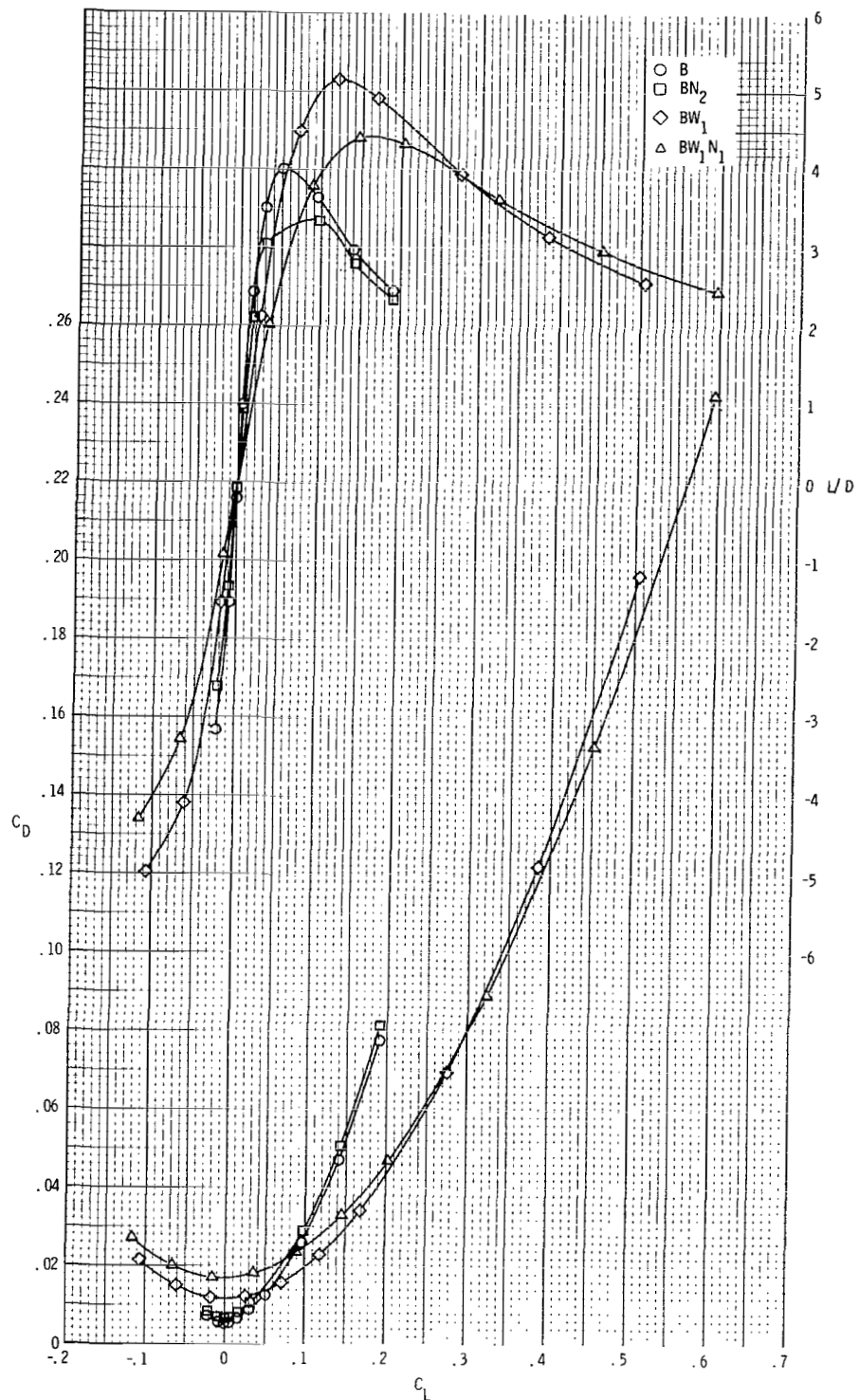
(a) Concluded.

Figure 6.- Continued.



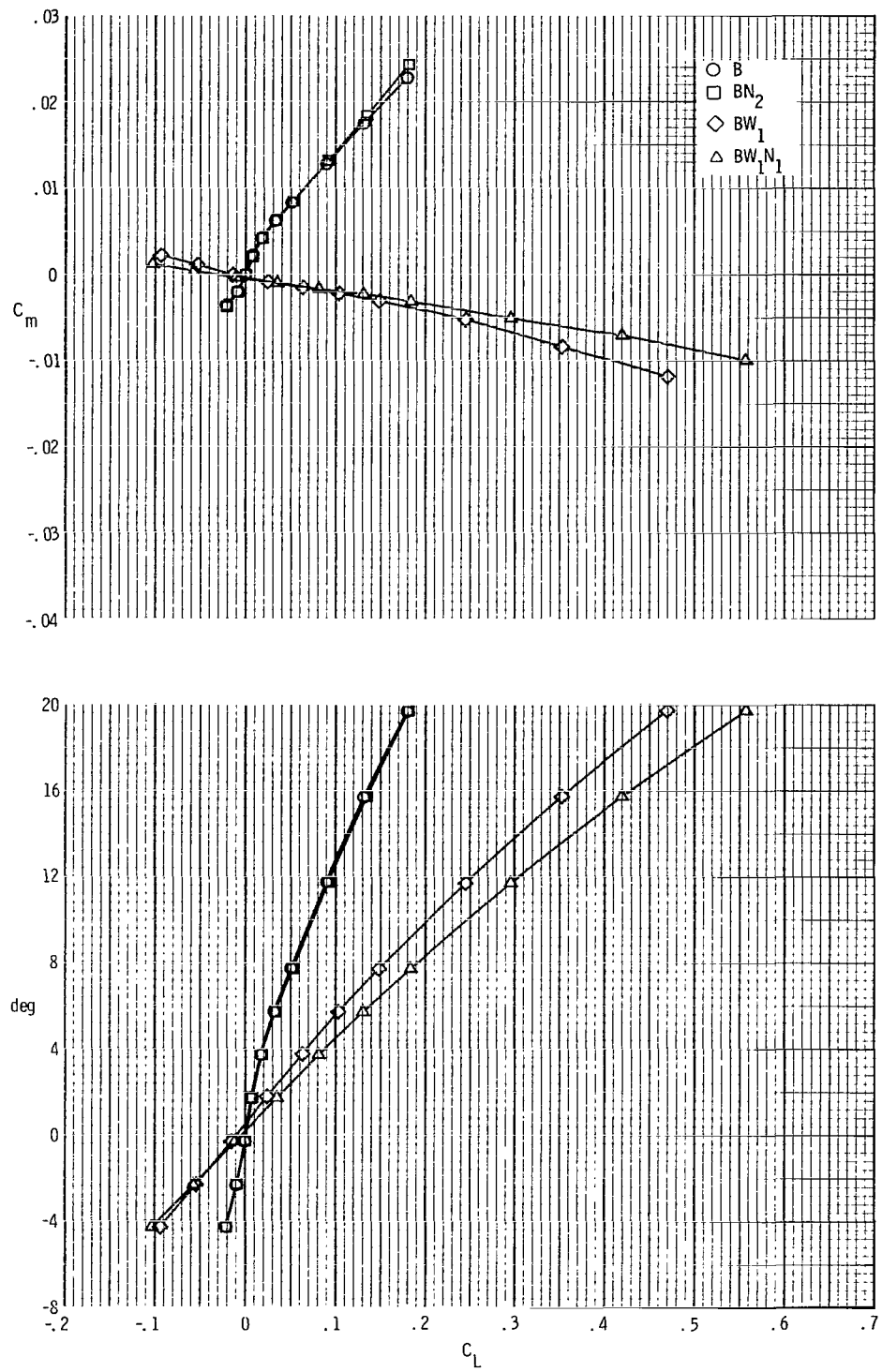
(b)  $M = 3.96.$

**Figure 6.- Continued.**



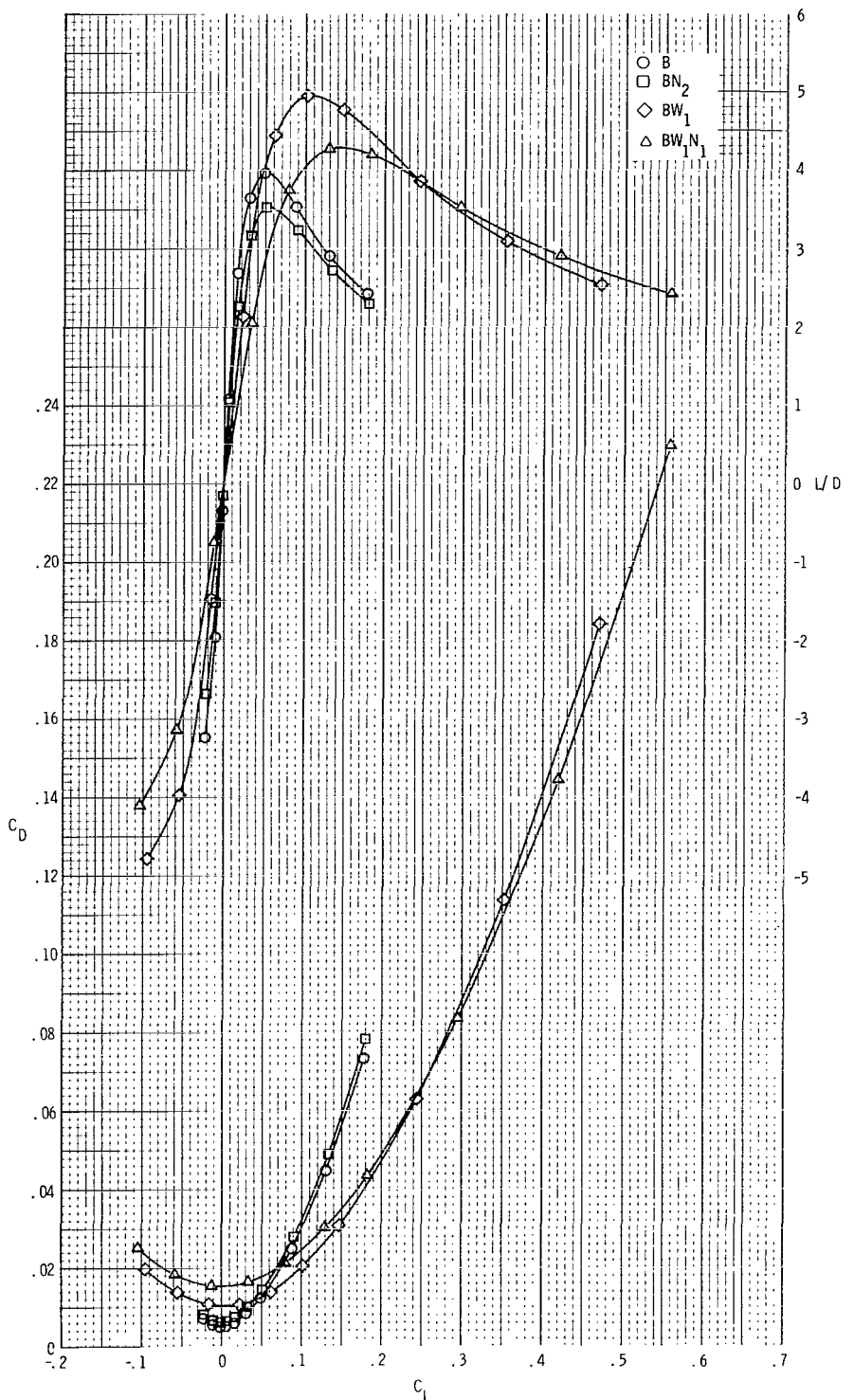
(b) Concluded.

Figure 6.- Continued.



(c)  $M = 4.63.$

Figure 6.- Continued.



(c) Concluded.

Figure 6.- Concluded.

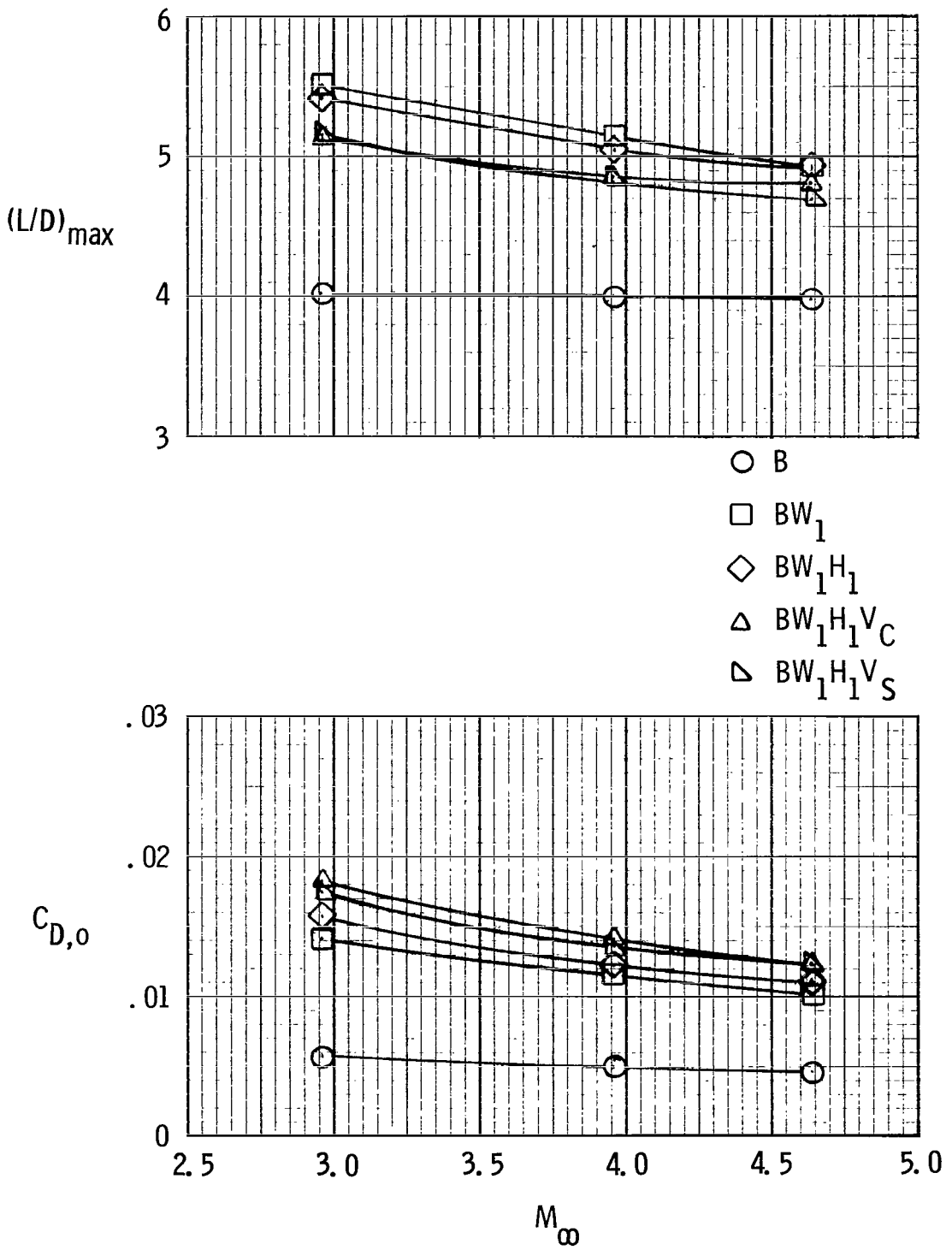


Figure 7.- Summary drag data for configuration buildup.

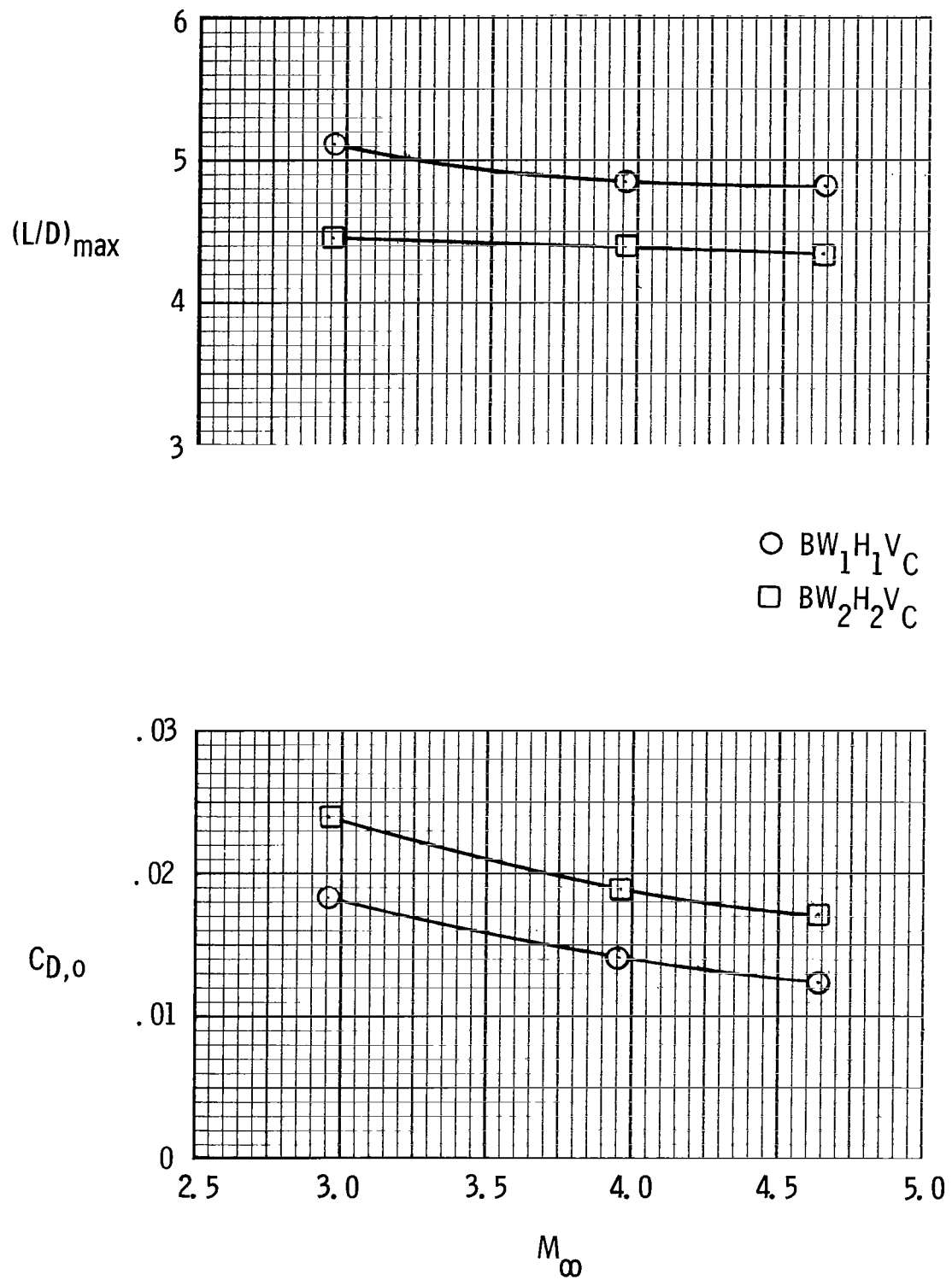


Figure 8.- Summary drag data for  $BW_1 H_1 V_C$  and  $BW_2 H_2 V_C$  configurations.

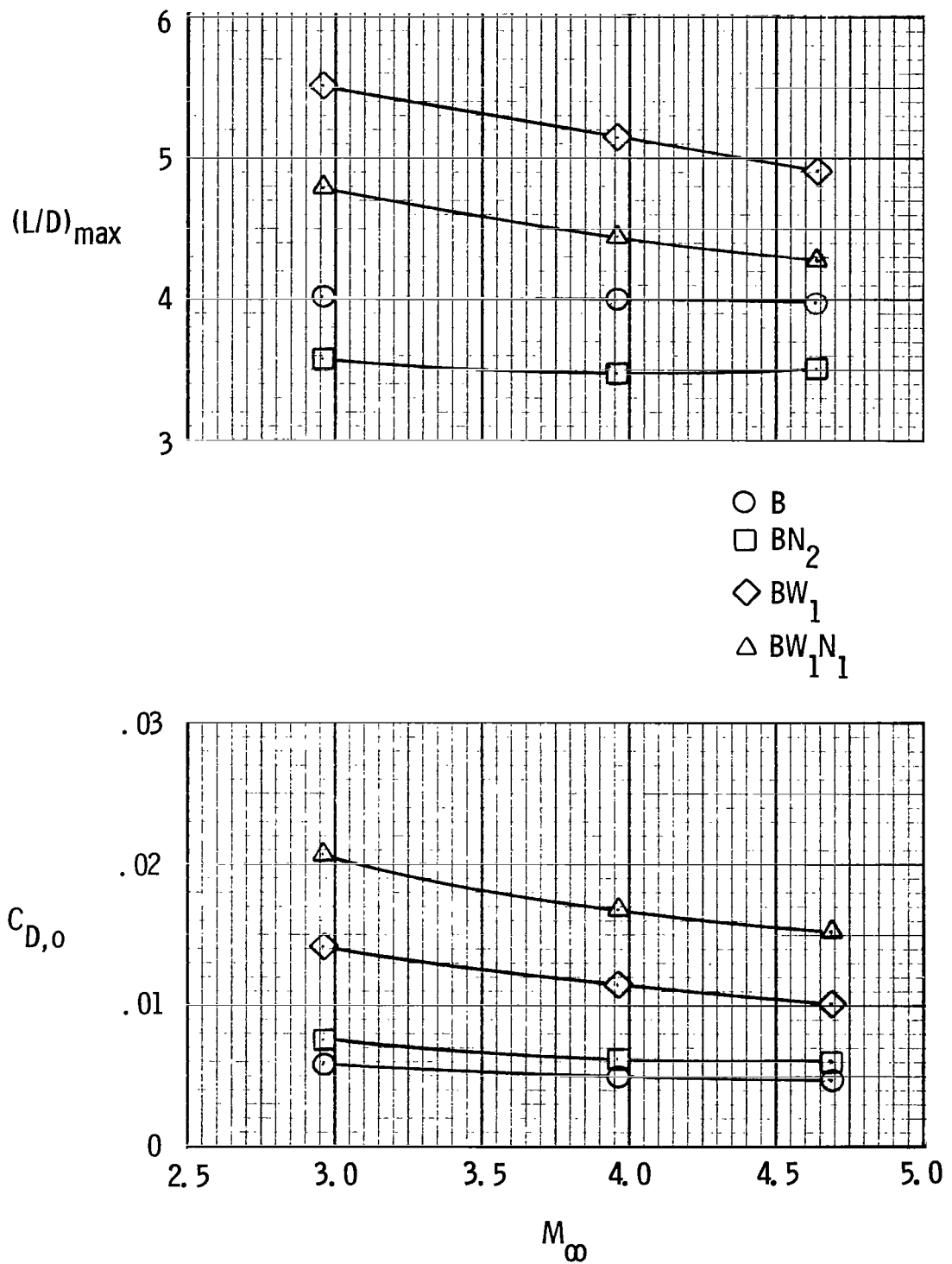
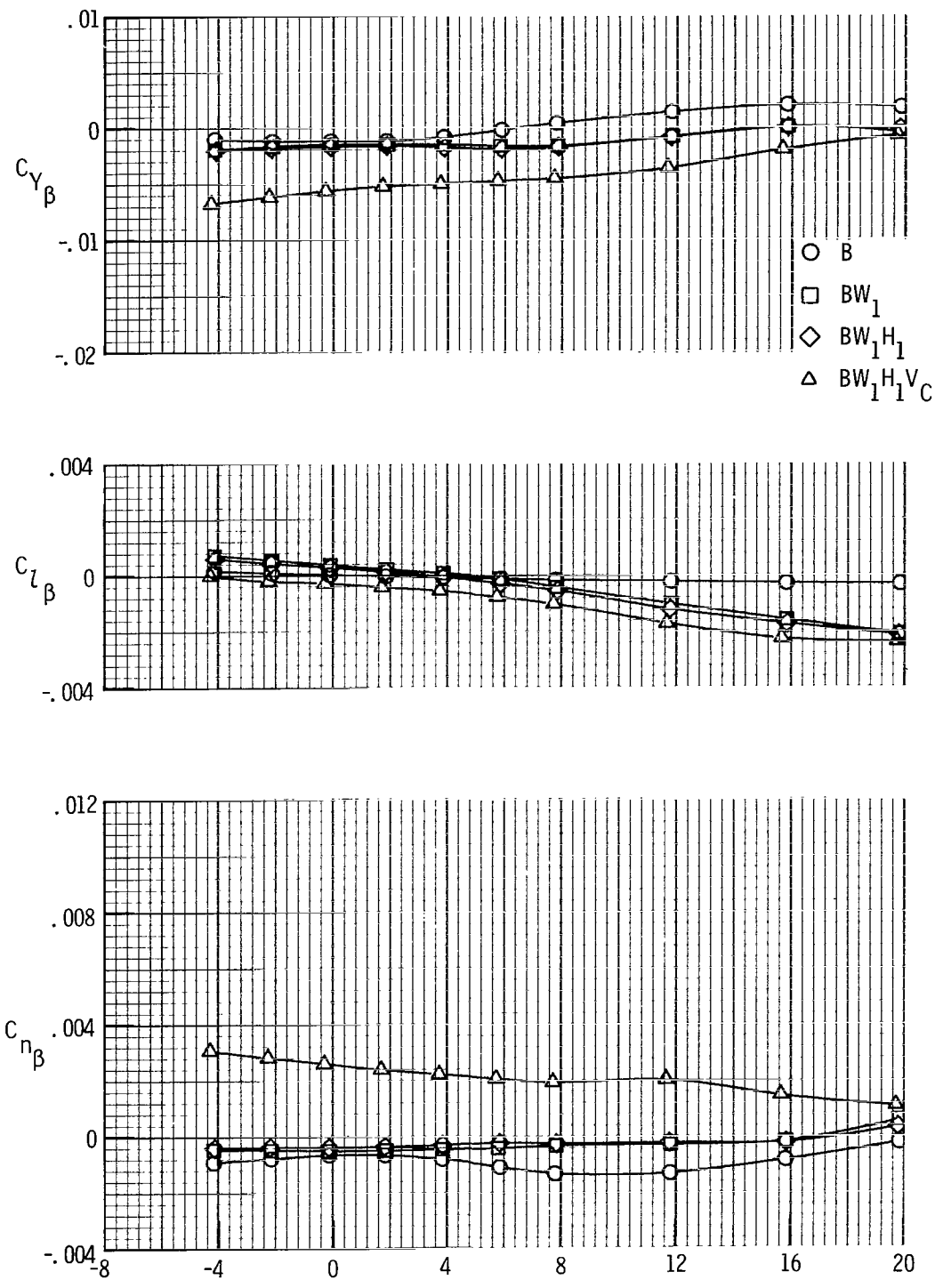
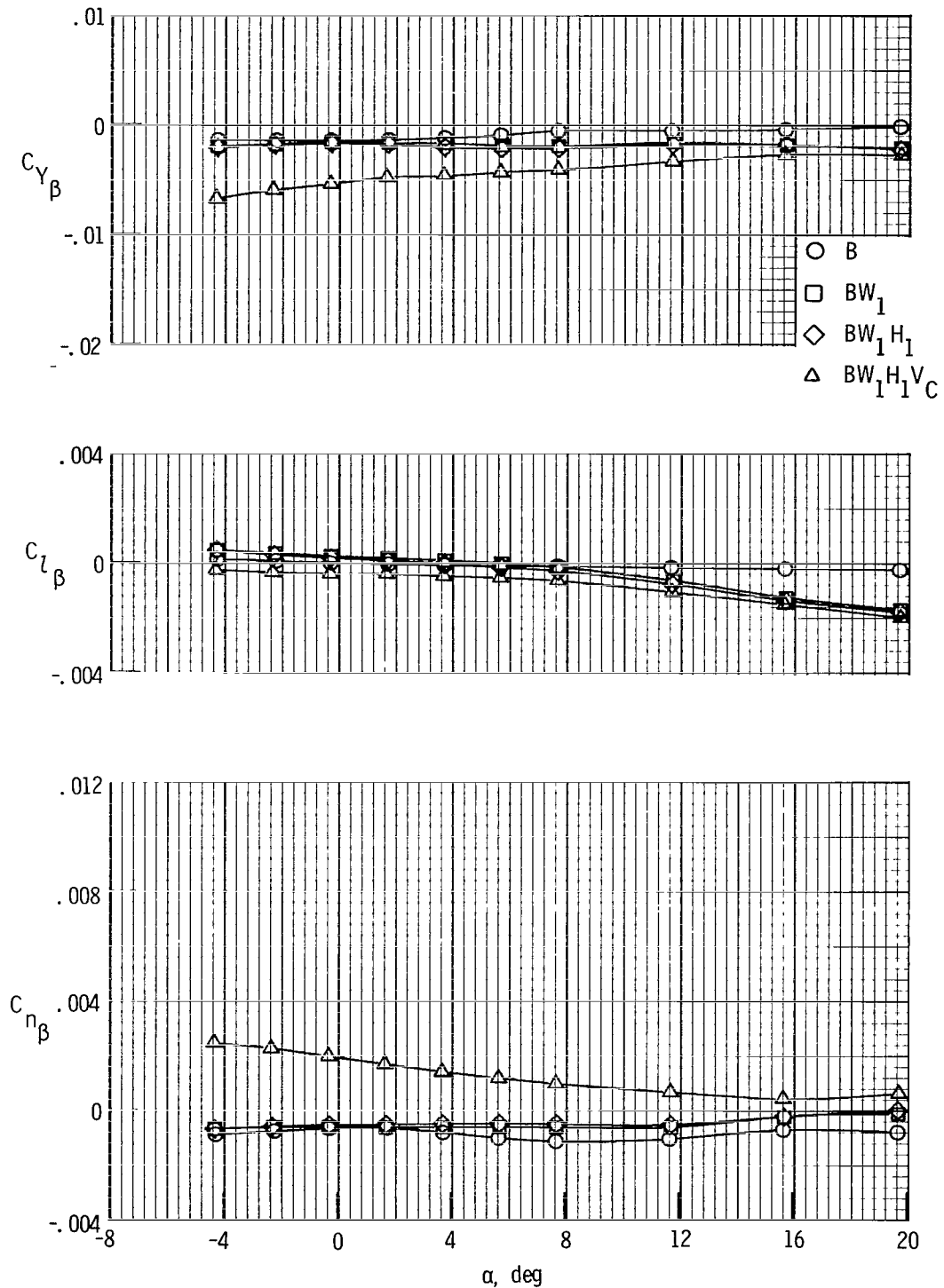


Figure 9.- Summary drag data for nacelle-on and nacelle-off configurations.



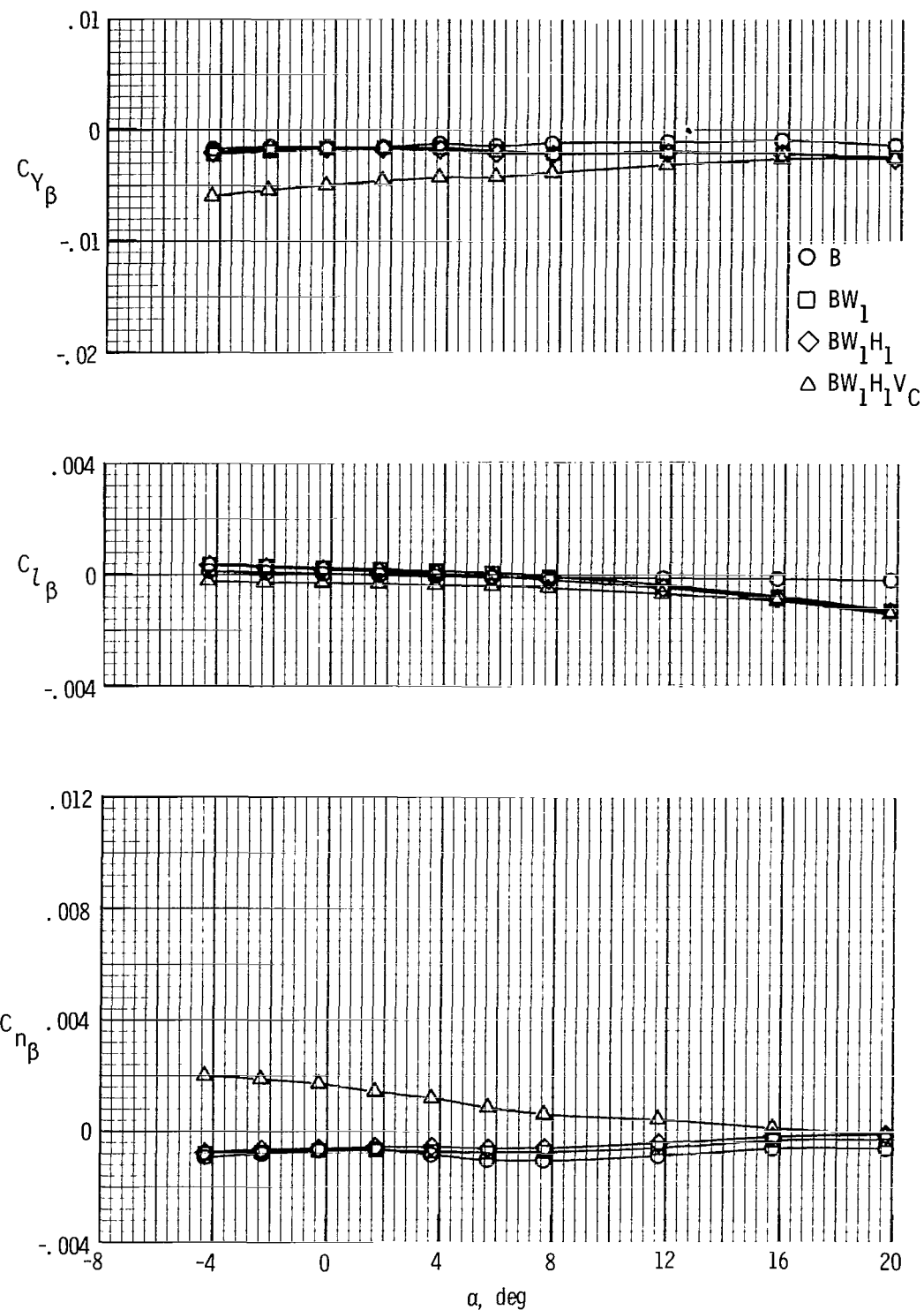
(a)  $M = 2.96.$

Figure 10.- Lateral-directional characteristics for configuration buildup.



(b)  $M = 3.96$ .

**Figure 10.- Continued.**



(c)  $M = 4.63.$

Figure 10.- Concluded.

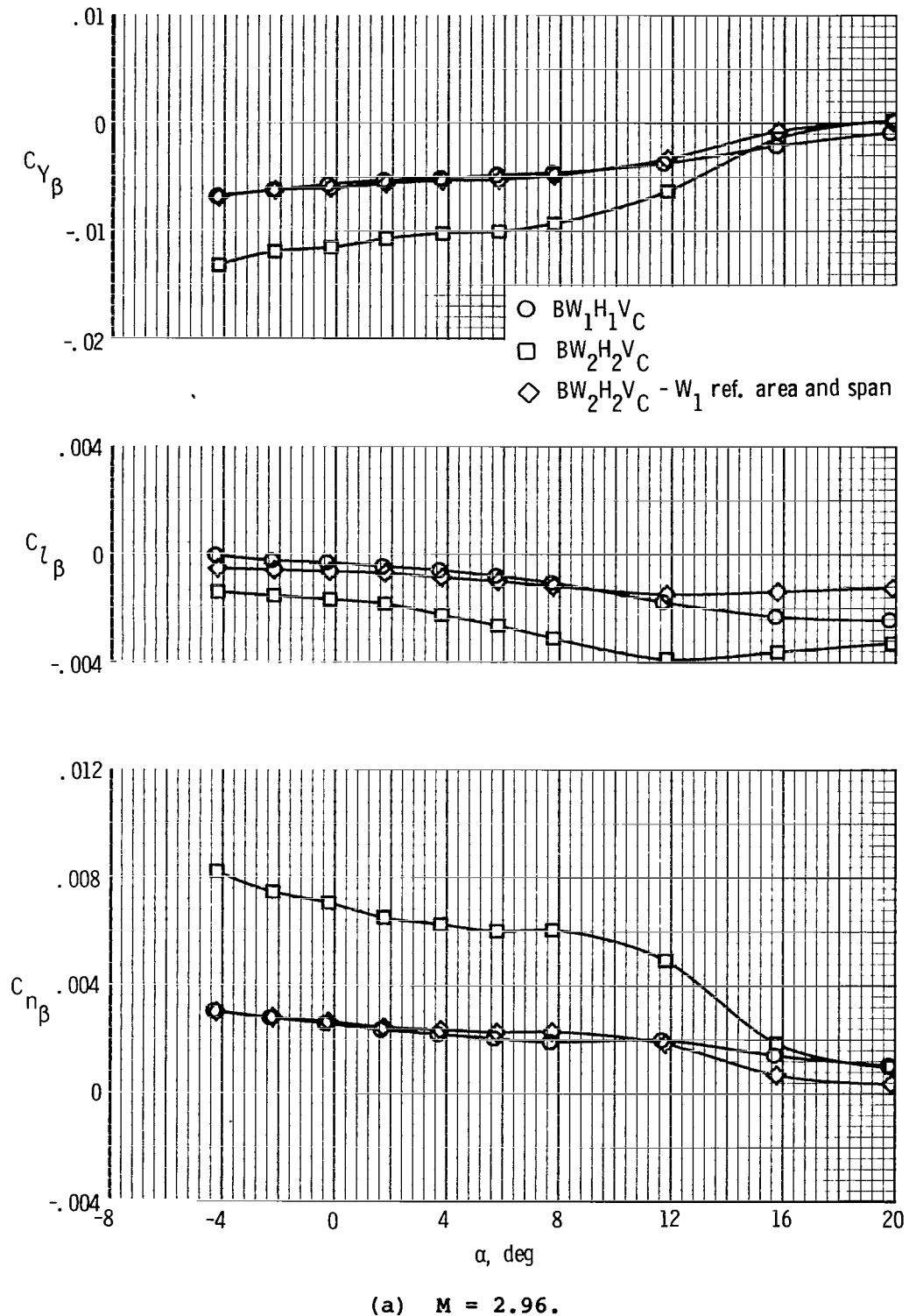
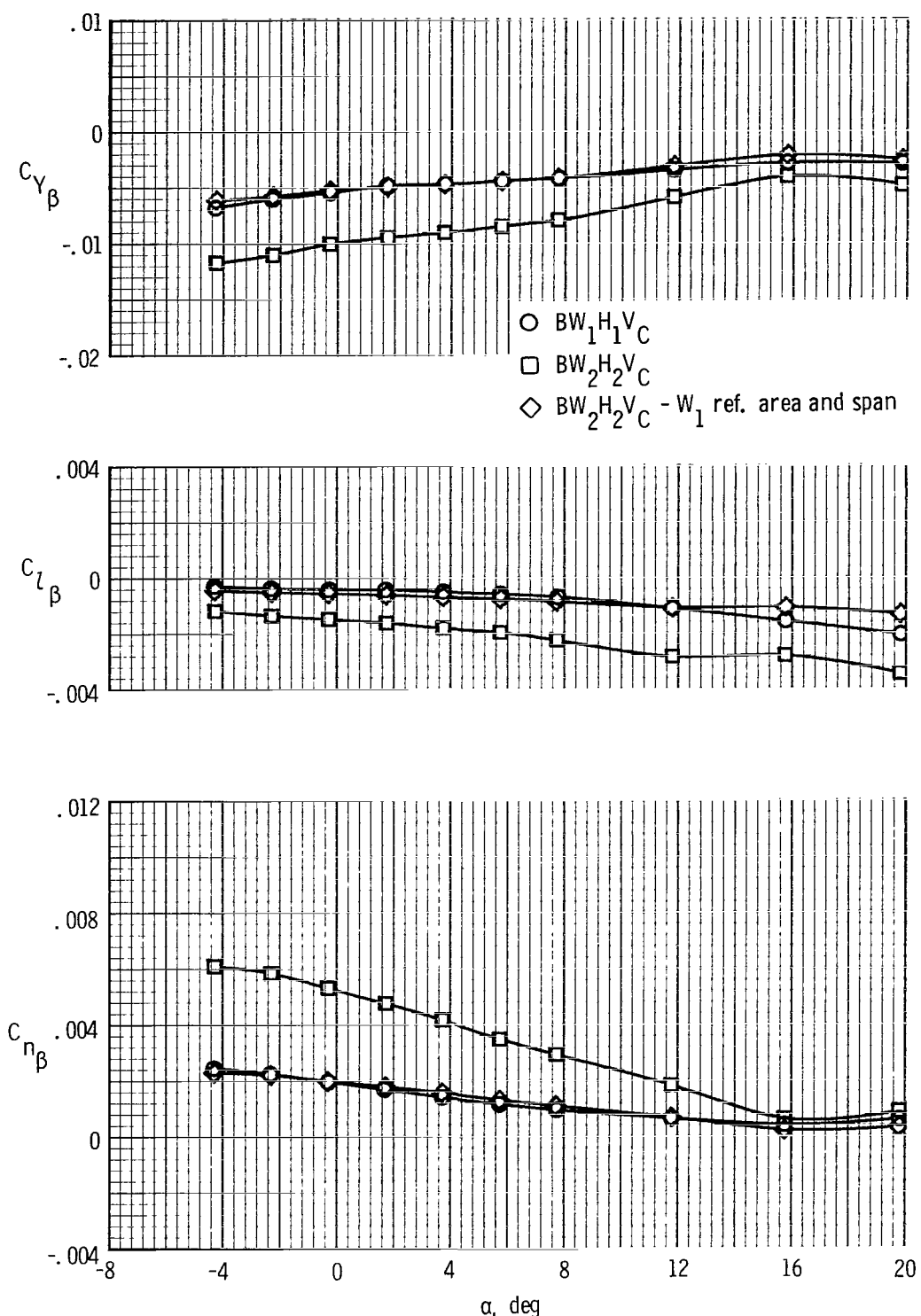
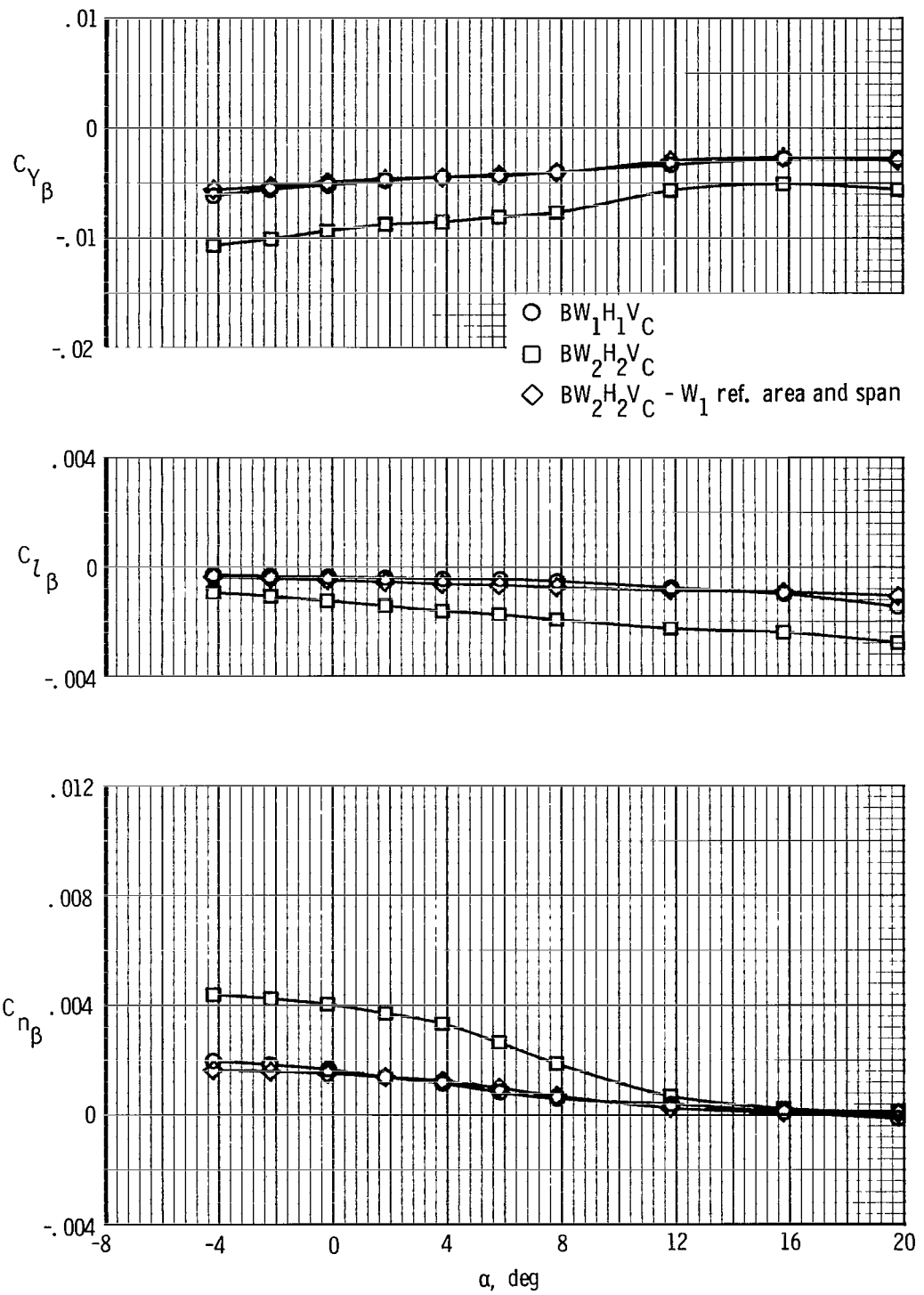


Figure 11.- Lateral-directional characteristics for  $BW_1 H_1 V_C$  and  $BW_2 H_2 V_C$  configurations.



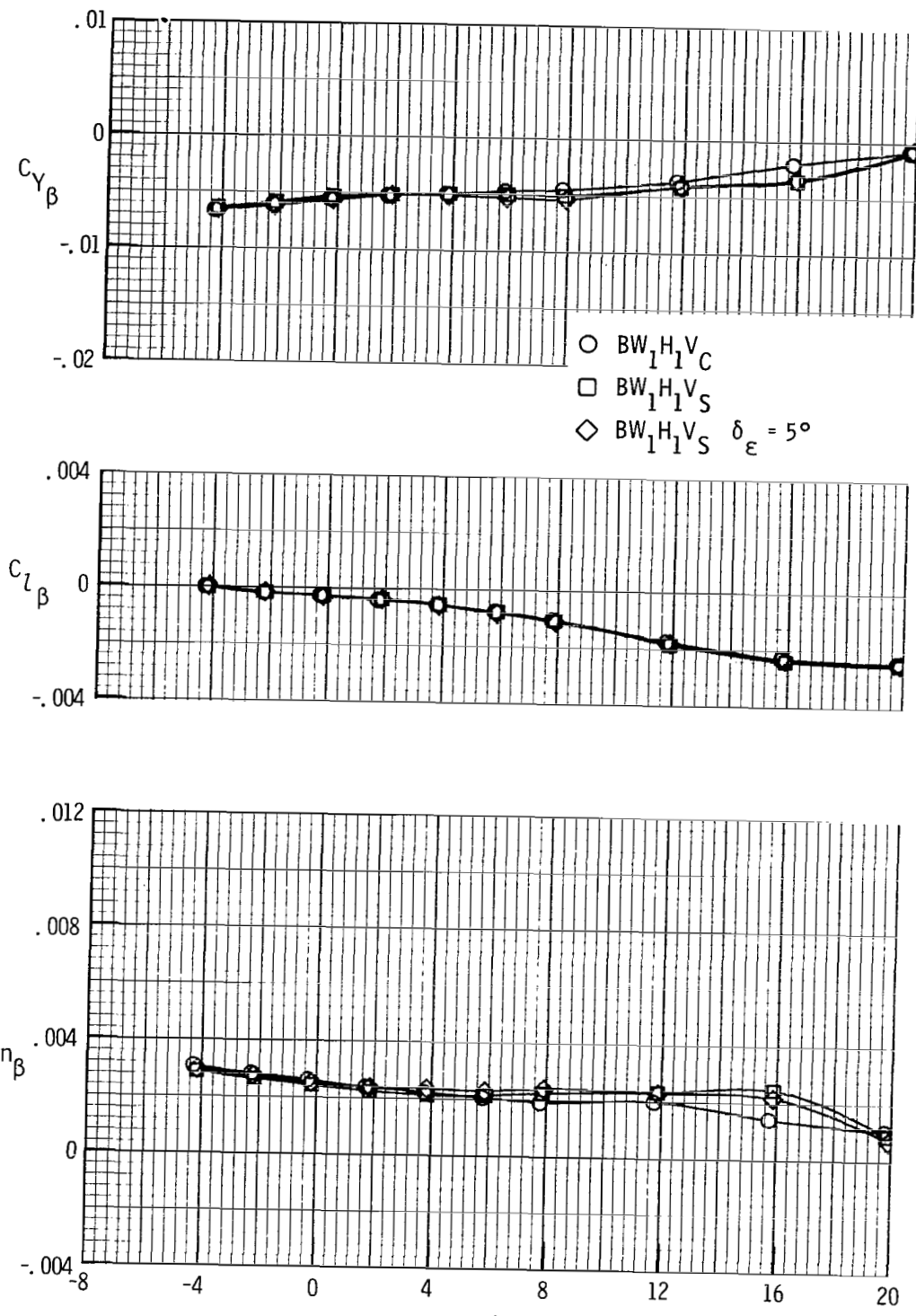
(b)  $M = 3.96$ .

Figure 11.- Continued.



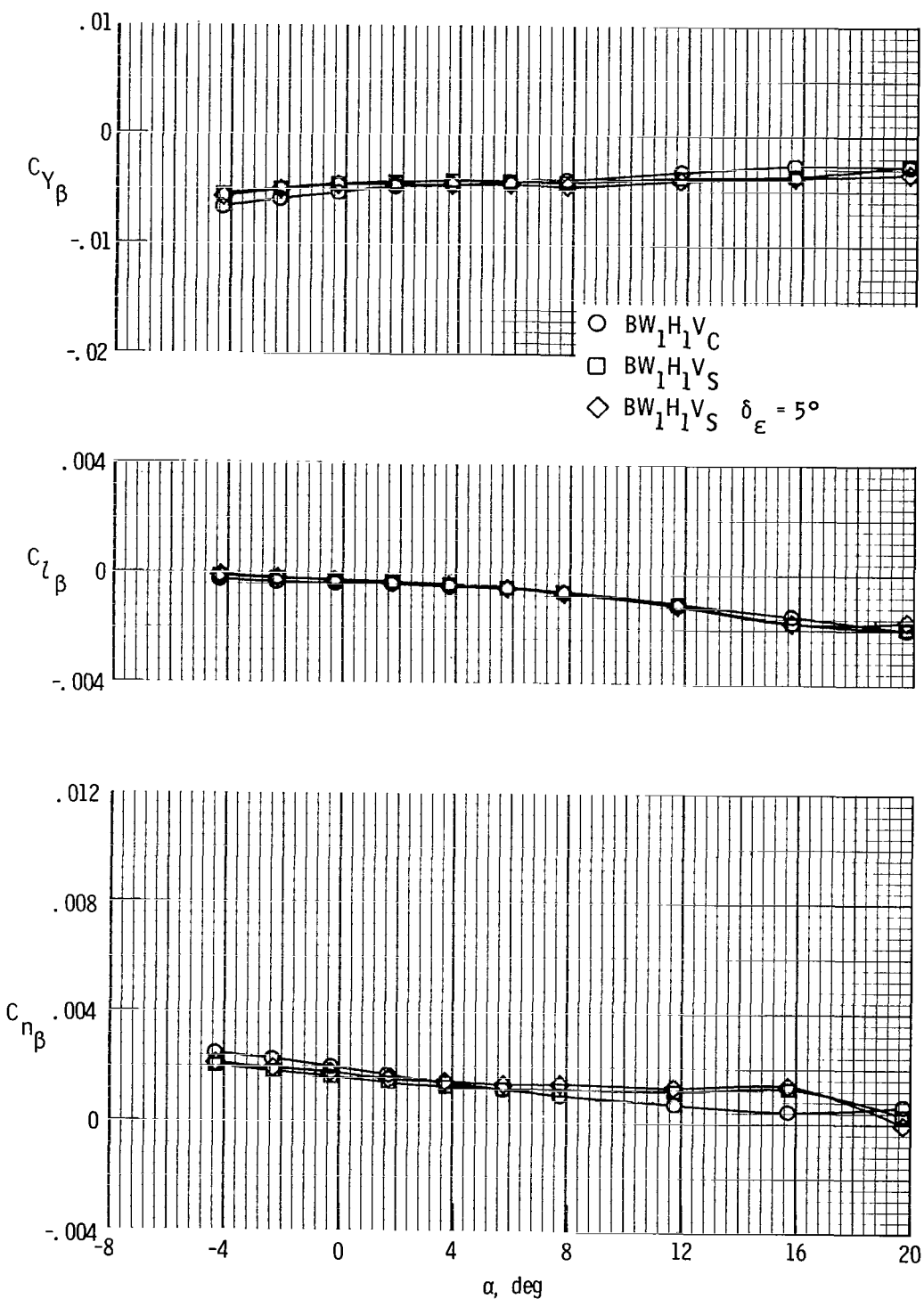
(c)  $M = 4.63.$

Figure 11.- Concluded.



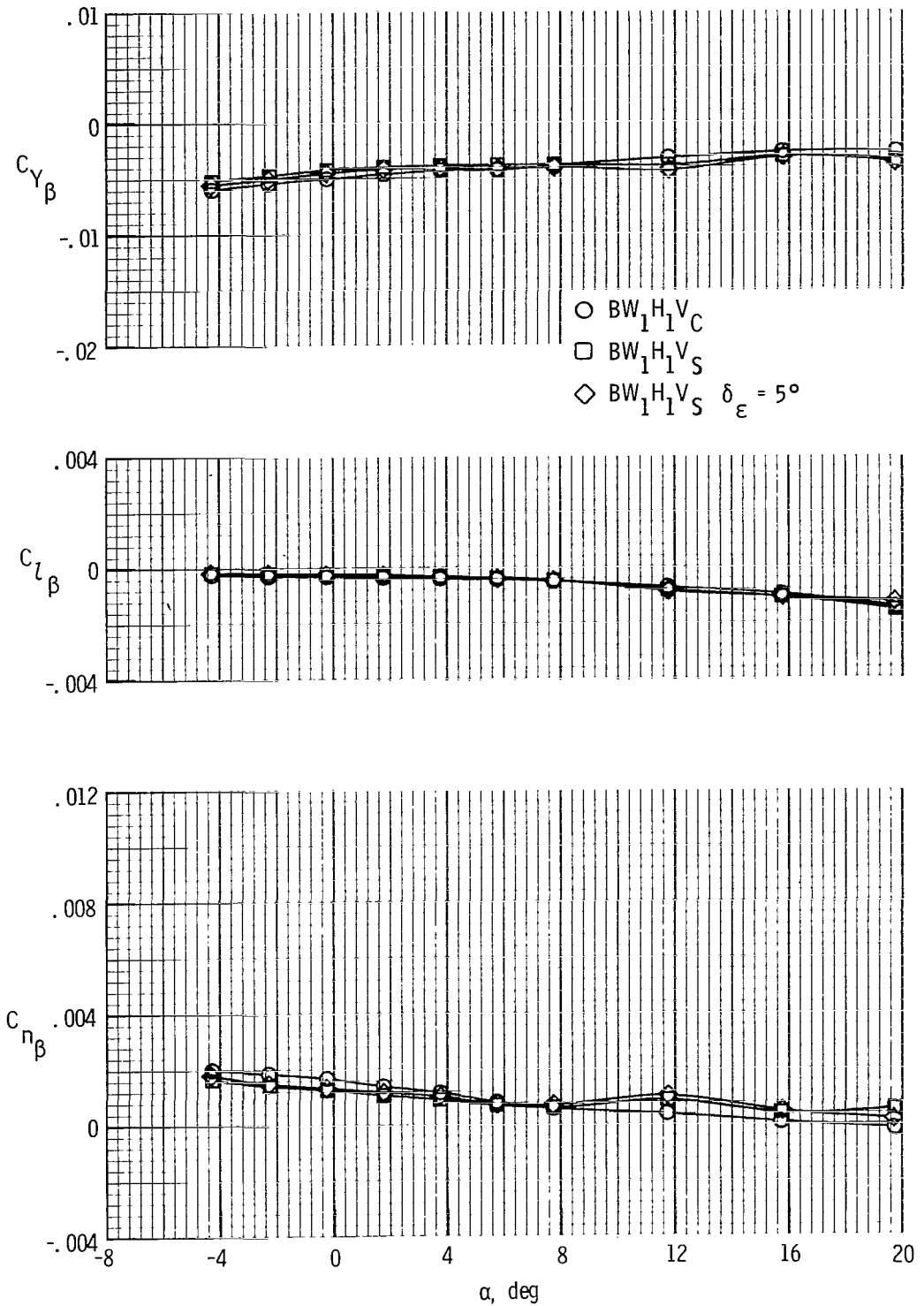
(a)  $M = 2.96$ .

Figure 12.- Lateral-directional characteristics for  $BW_1H_1V_C$  and  $BW_1H_1V_S$  configurations.



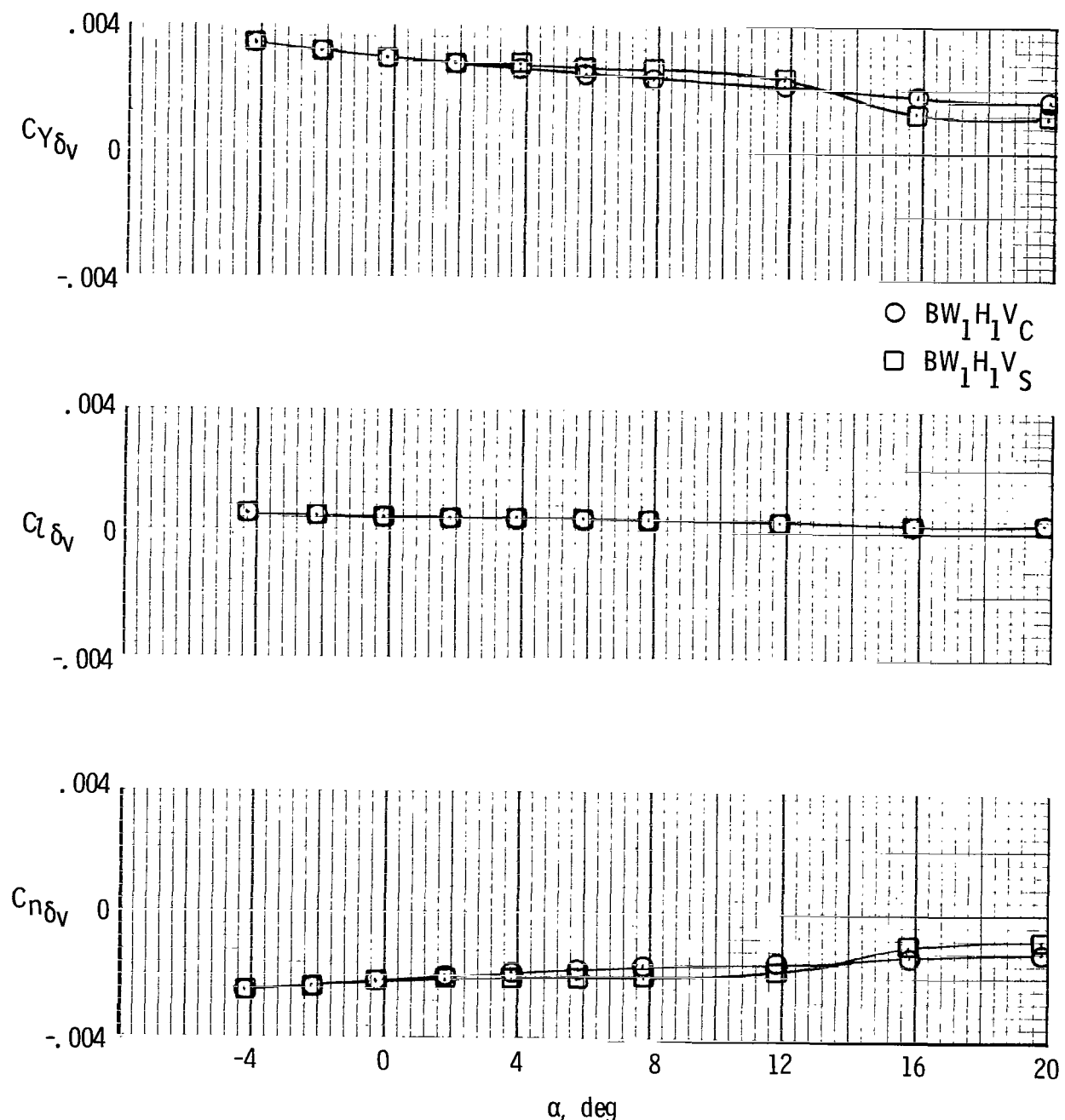
(b)  $M = 3.96$ .

Figure 12.- Continued.



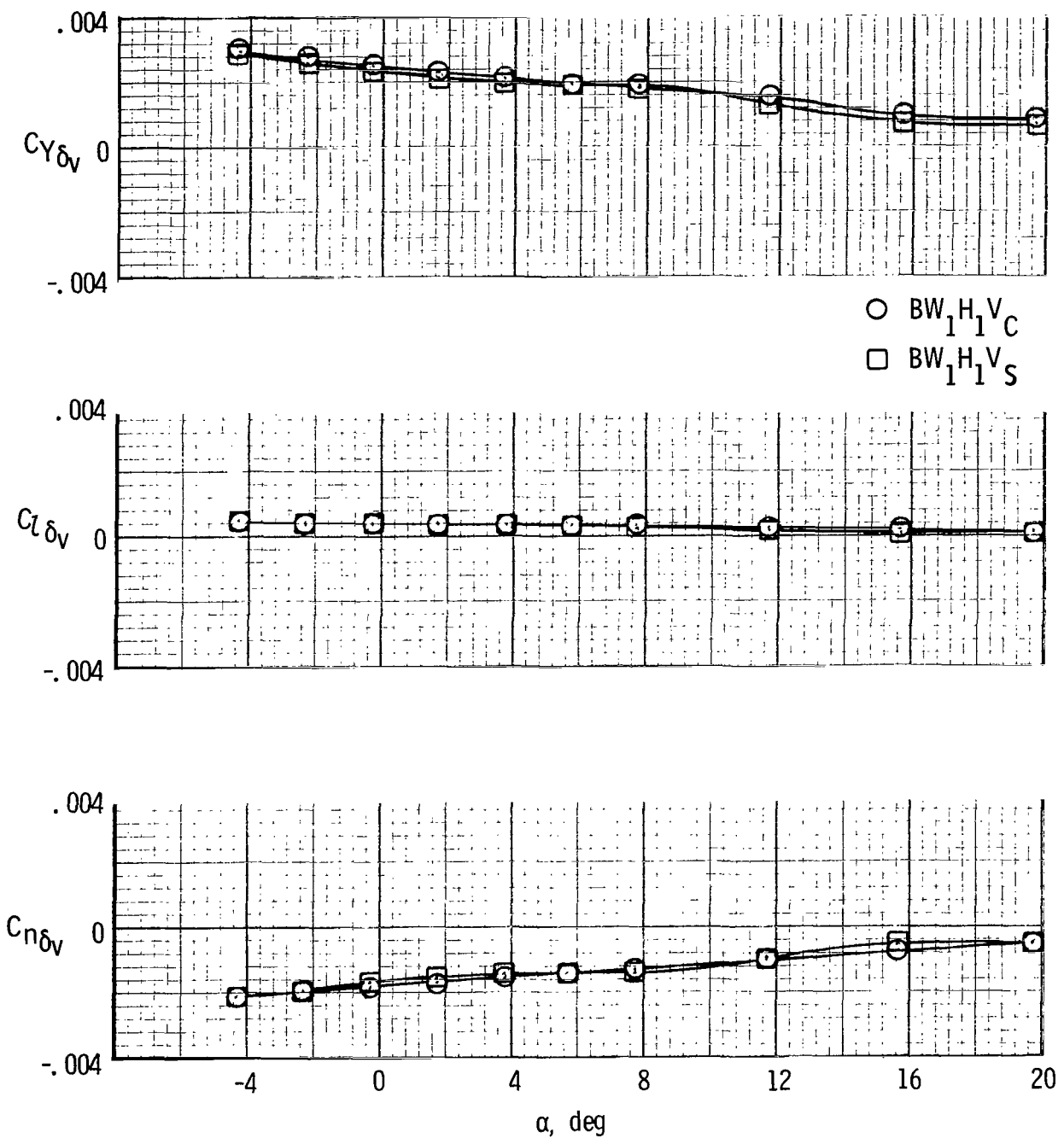
(c)  $M = 4.63$ .

Figure 12.- Concluded.



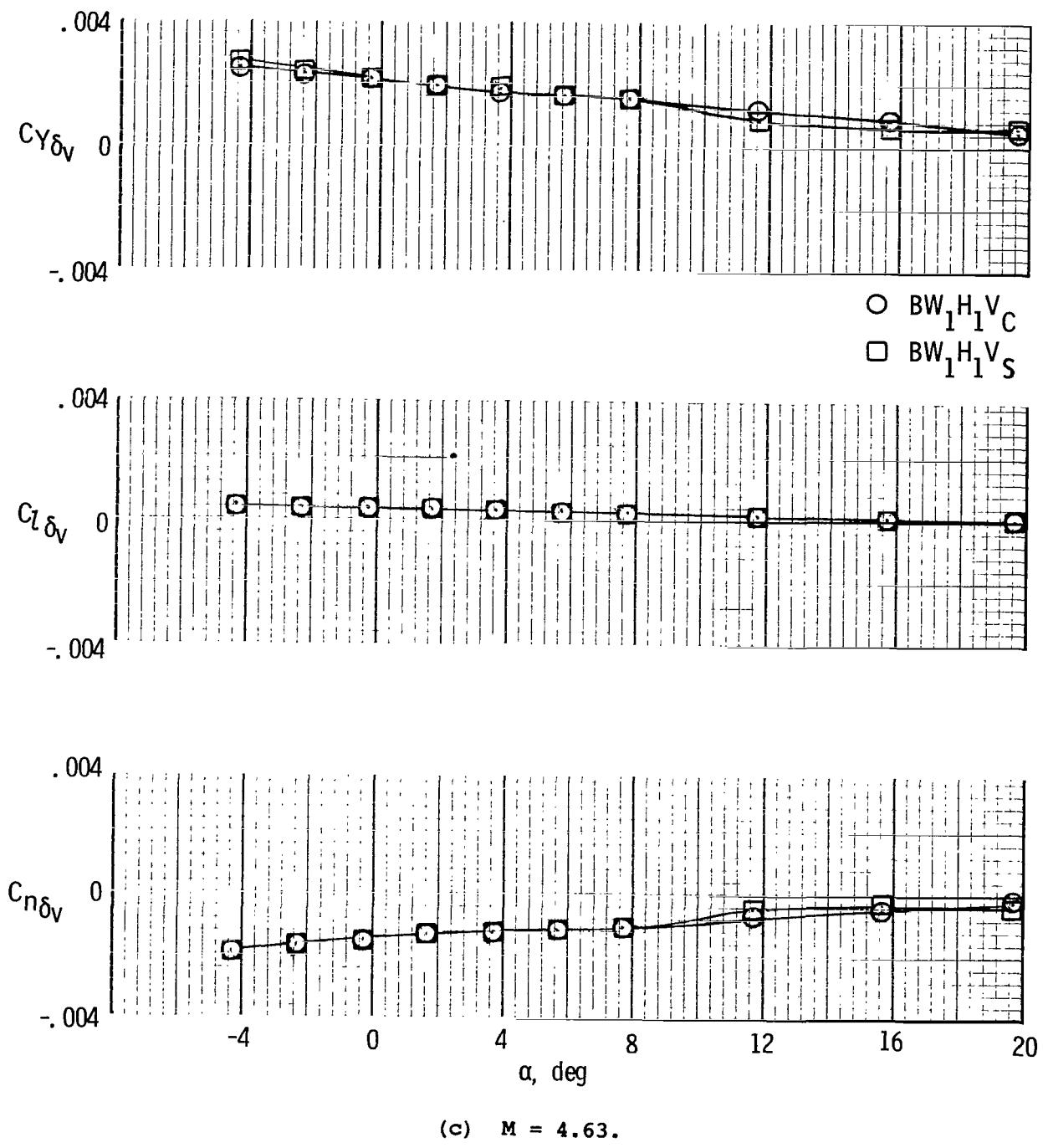
(a)  $M = 2.96$ .

Figure 13.- Yaw control for  $BW_1H_1V_C$  and  $BW_1H_1V_S$  configurations.



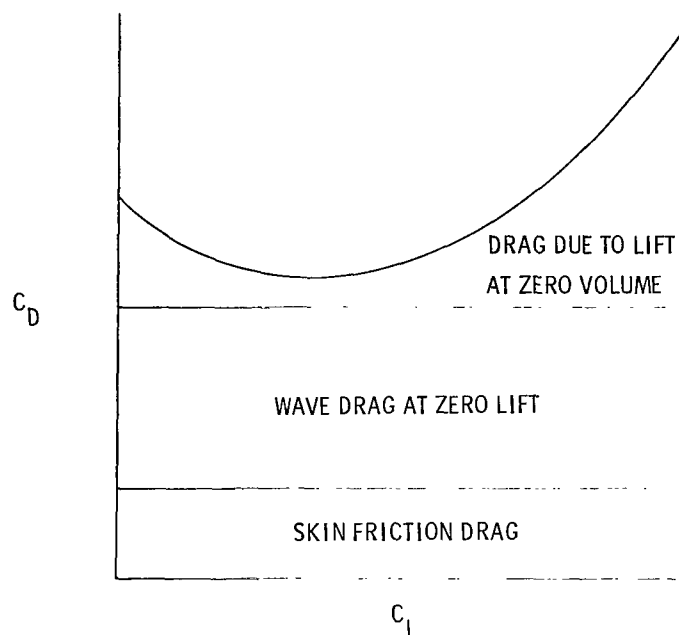
(b)  $M = 3.96$ .

Figure 13.- Continued.

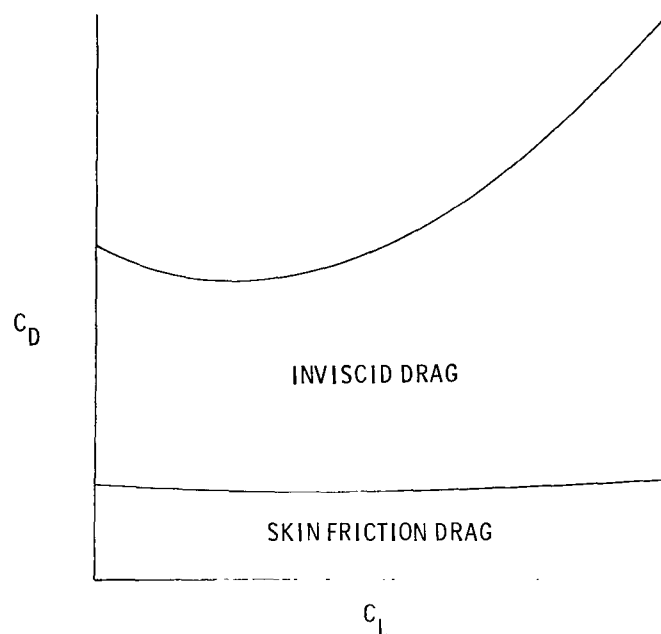


(c)  $M = 4.63.$

Figure 13.- Concluded.



(a) Supersonic linear theory.



(b) Hypersonic impact theory.

Figure 14.- Theoretical drag polar construction.

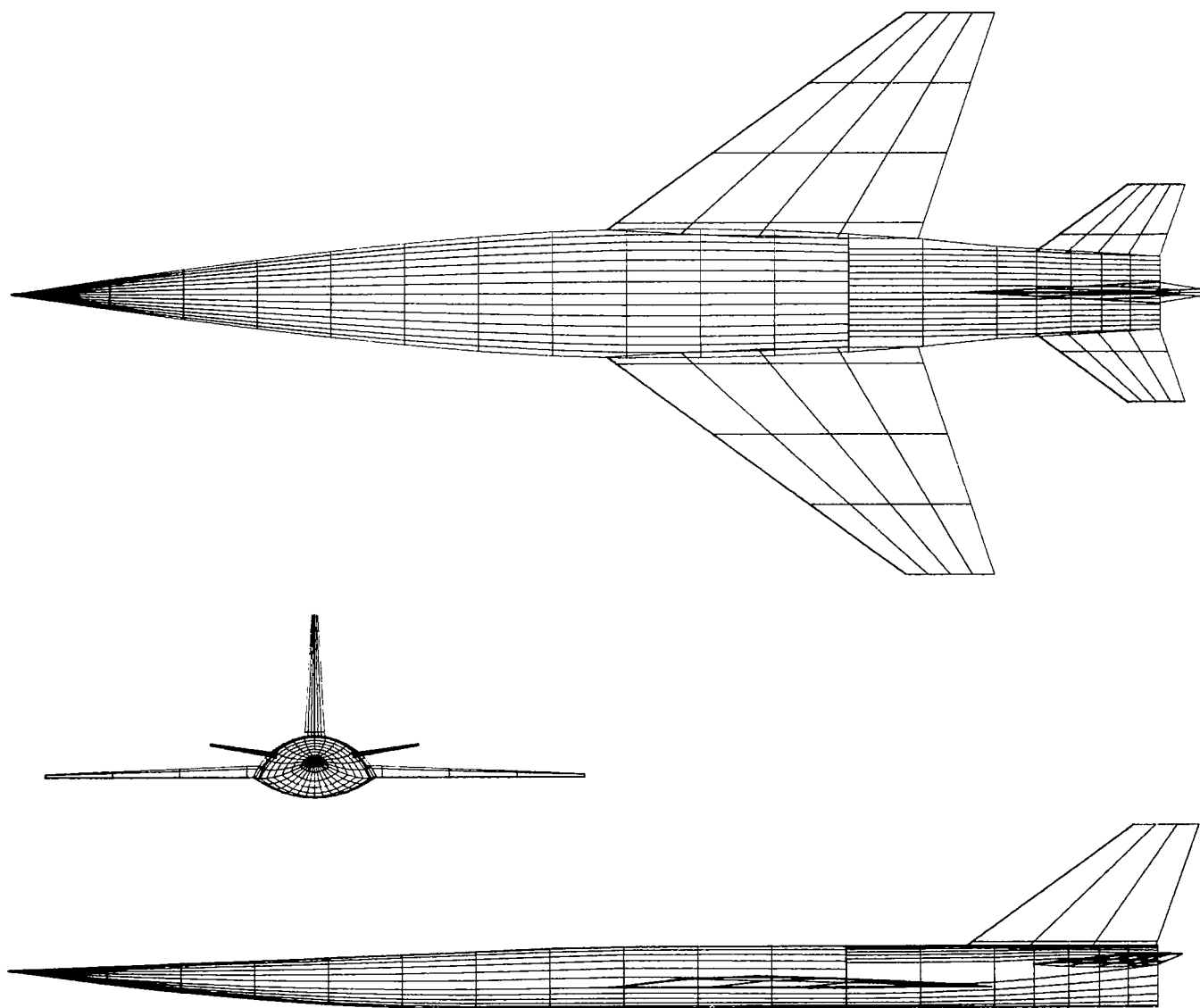
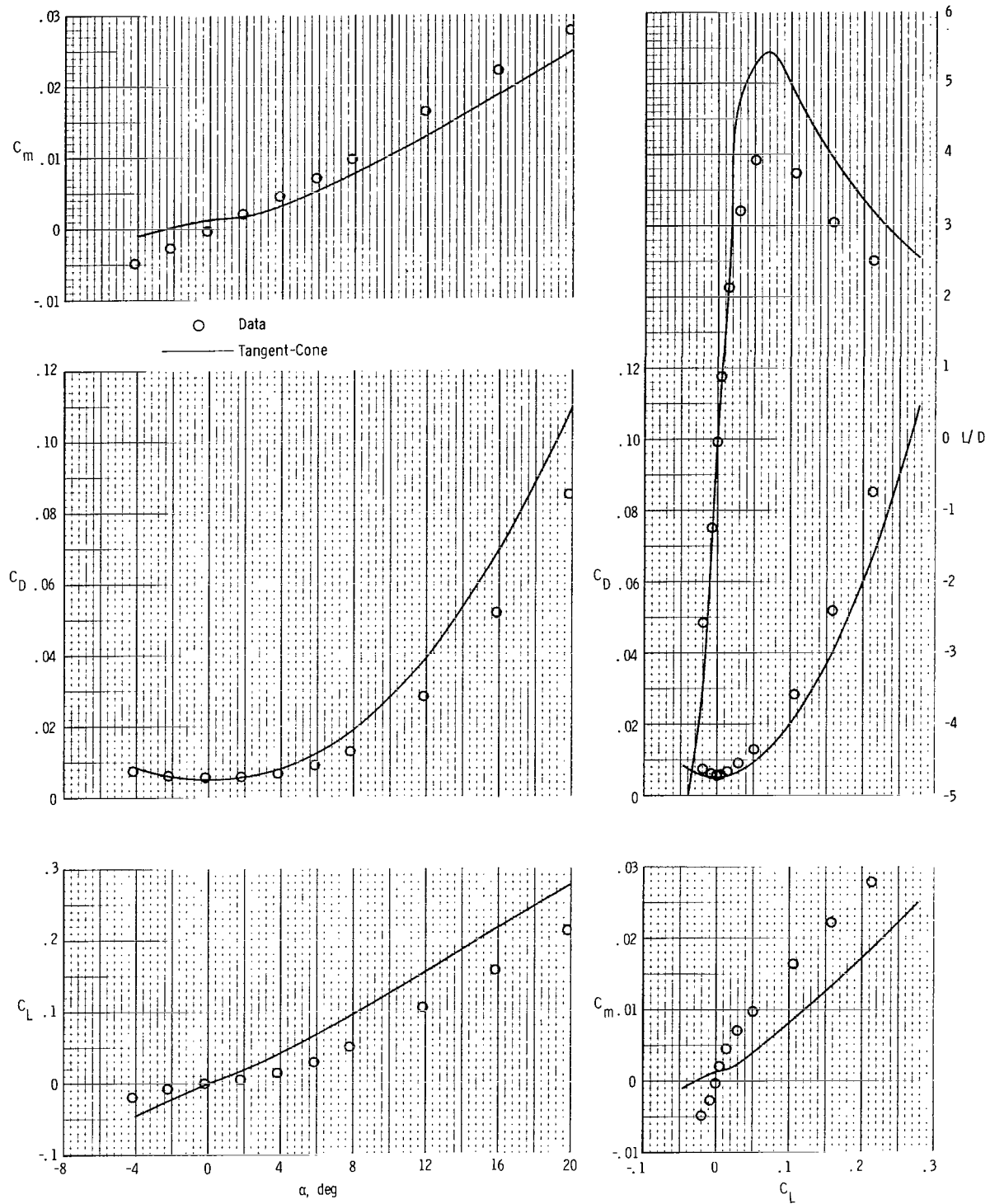
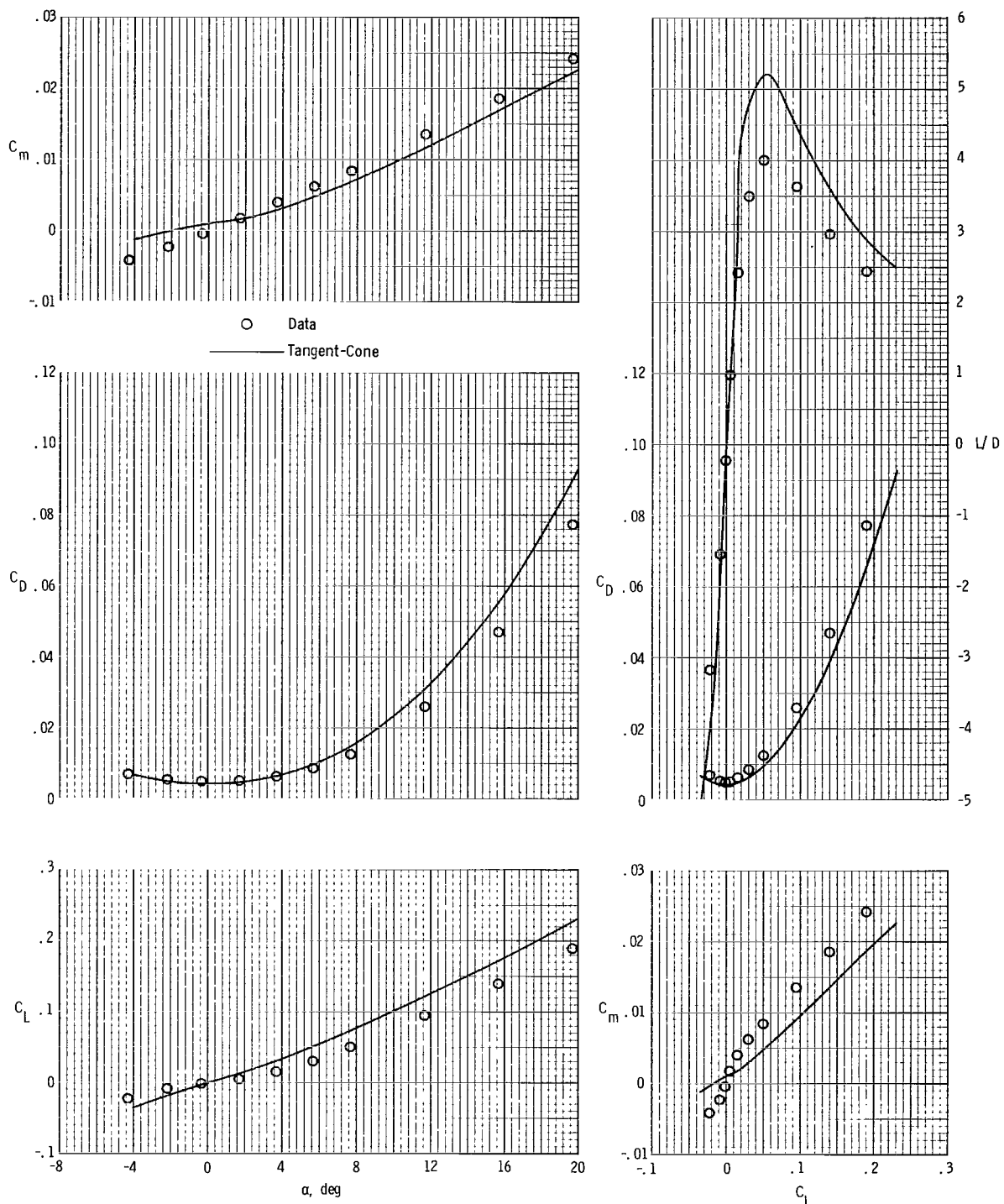


Figure 15.- Computer-generated drawing of BW<sub>1</sub>H<sub>1</sub>V<sub>C</sub> configuration.



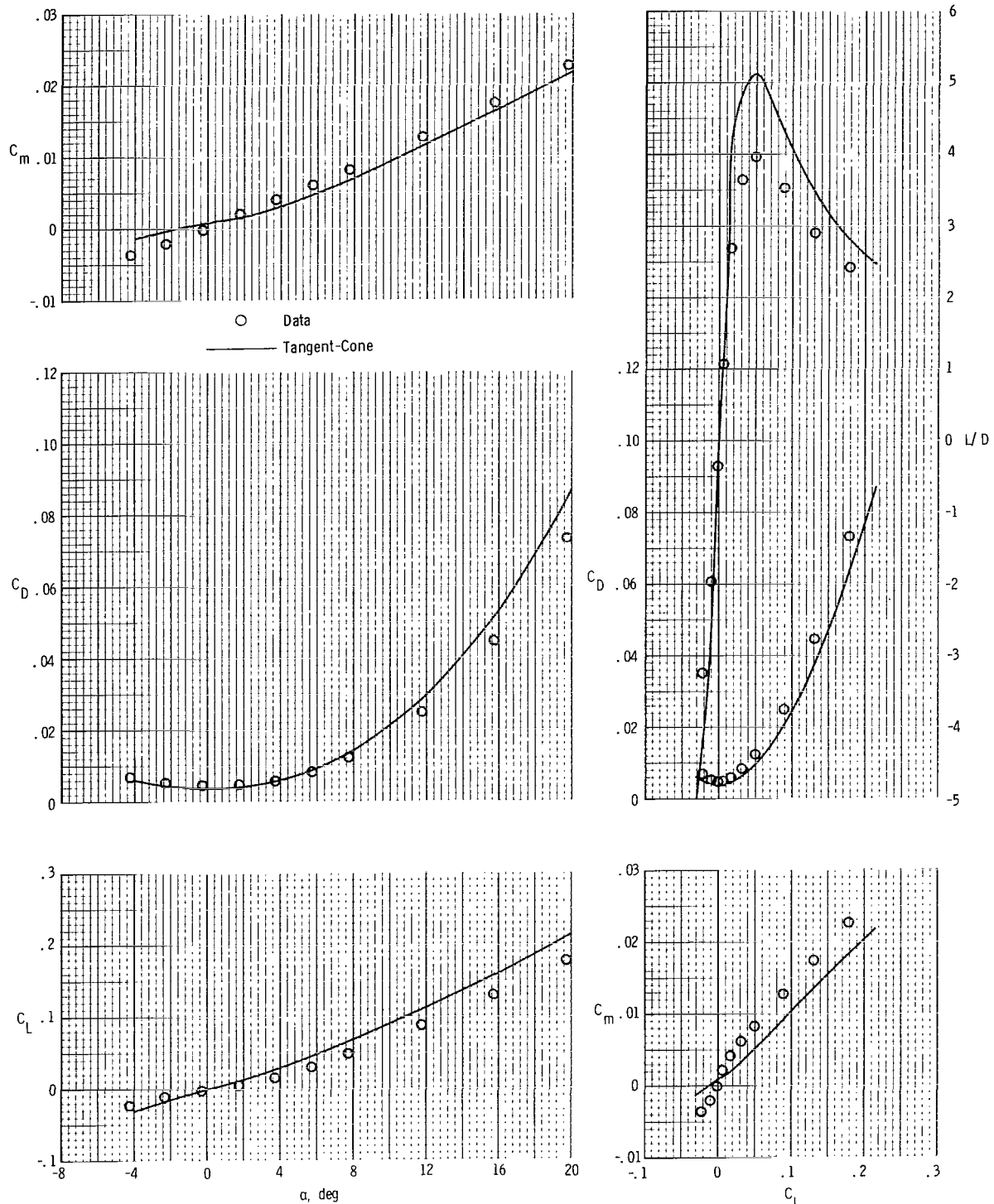
(a)  $M = 2.96$ .

Figure 16.- Comparison of theoretical and experimental longitudinal aerodynamic parameters for B configuration.



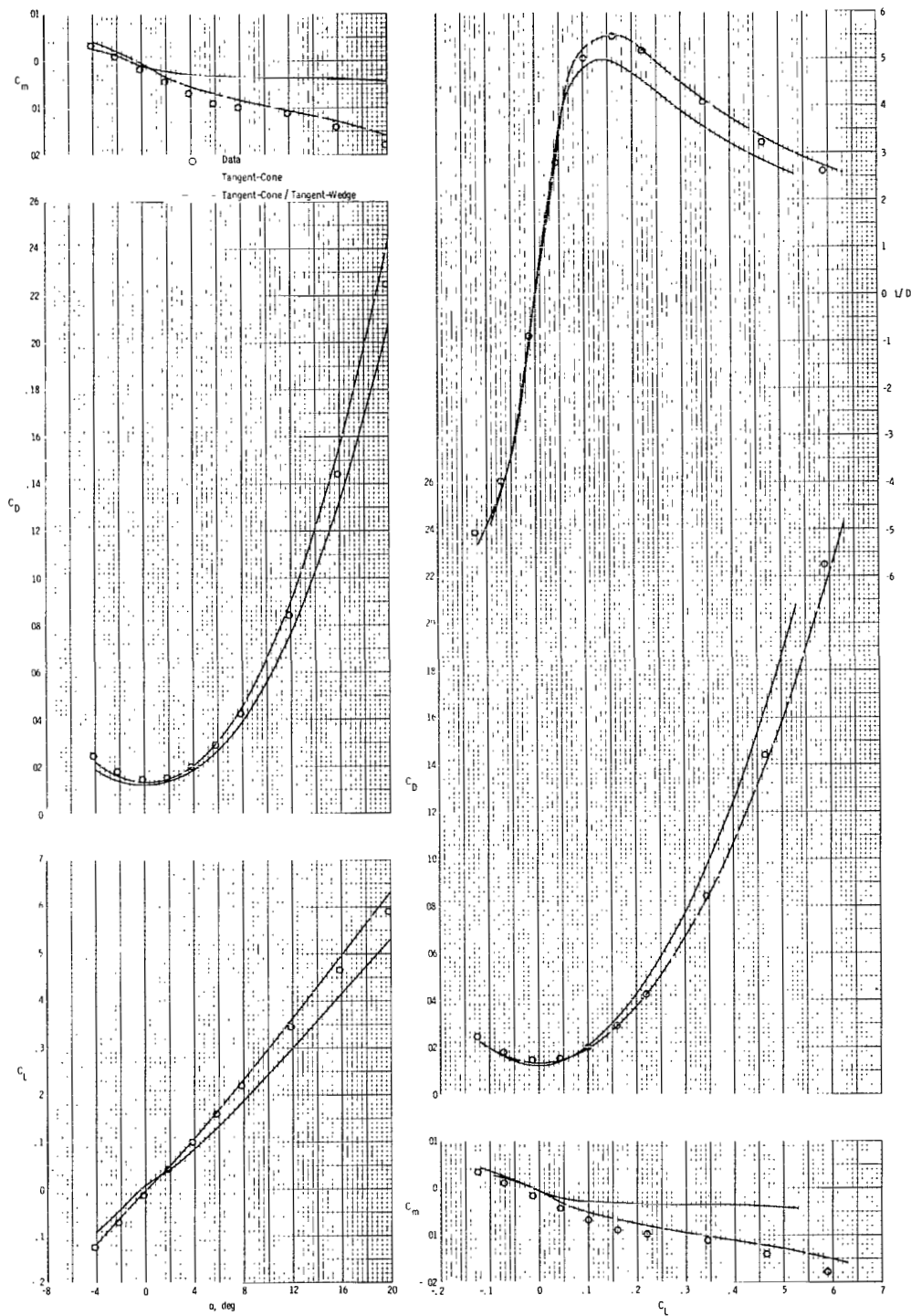
(b)  $M = 3.96$ .

Figure 16.- Continued.



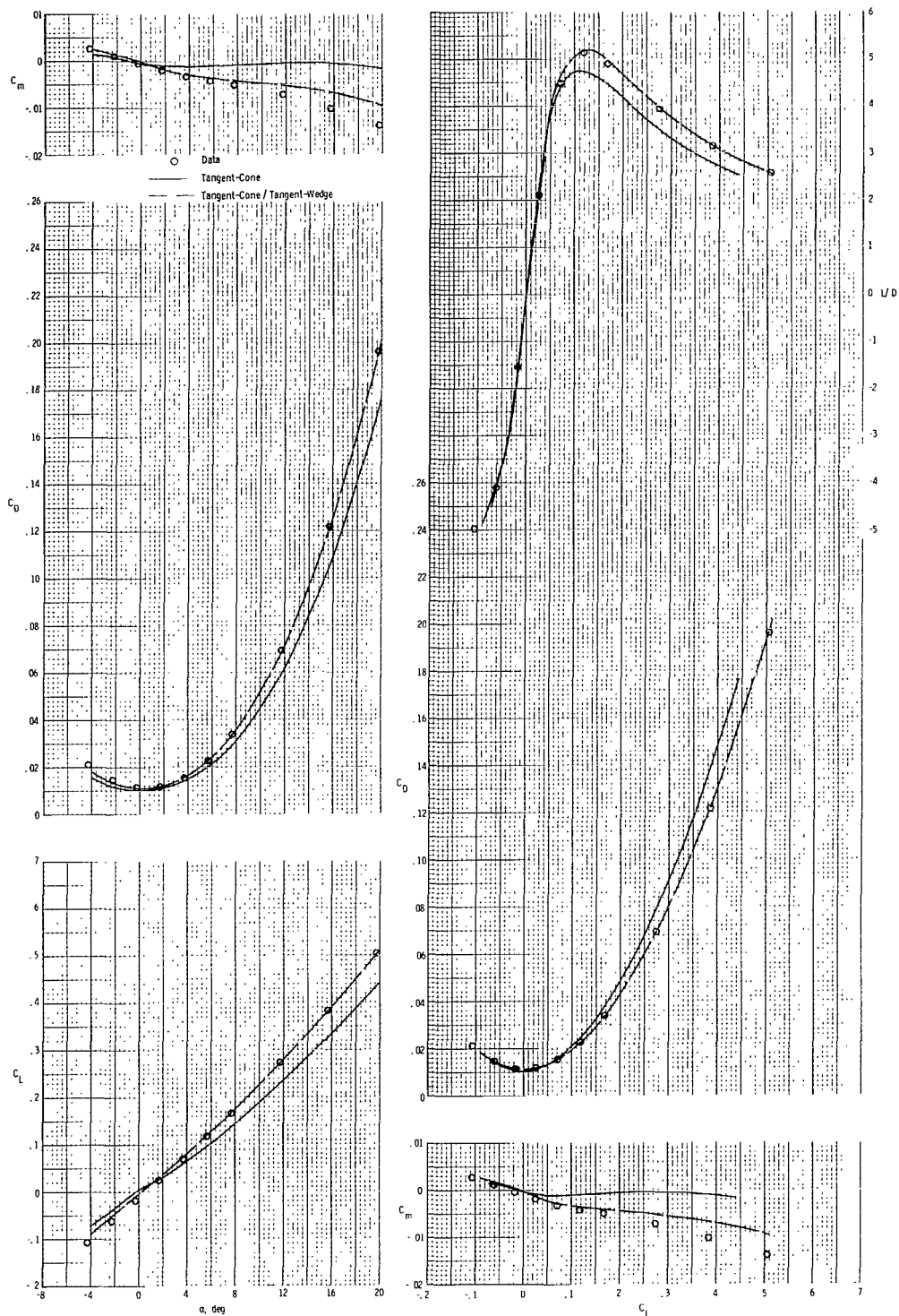
(c)  $M = 4.63.$

**Figure 16.- Concluded.**



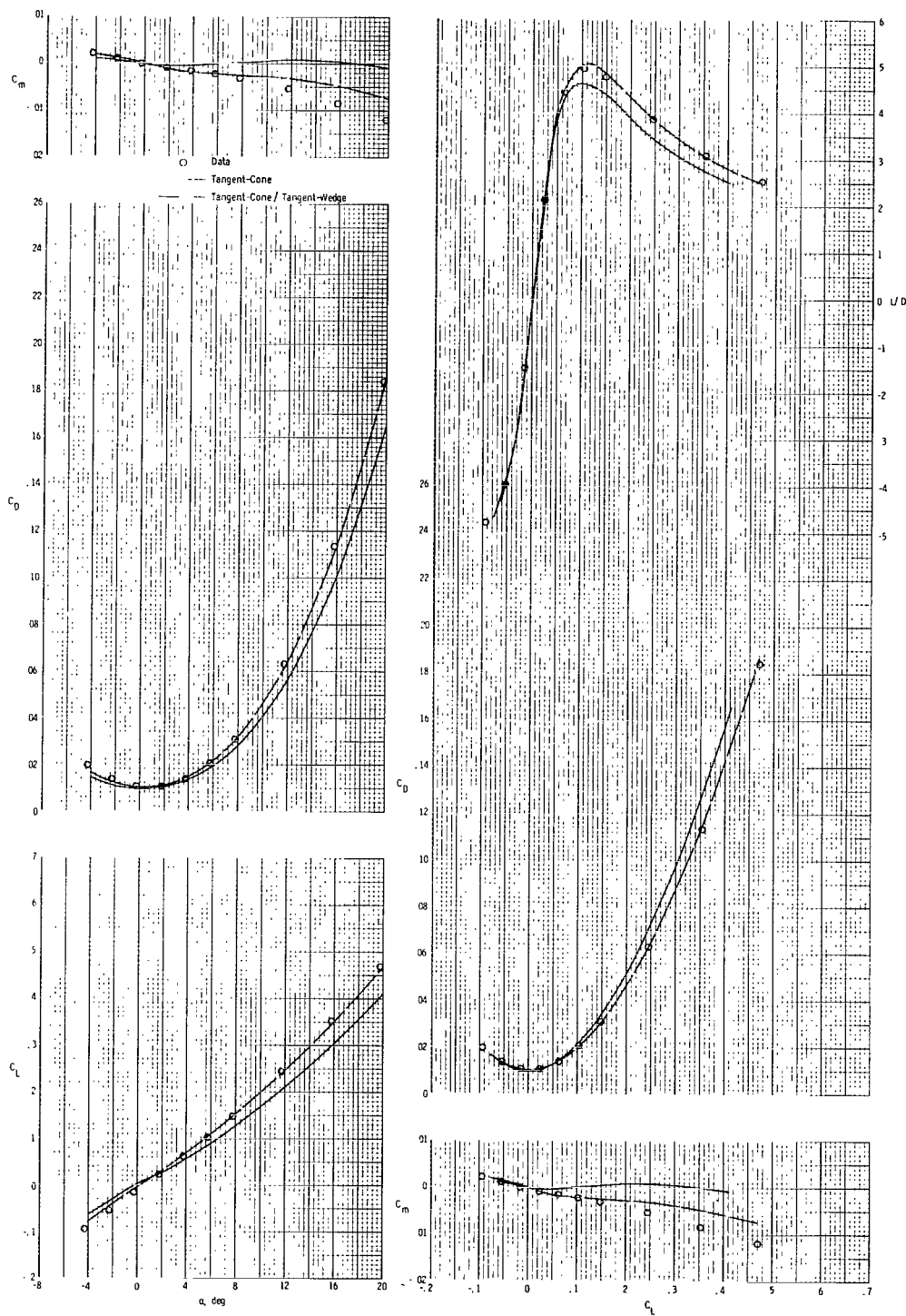
(a)  $M = 2.96$ .

Figure 17.- Comparison of theoretical and experimental longitudinal aerodynamic parameters for BW<sub>1</sub> configuration.



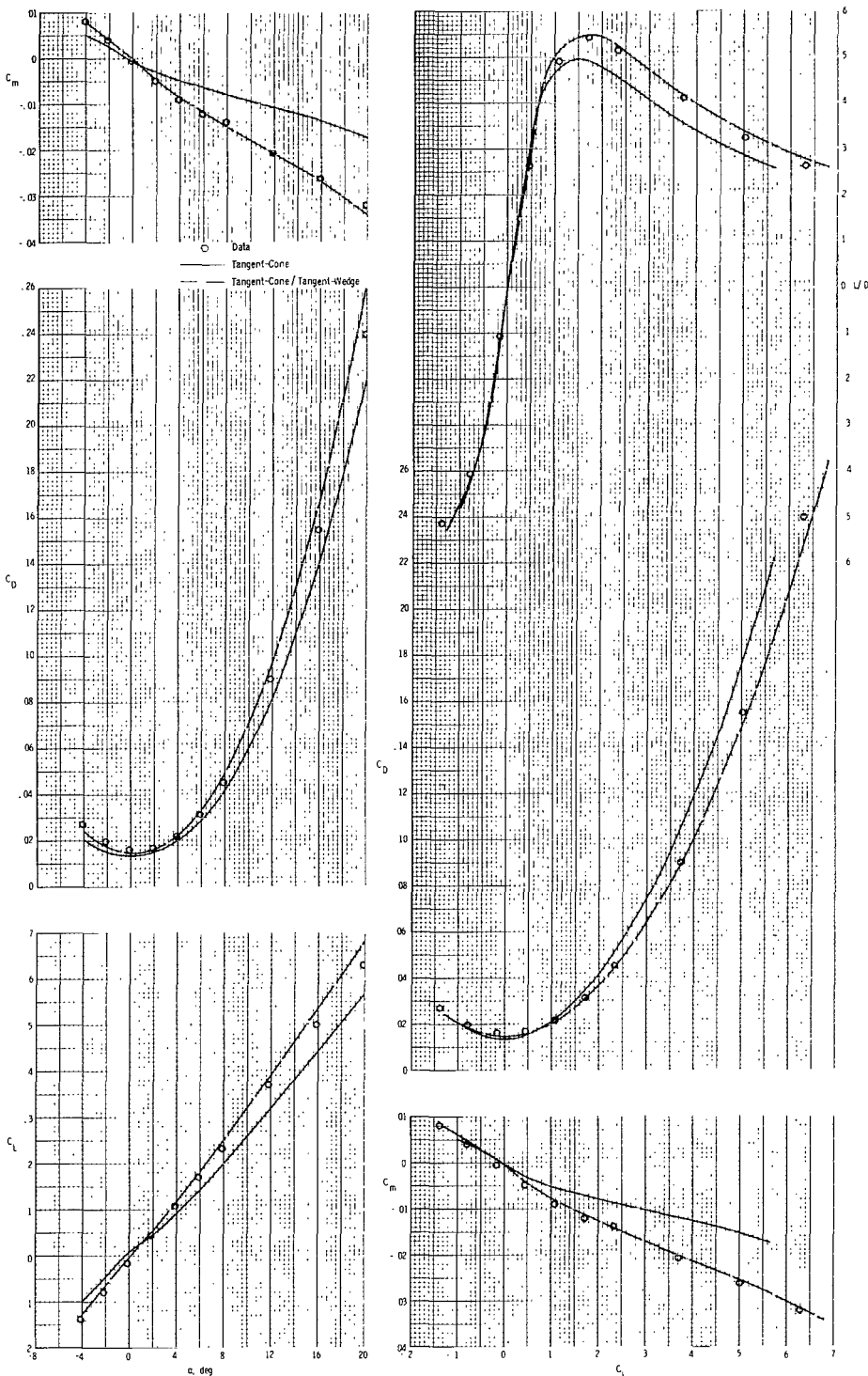
(b)  $M = 3.96$ .

Figure 17.- Continued.



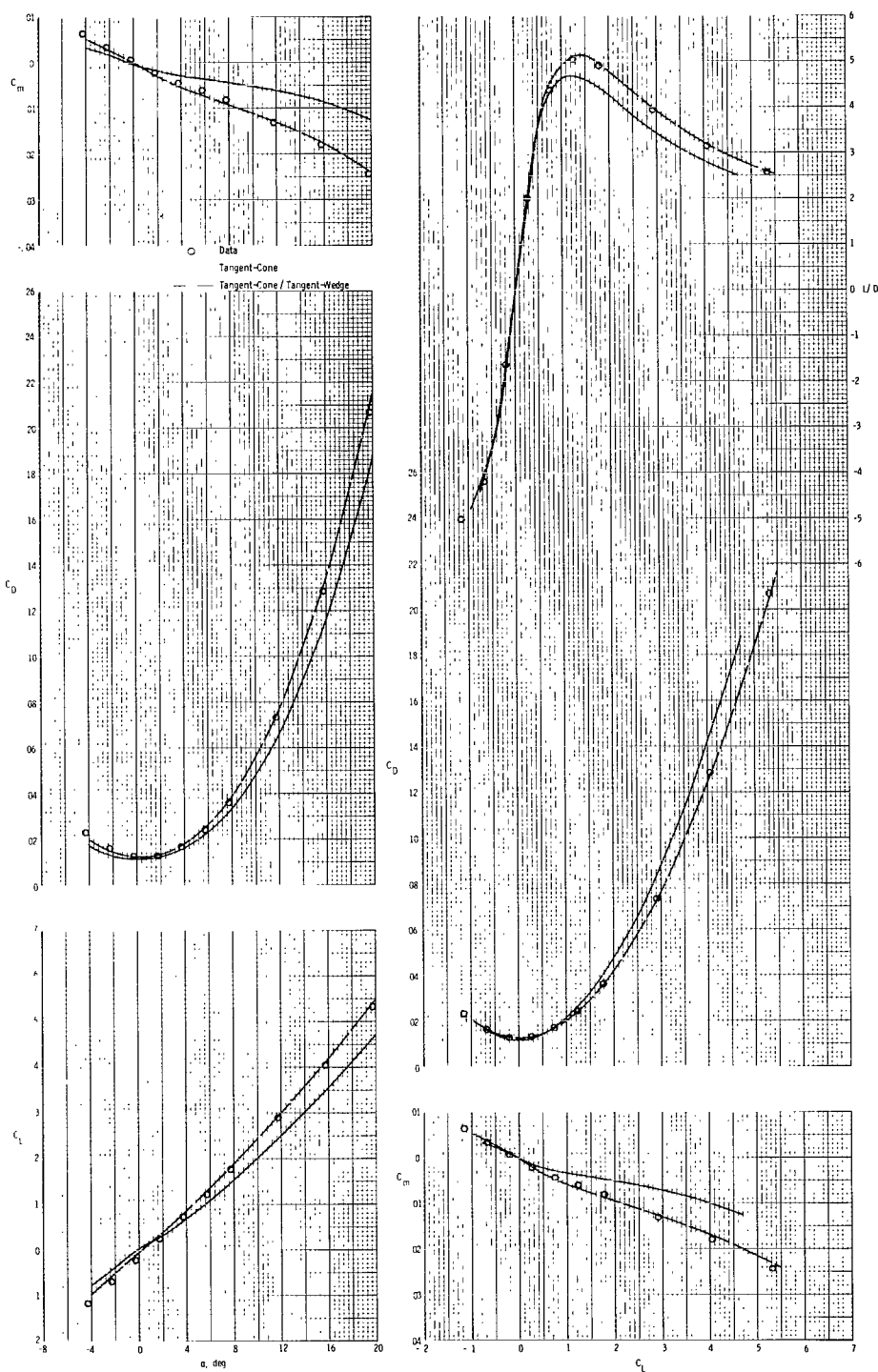
(c)  $M = 4.63.$

Figure 17.- Concluded.



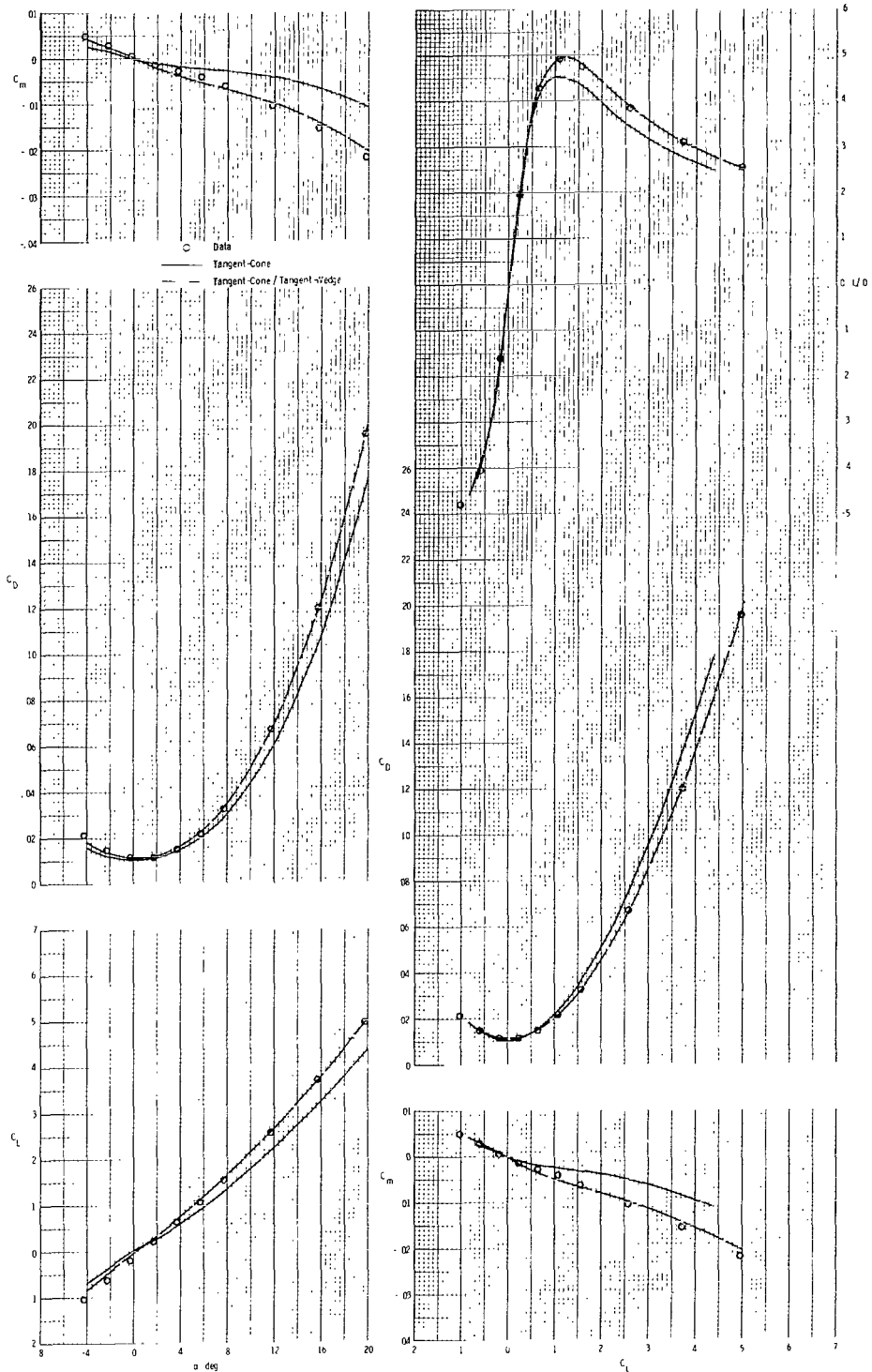
(a)  $M = 2.96$ .

Figure 18.- Comparison of theoretical and experimental longitudinal aerodynamic parameters for BW<sub>1</sub>H<sub>1</sub> configuration.



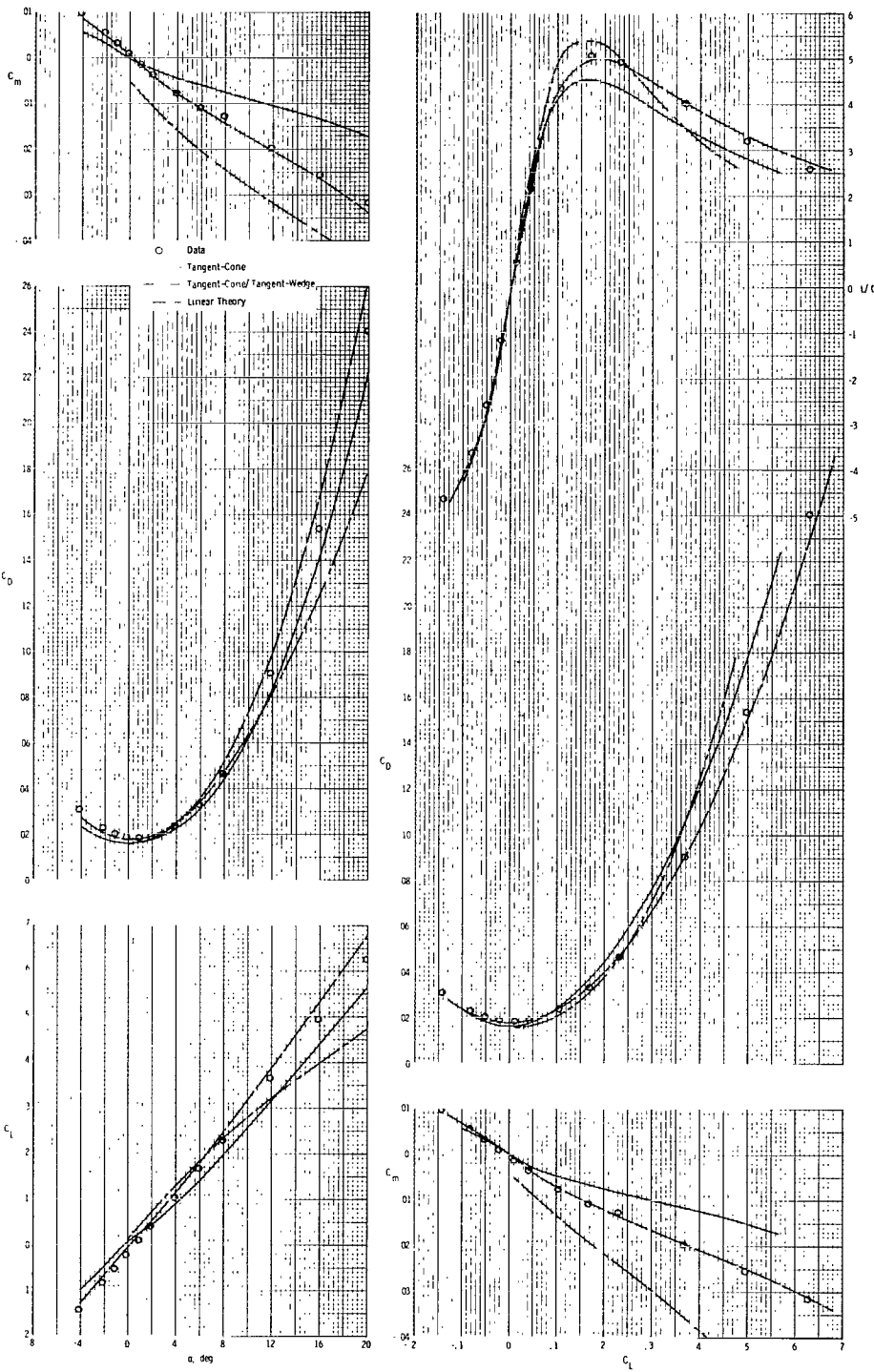
(b)  $M = 3.96$ .

Figure 18.- Continued.



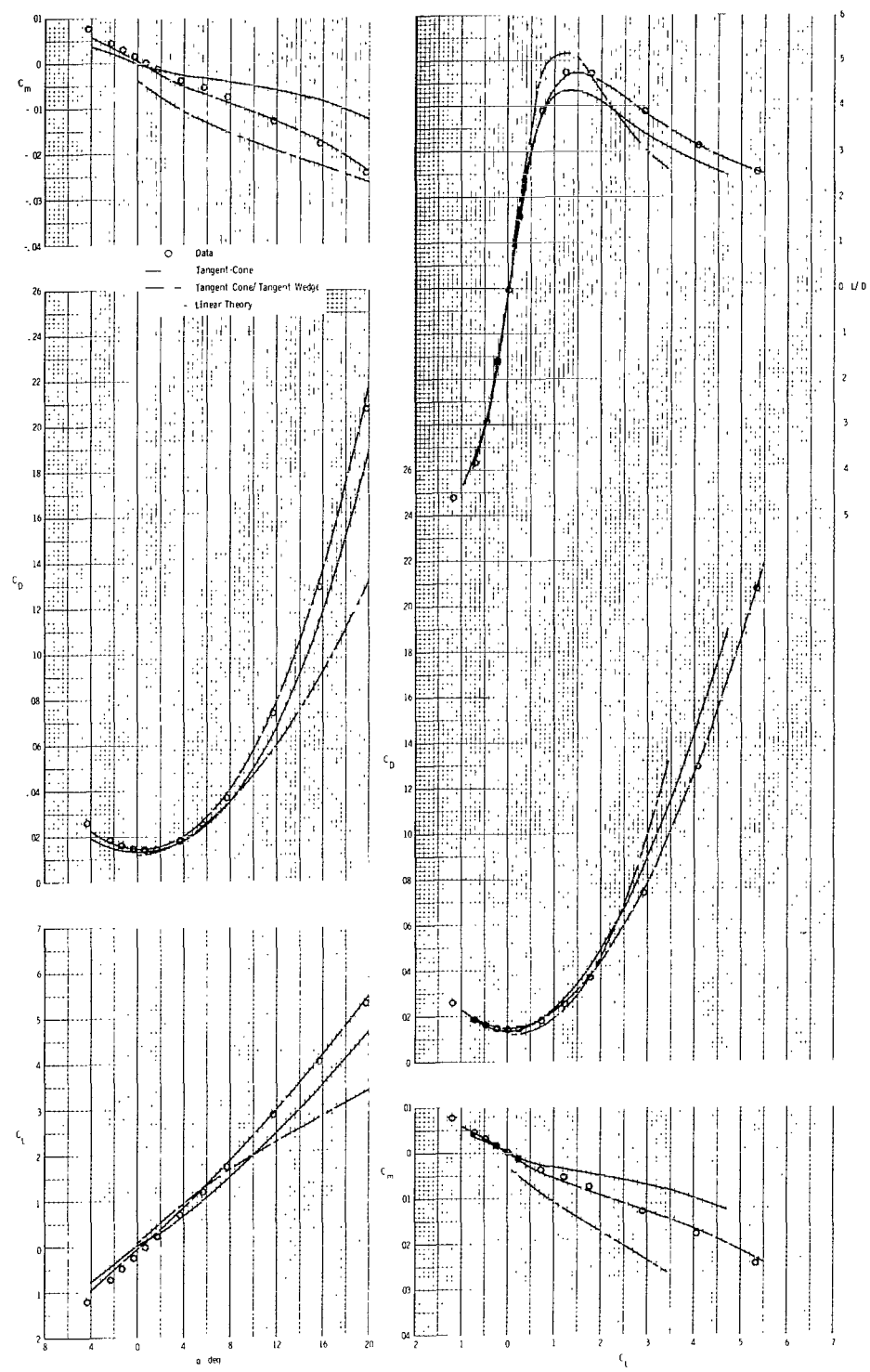
(c)  $M = 4.63.$

Figure 18.- Concluded.



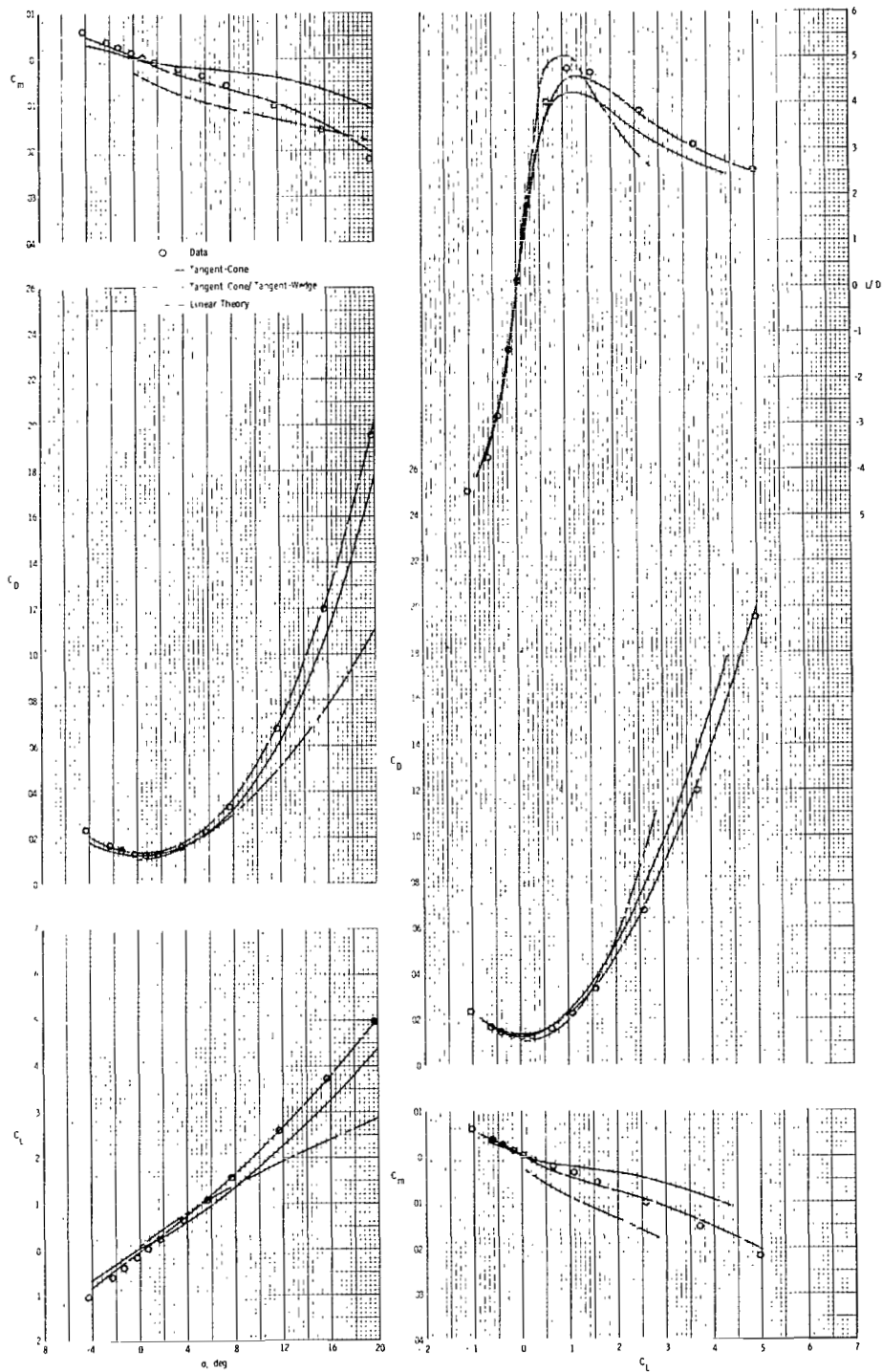
(a)  $M = 2.96.$

Figure 19.- Comparison of theoretical and experimental longitudinal aerodynamic parameters for BW<sub>1</sub>H<sub>1</sub>V<sub>C</sub> configuration.



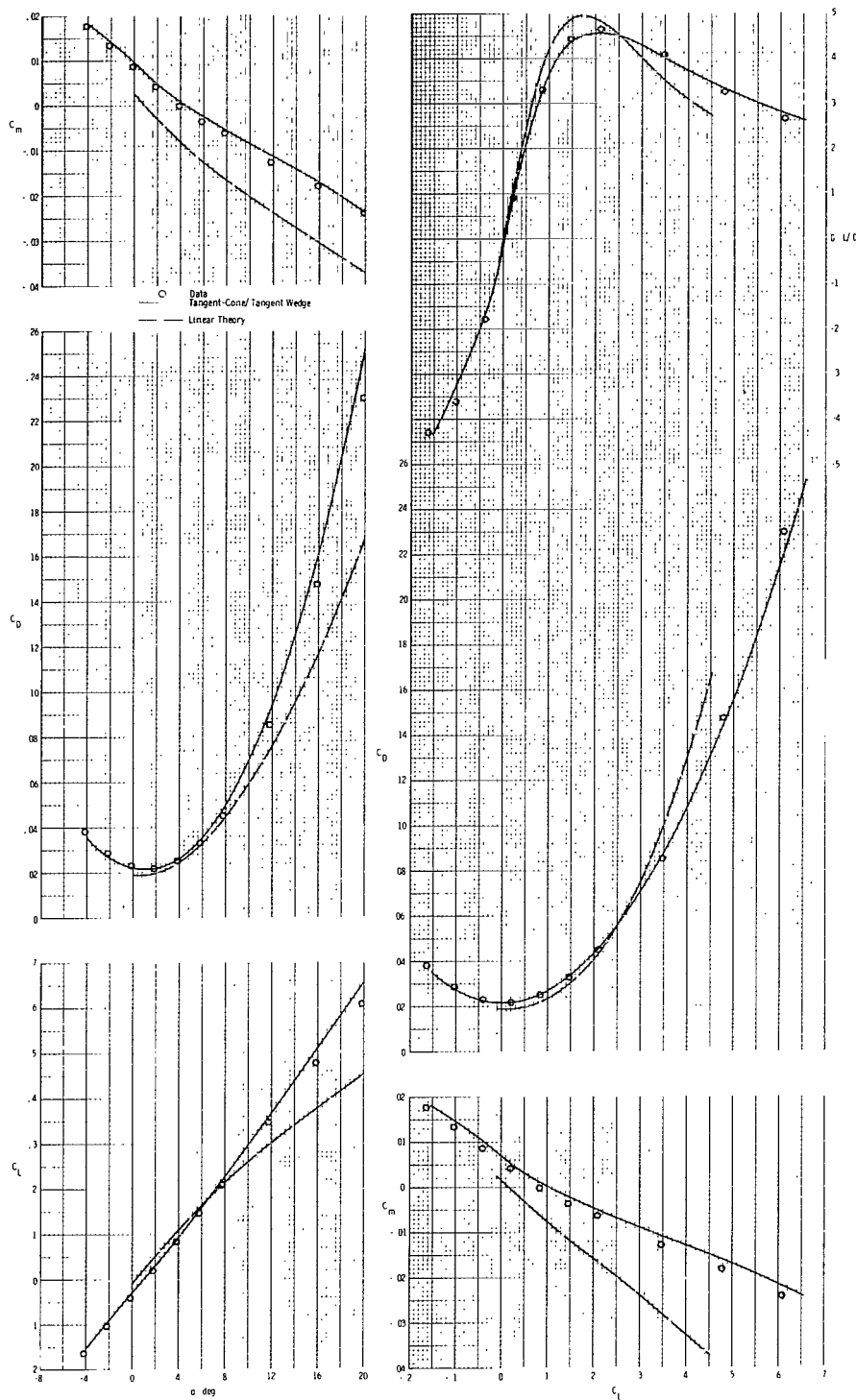
(b)  $M = 3.96$ .

Figure 19.- Continued.



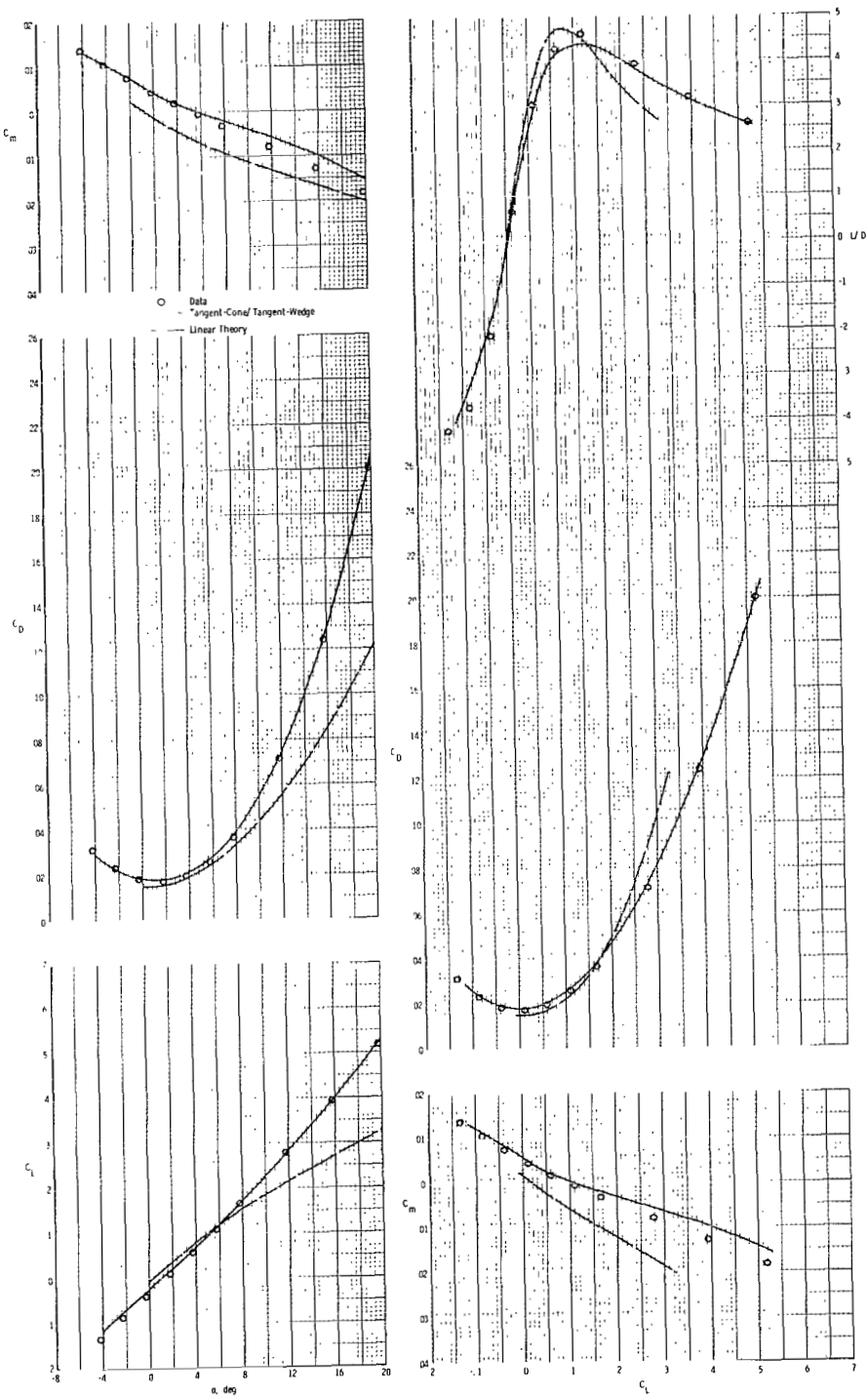
(c)  $M = 4.63.$

Figure 19.- Concluded.



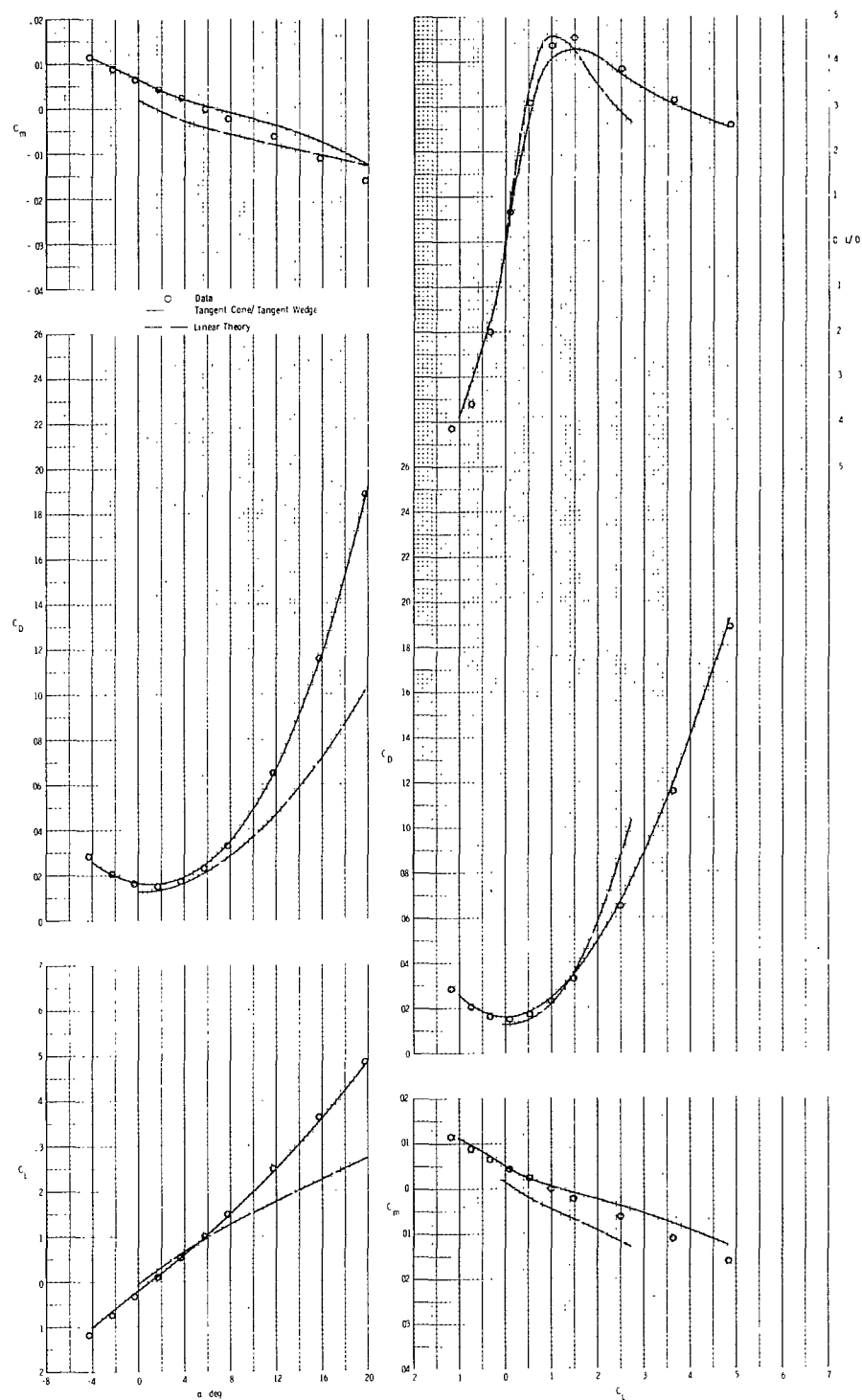
(a)  $M = 2.96.$

**Figure 20.- Comparison of theoretical and experimental longitudinal aerodynamic parameters for BW<sub>1</sub>H<sub>1</sub>V<sub>C</sub>,  $\delta_h = -10^\circ$ .**



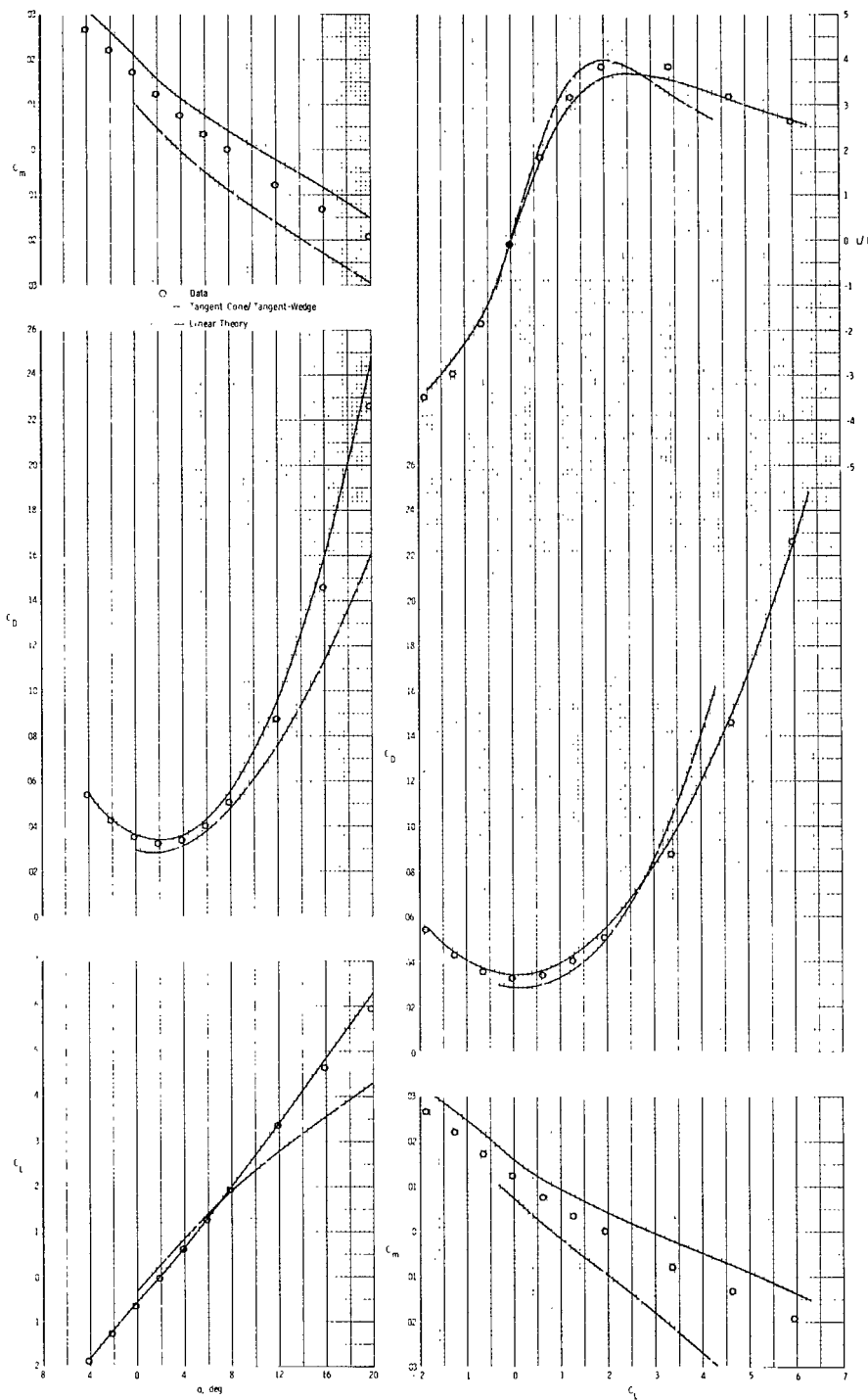
(b)  $M = 3.96.$

Figure 20.- Continued.



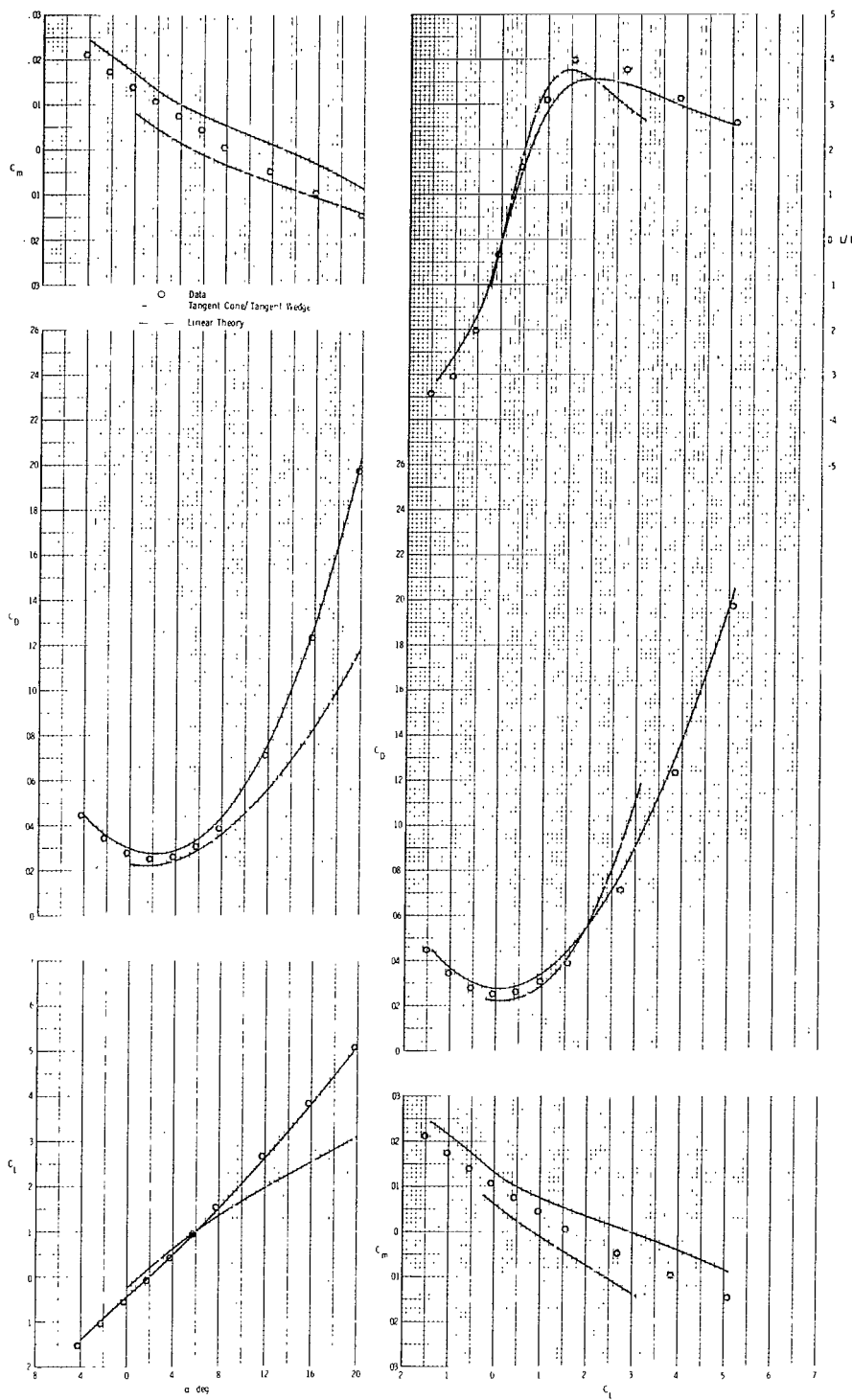
(c)  $M = 4.63.$

Figure 20.- Concluded.



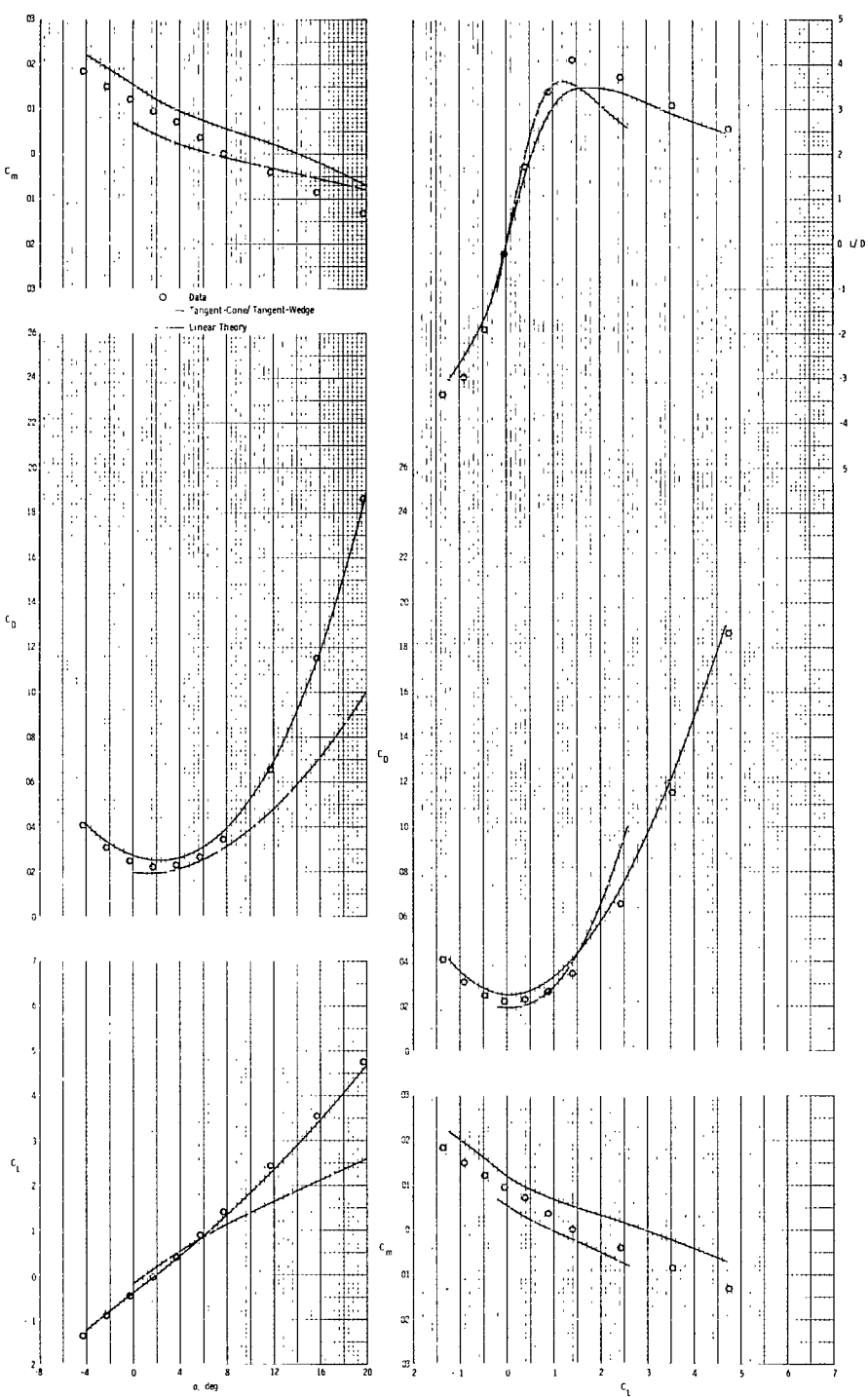
(a)  $M = 2.96$ .

**Figure 21.- Comparison of theoretical and experimental longitudinal aerodynamic parameters for BW<sub>1</sub>H<sub>1</sub>V<sub>C</sub>,  $\delta_h = -20^\circ$ .**



(b)  $M = 3.96.$

Figure 21.- Continued.



(c)  $M = 4.63.$

Figure 21.- Concluded.

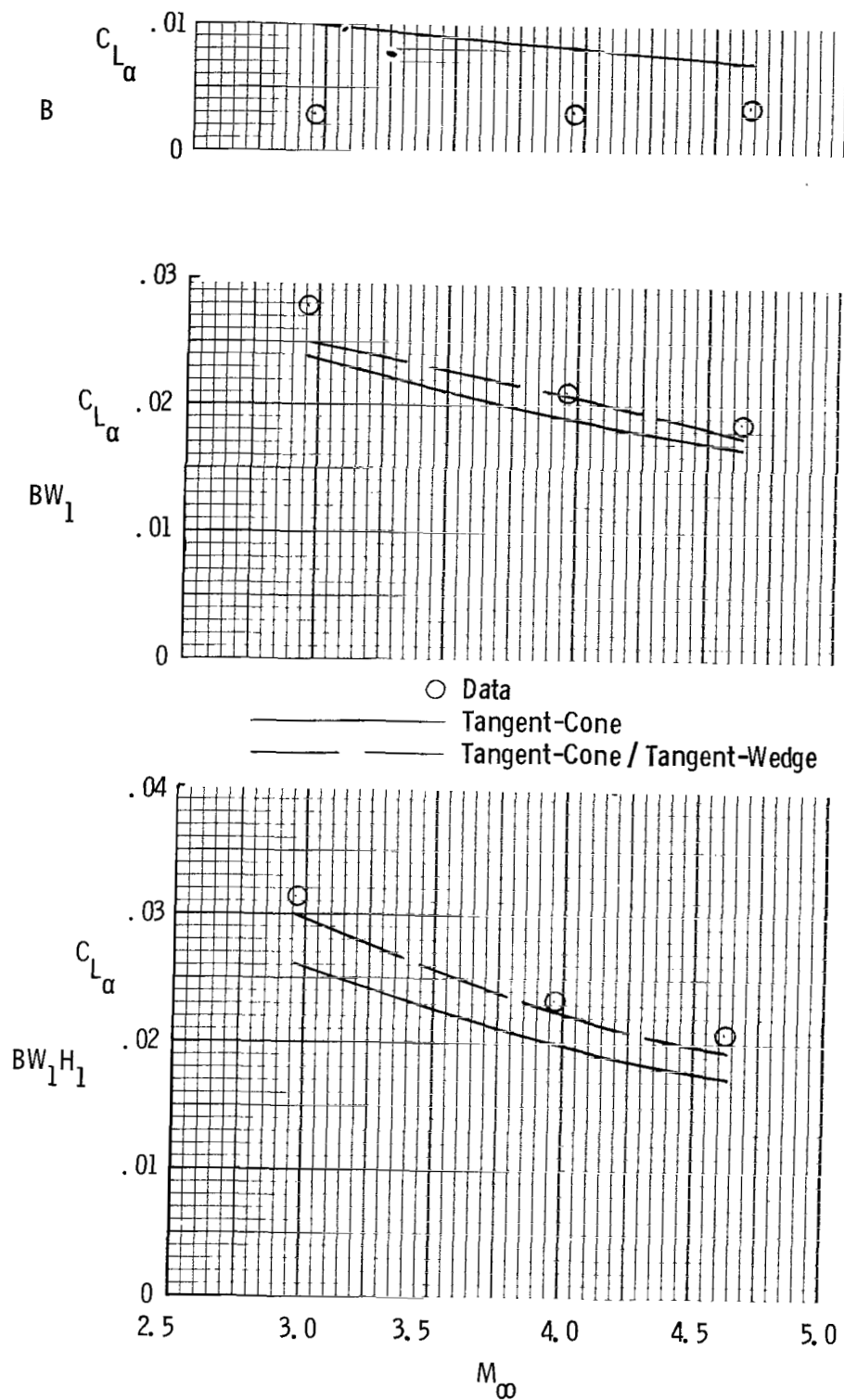
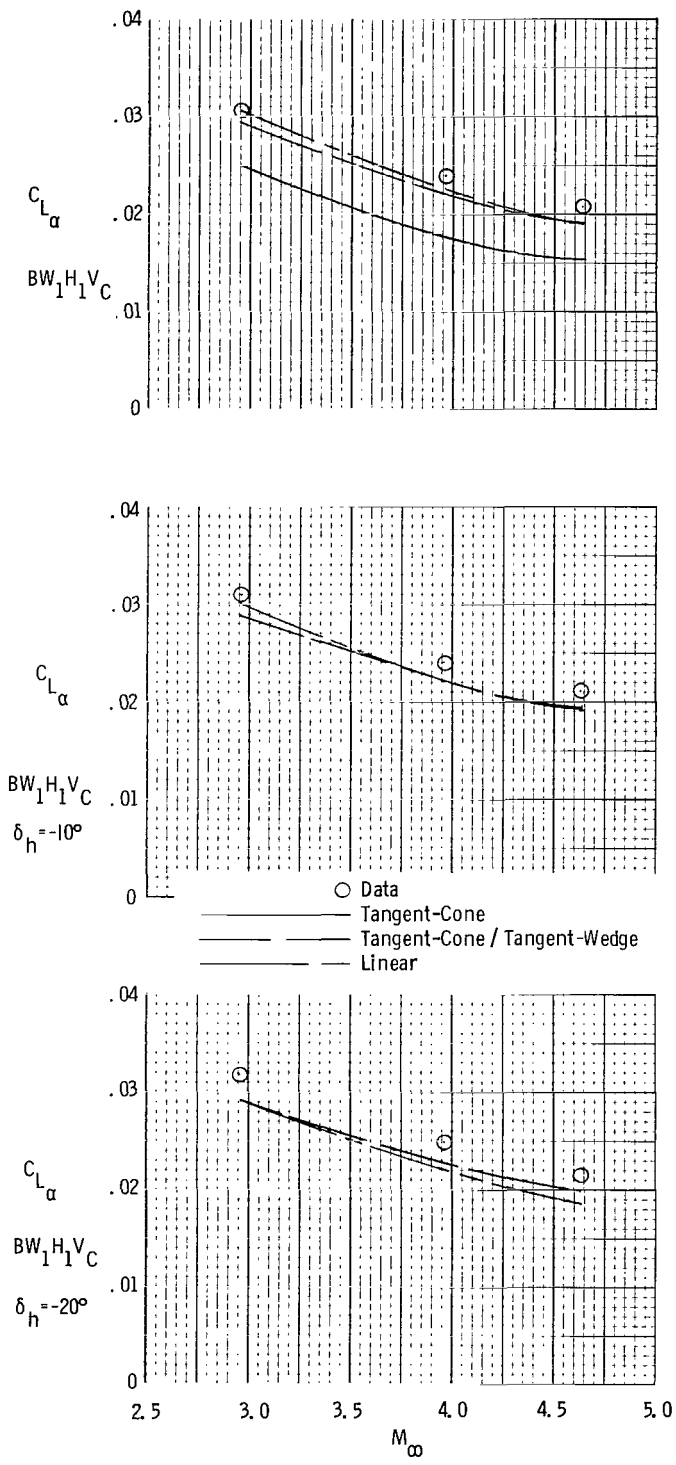


Figure 22.- Comparison of theoretical and experimental lift-curve slope with Mach number.



**Figure 22.- Concluded.**

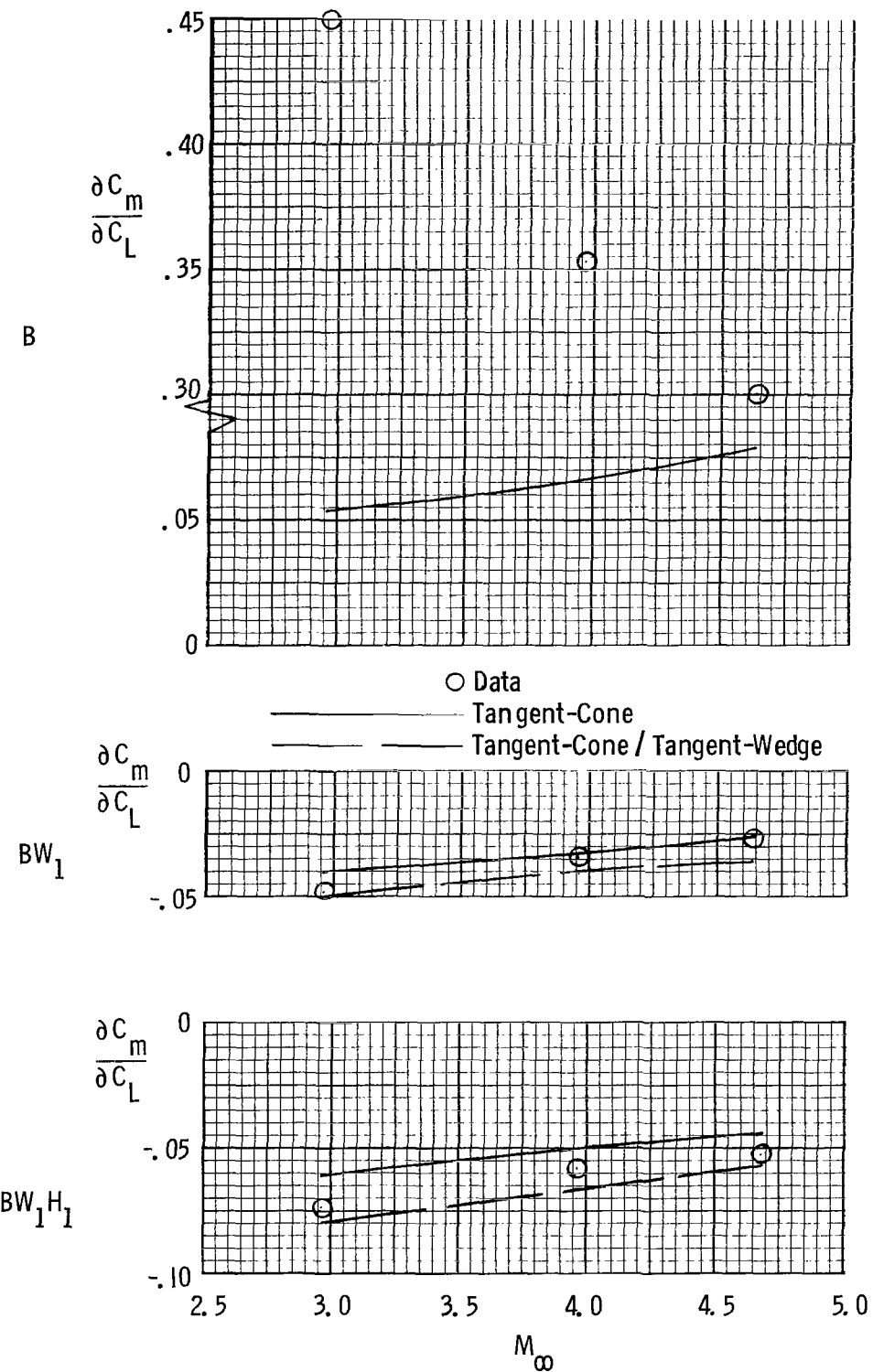


Figure 23.- Comparison of theoretical and experimental static margin with Mach number.

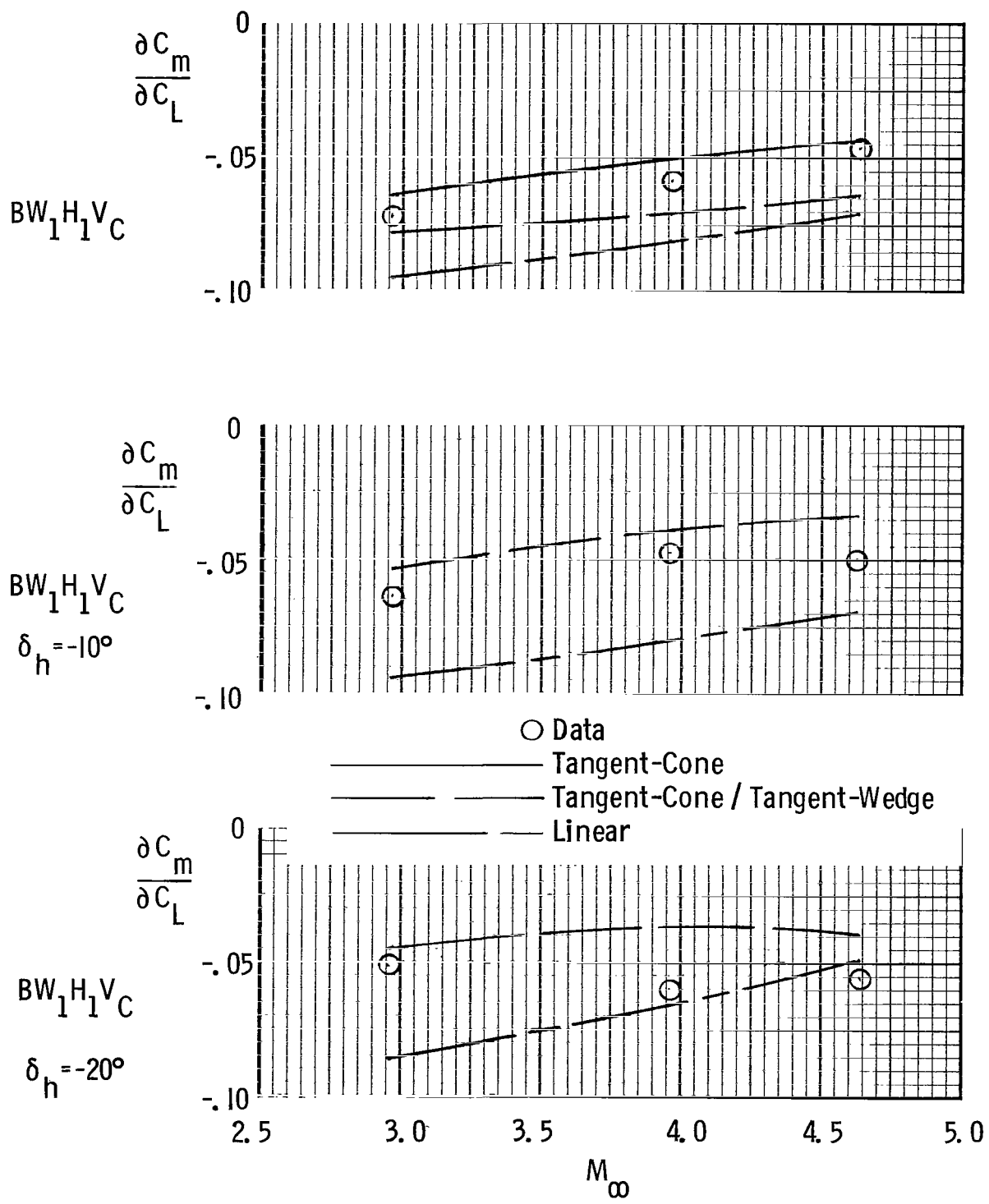


Figure 23.- Concluded.

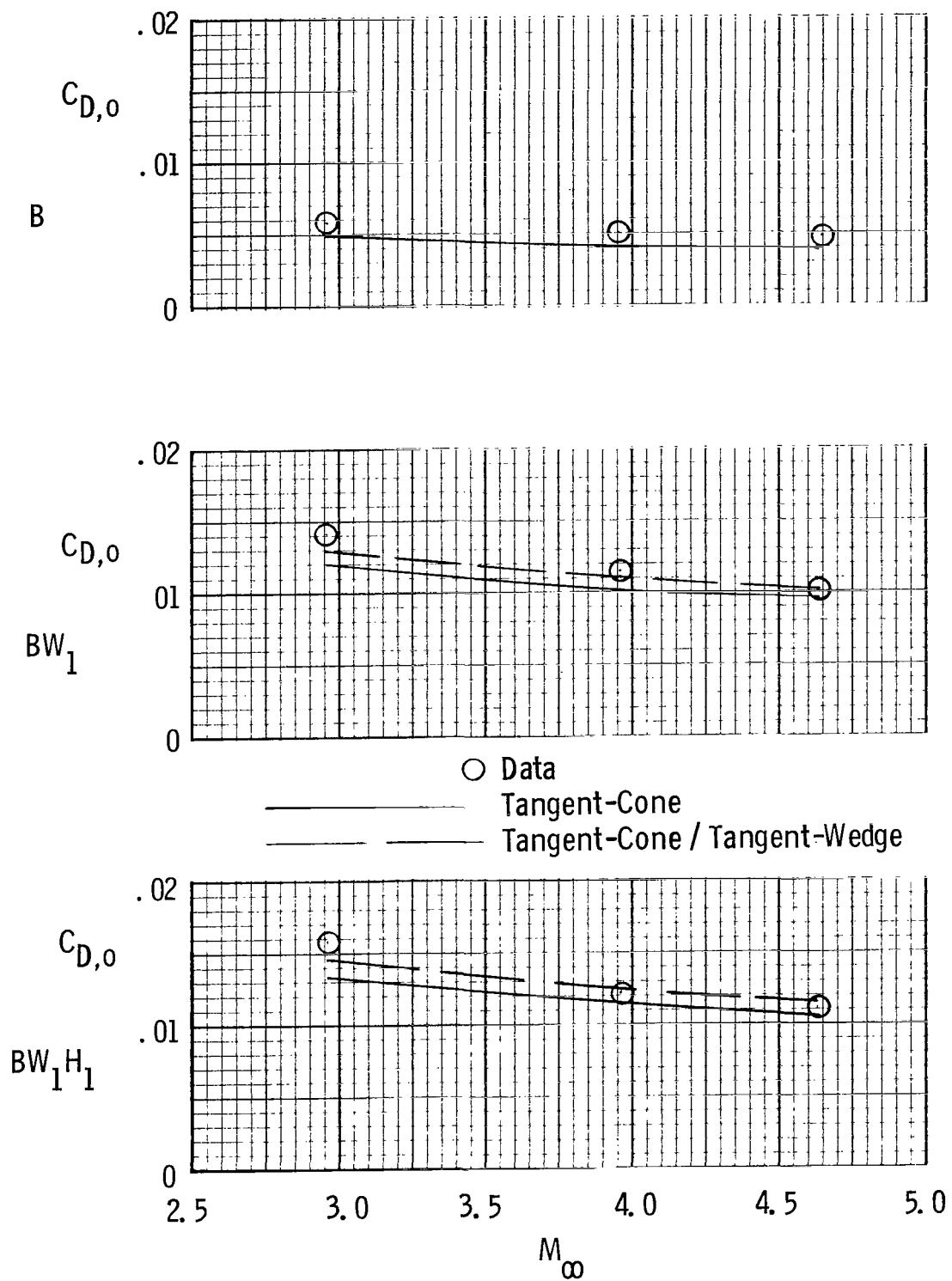


Figure 24.- Comparison of theoretical and experimental zero-lift drag coefficient with Mach number.

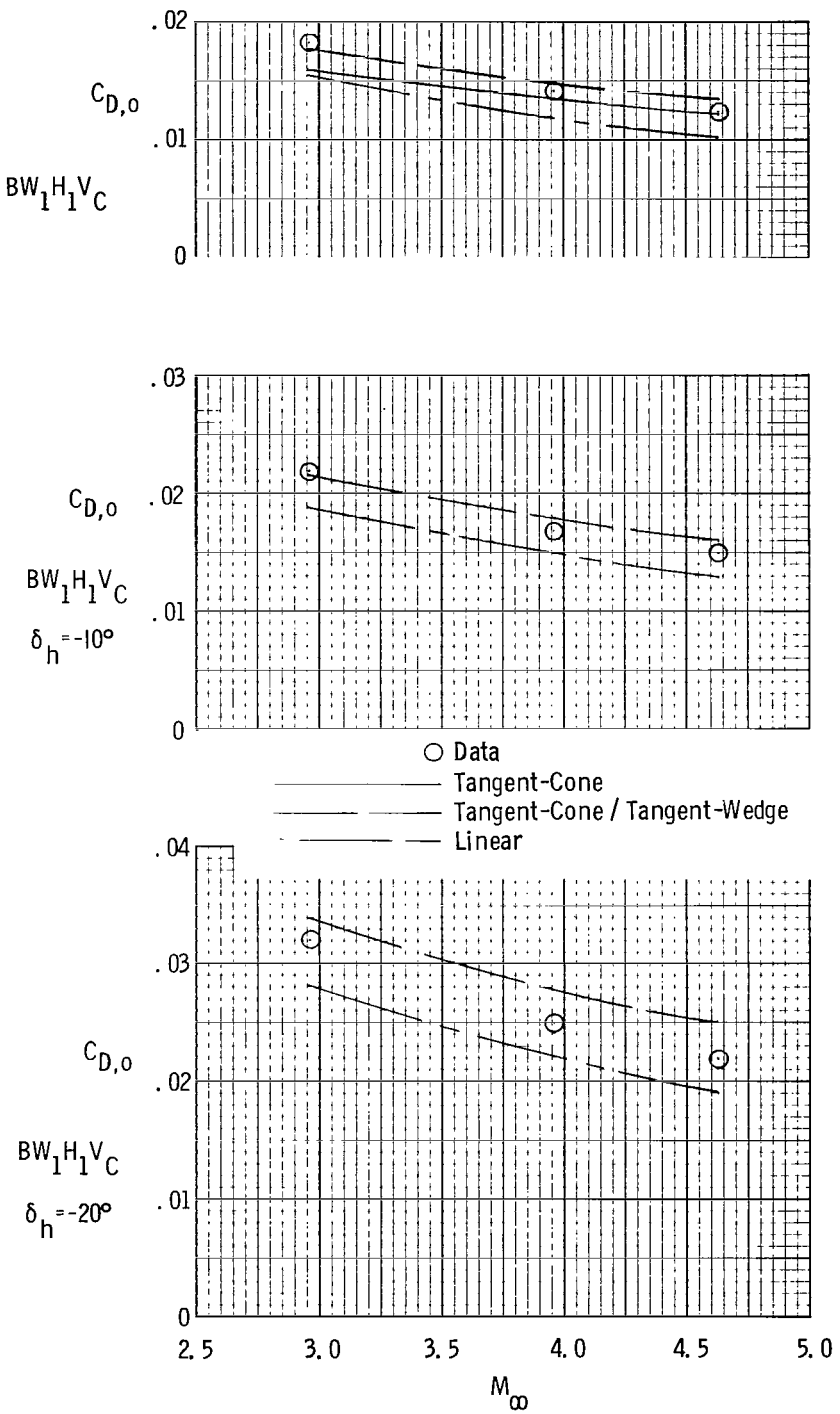


Figure 24.- Concluded.

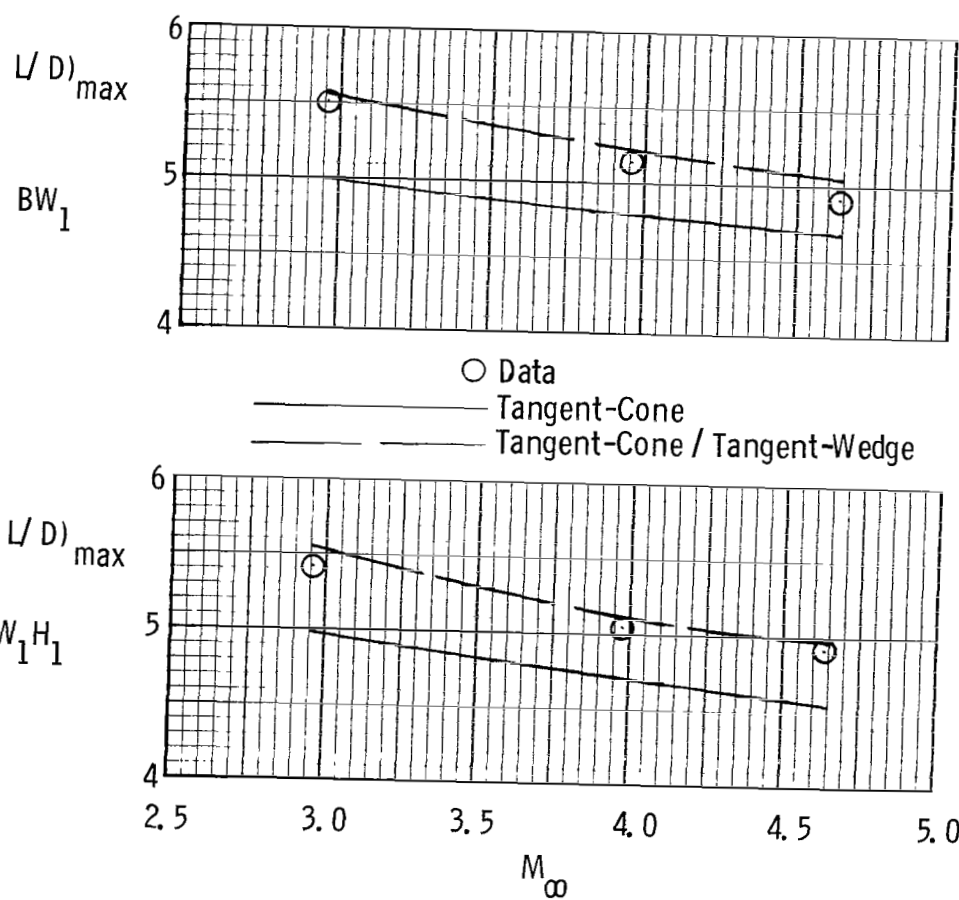
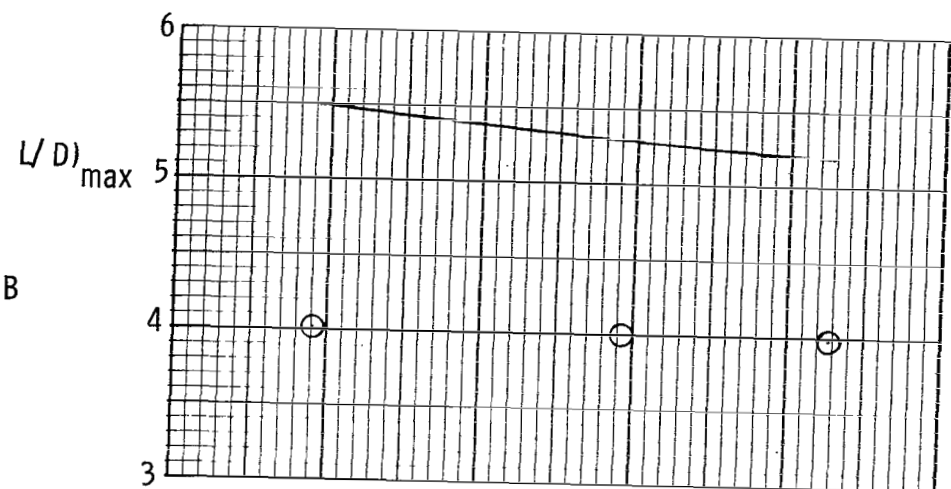


Figure 25.- Comparison of theoretical and experimental maximum lift-drag ratio with Mach number.

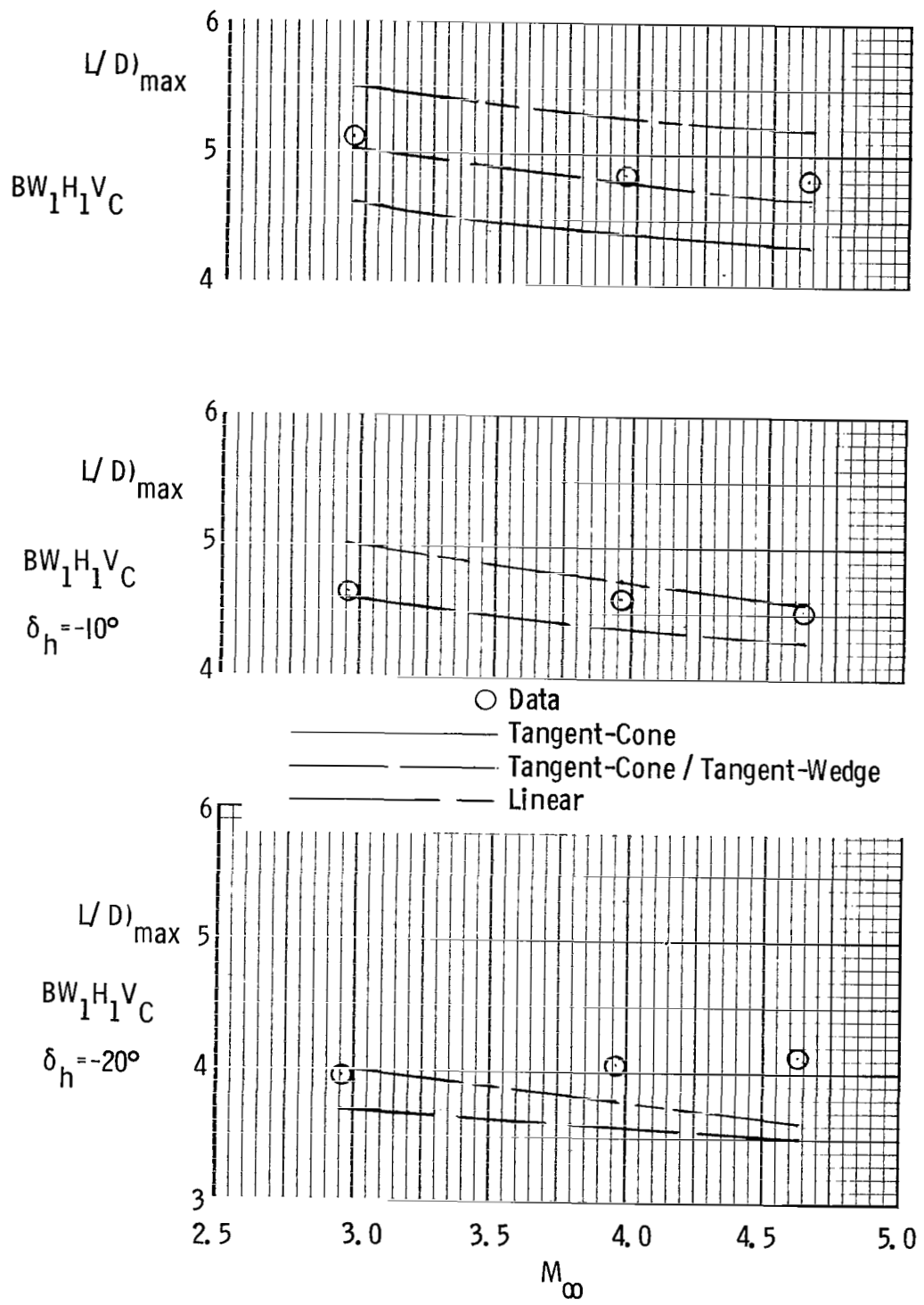
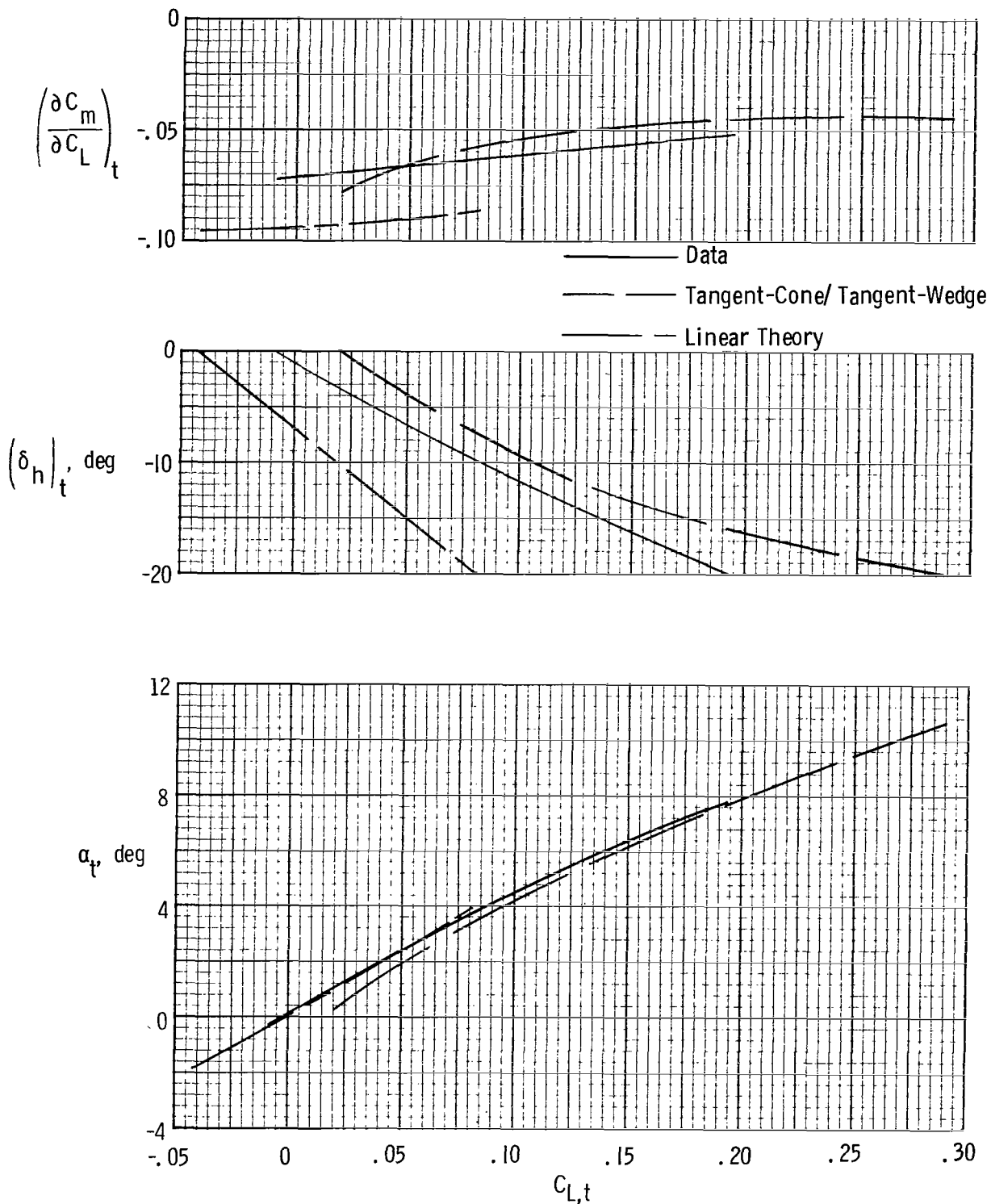
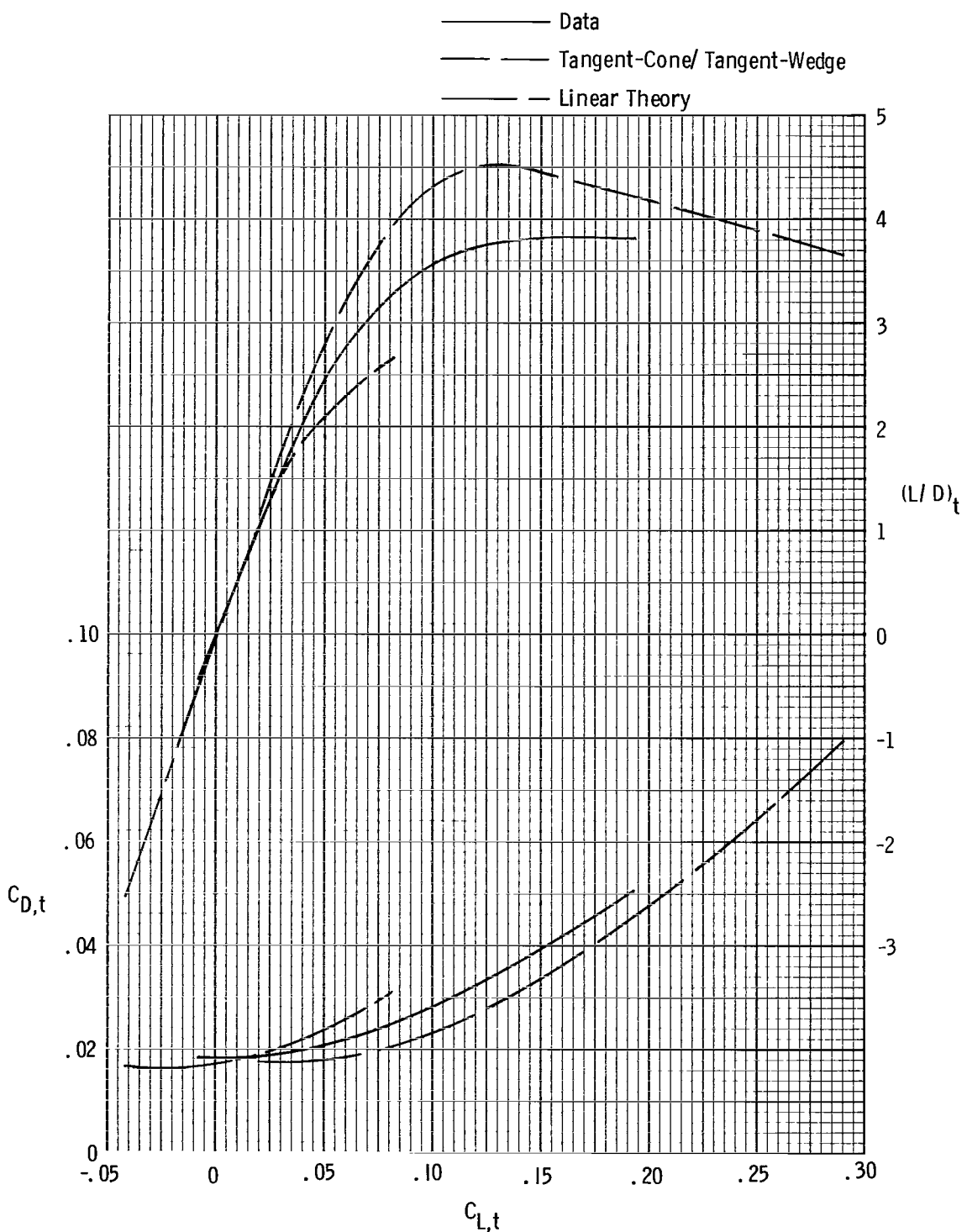


Figure 25.- Concluded.



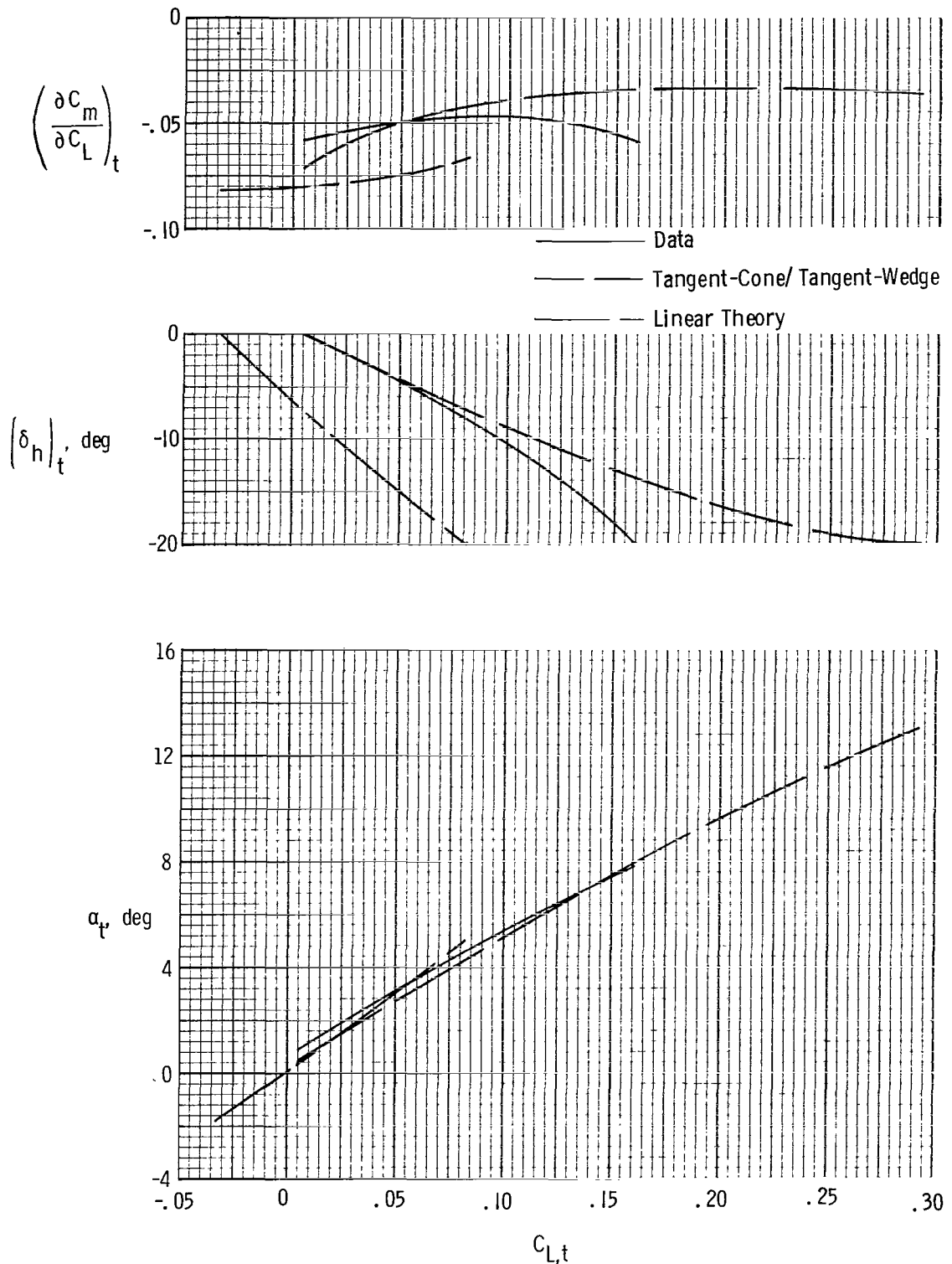
(a)  $M = 2.96$ .

Figure 26.- Comparison of theoretical and experimental trim parameters for BW<sub>1</sub>H<sub>1</sub>V<sub>C</sub> configuration.



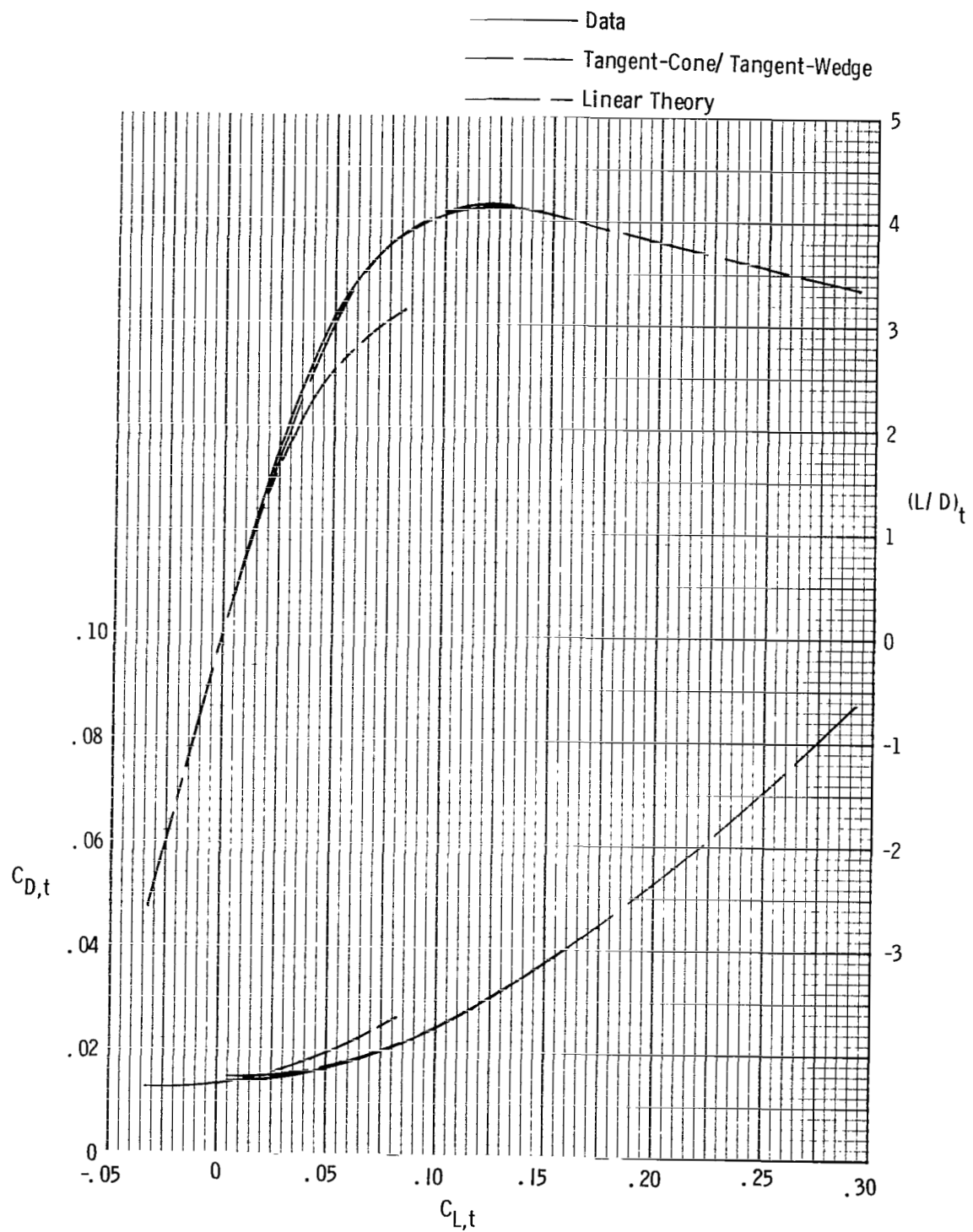
(a) Concluded.

Figure 26.- Continued.



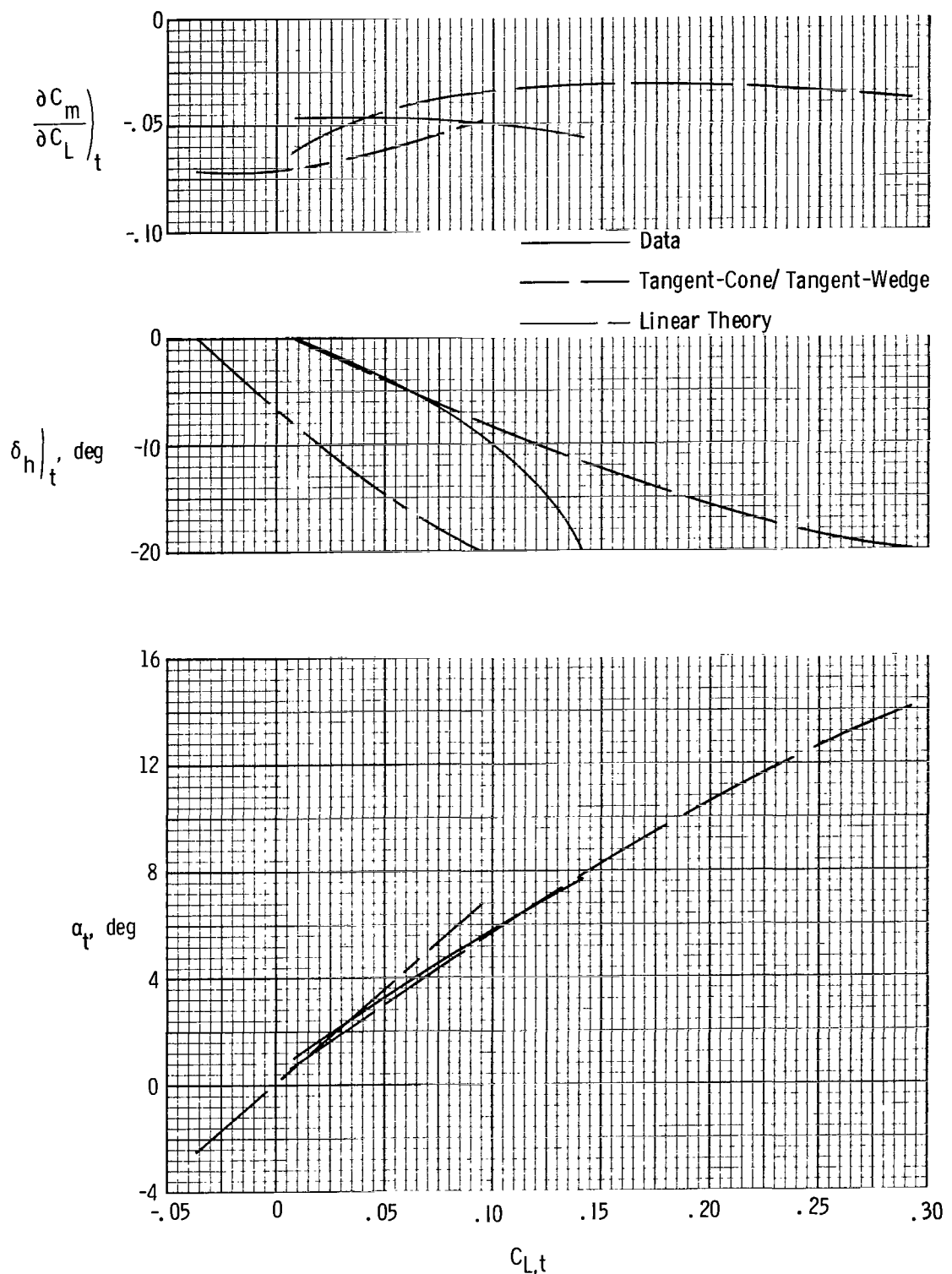
(b)  $M = 3.96.$

Figure 26.- Continued.



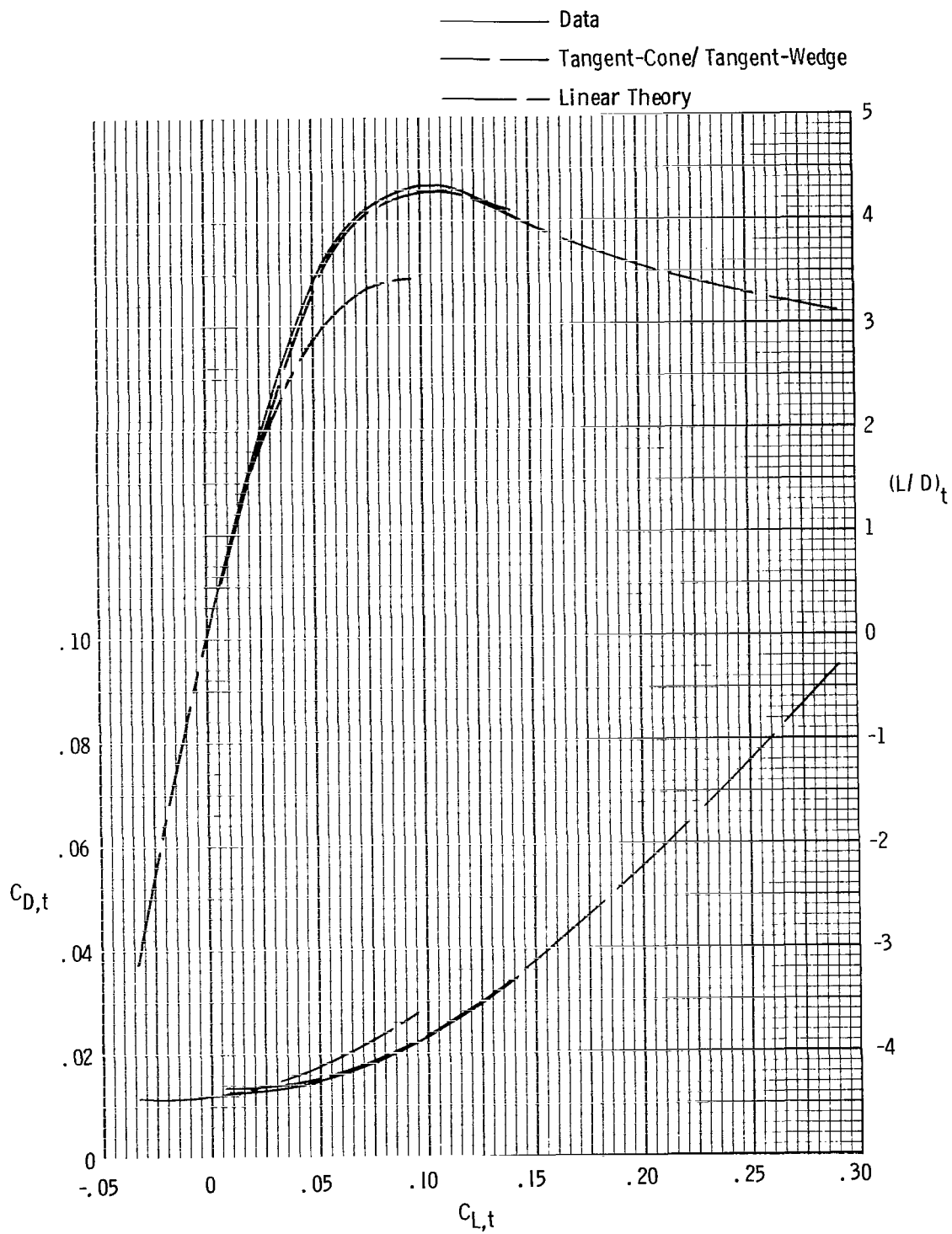
(b) Concluded.

Figure 26.- Continued.



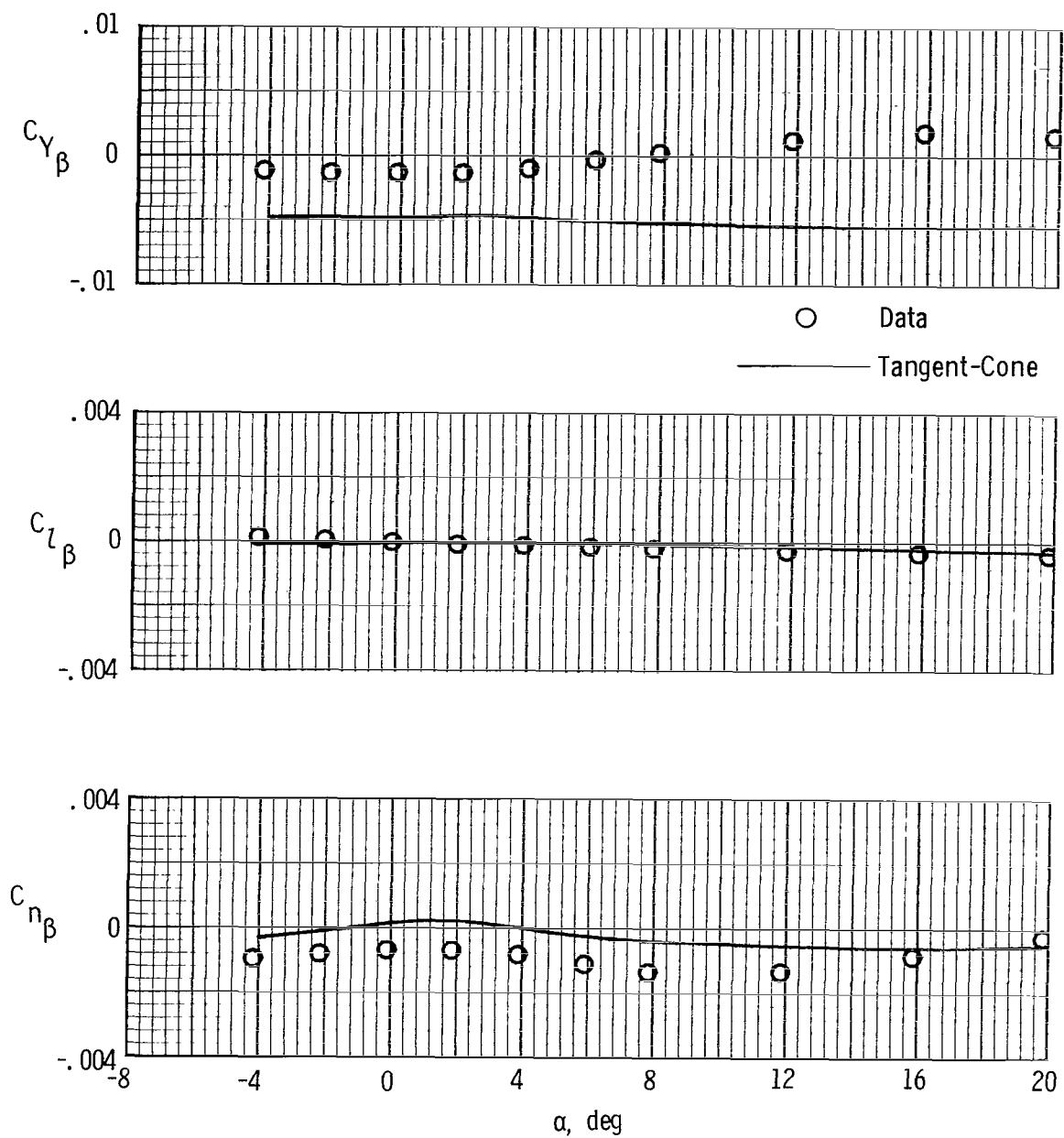
(c)  $M = 4.63.$

Figure 26.- Continued.



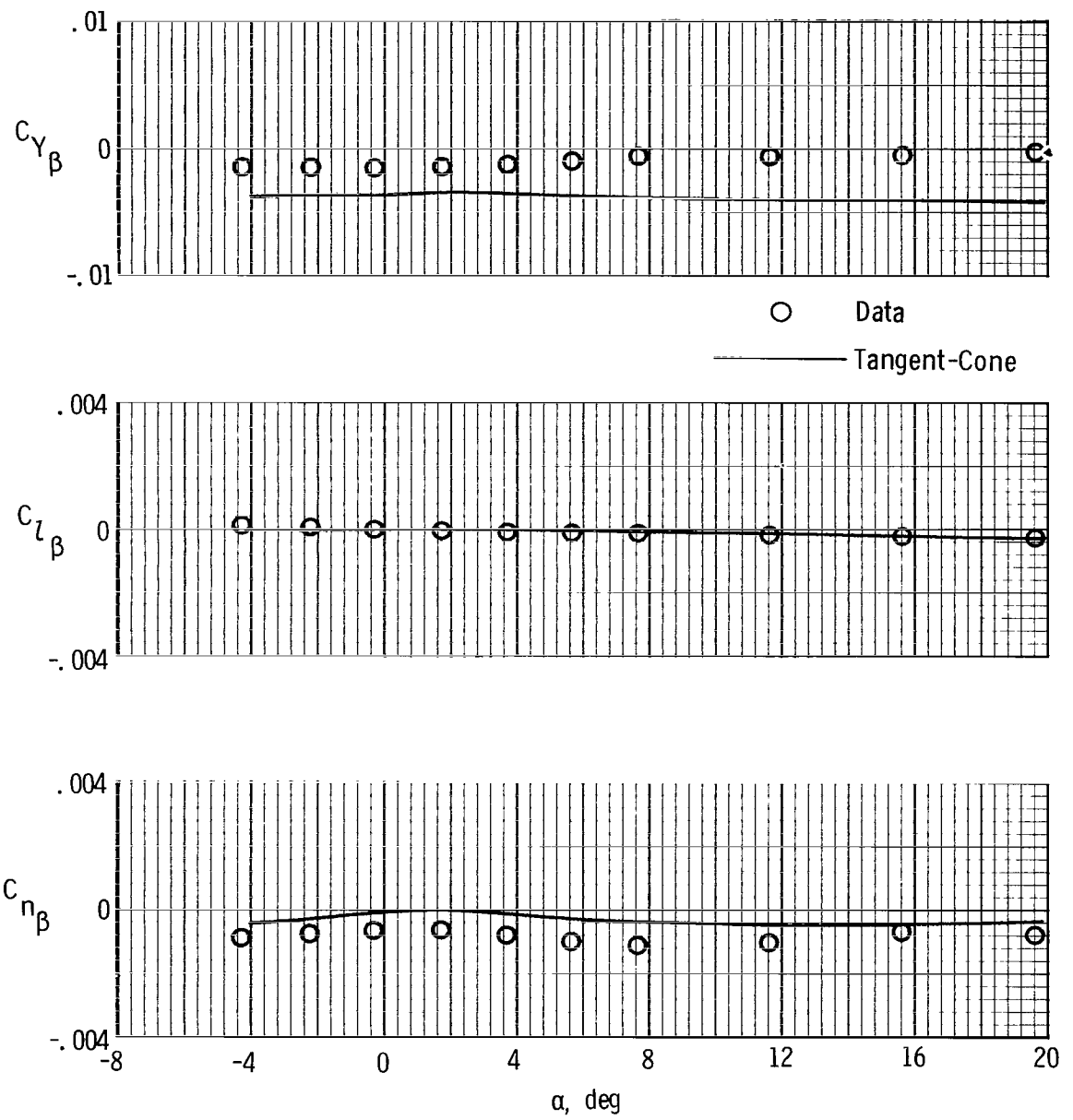
(c) Concluded.

Figure 26.- Concluded.



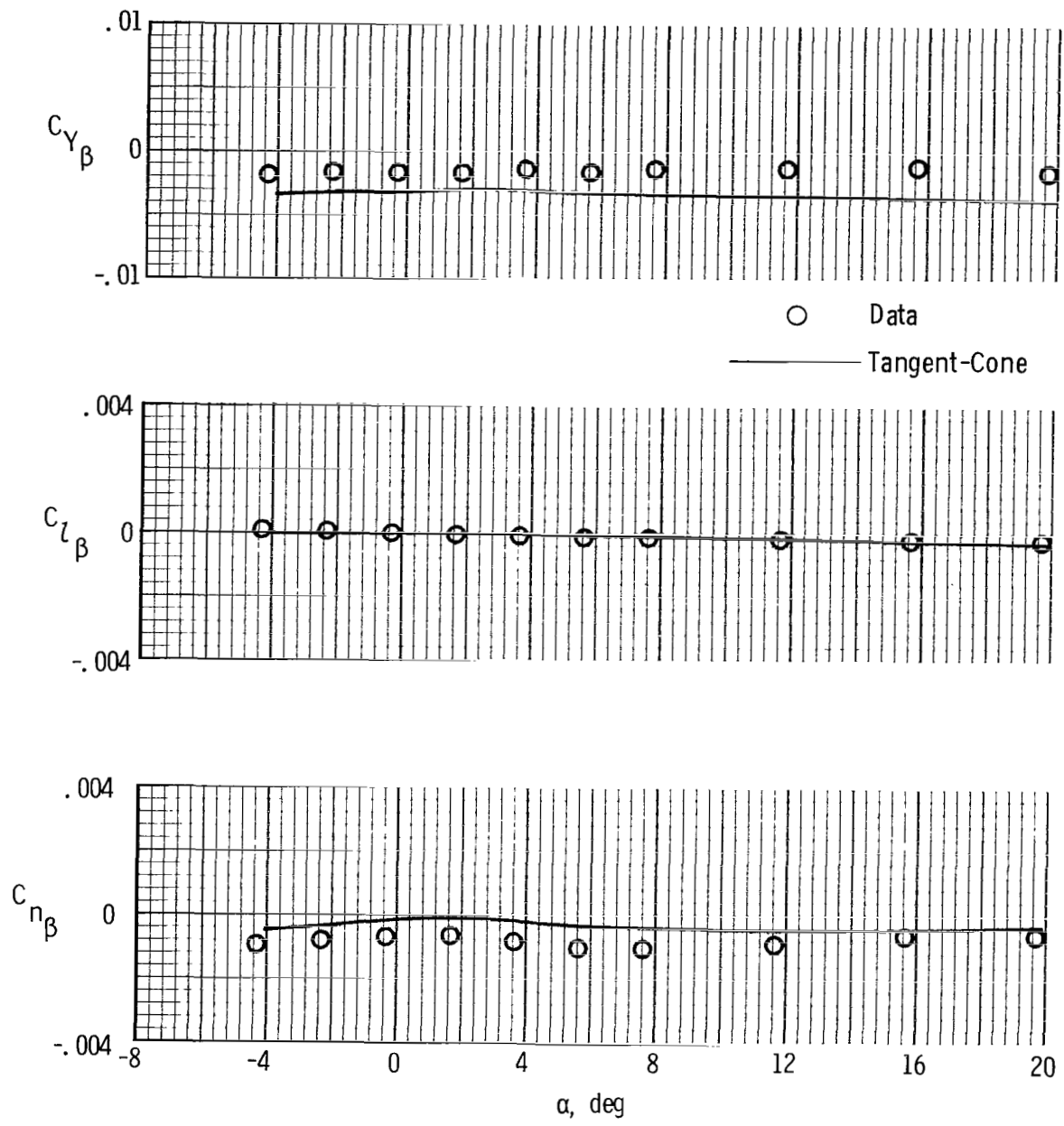
(a)  $M = 2.96$ .

Figure 27.- Comparison of theoretical and experimental lateral-directional aerodynamic parameters for B configuration.



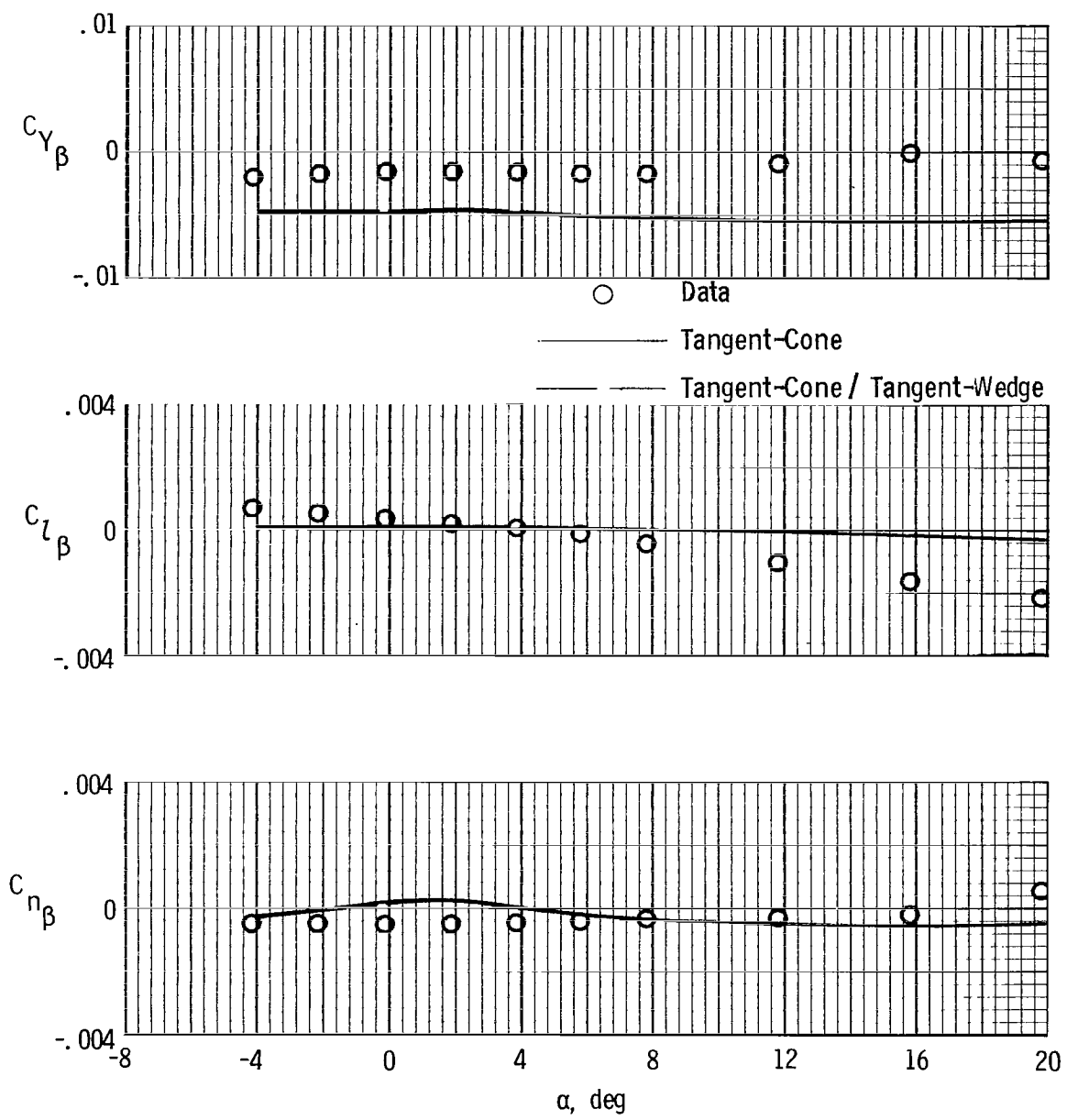
(b)  $M = 3.96.$

Figure 27.- Continued.



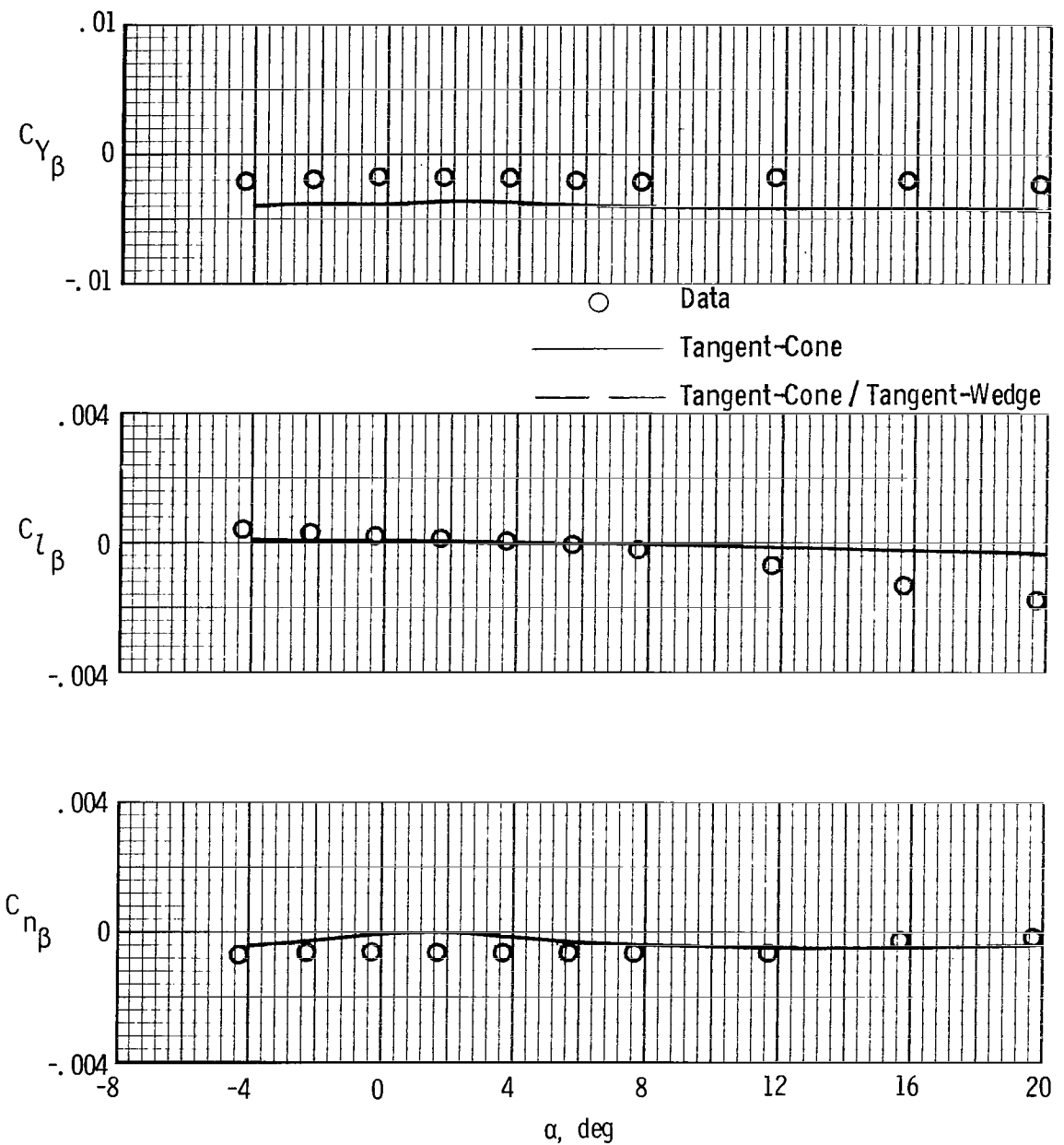
(c)  $M = 4.63.$

Figure 27.- Concluded.



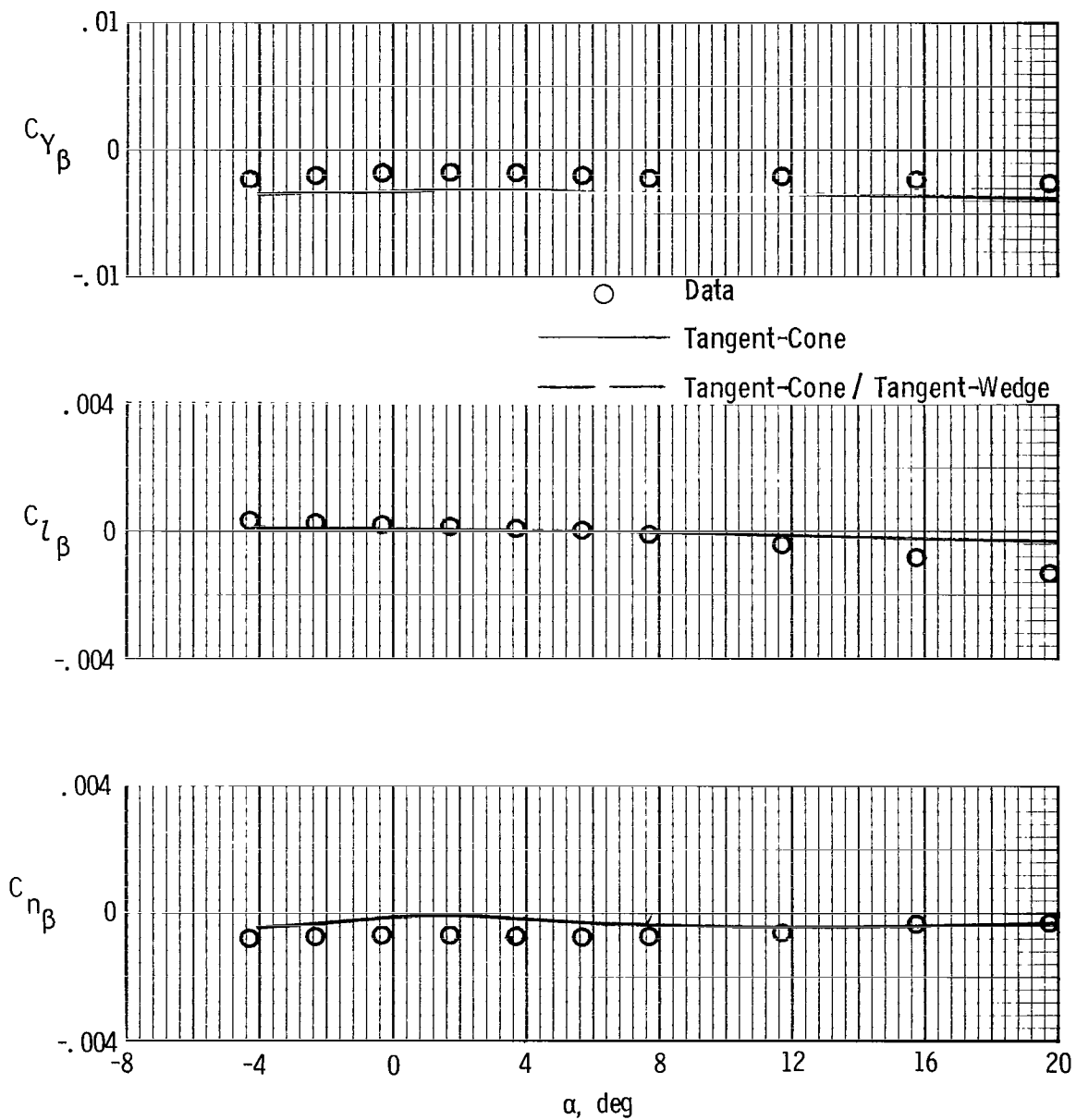
(a)  $M = 2.96$ .

Figure 28.- Comparison of theoretical and experimental lateral-directional aerodynamic parameters for BW<sub>1</sub> configuration.



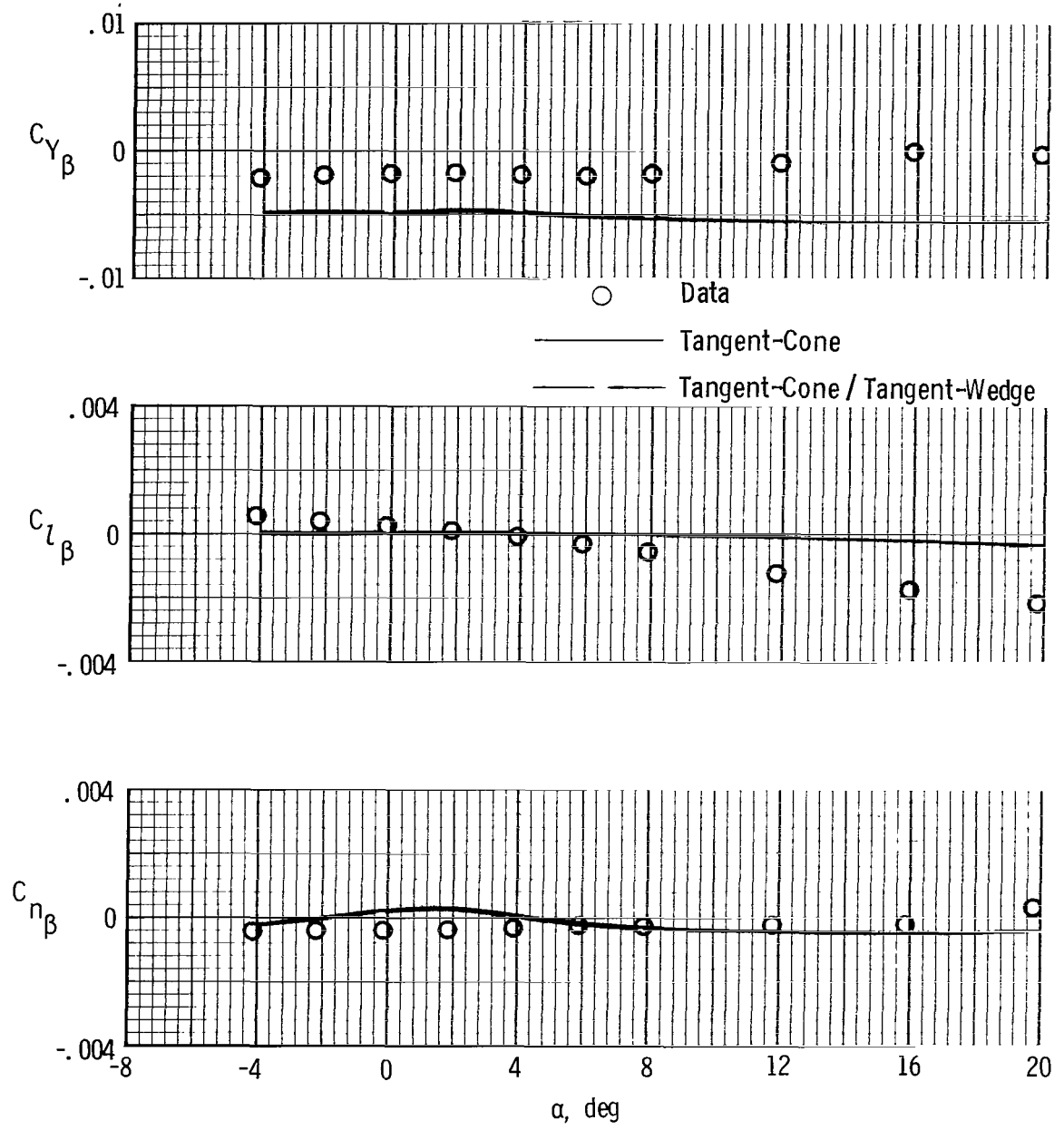
(b)  $M = 3.96$ .

Figure 28.- Continued.



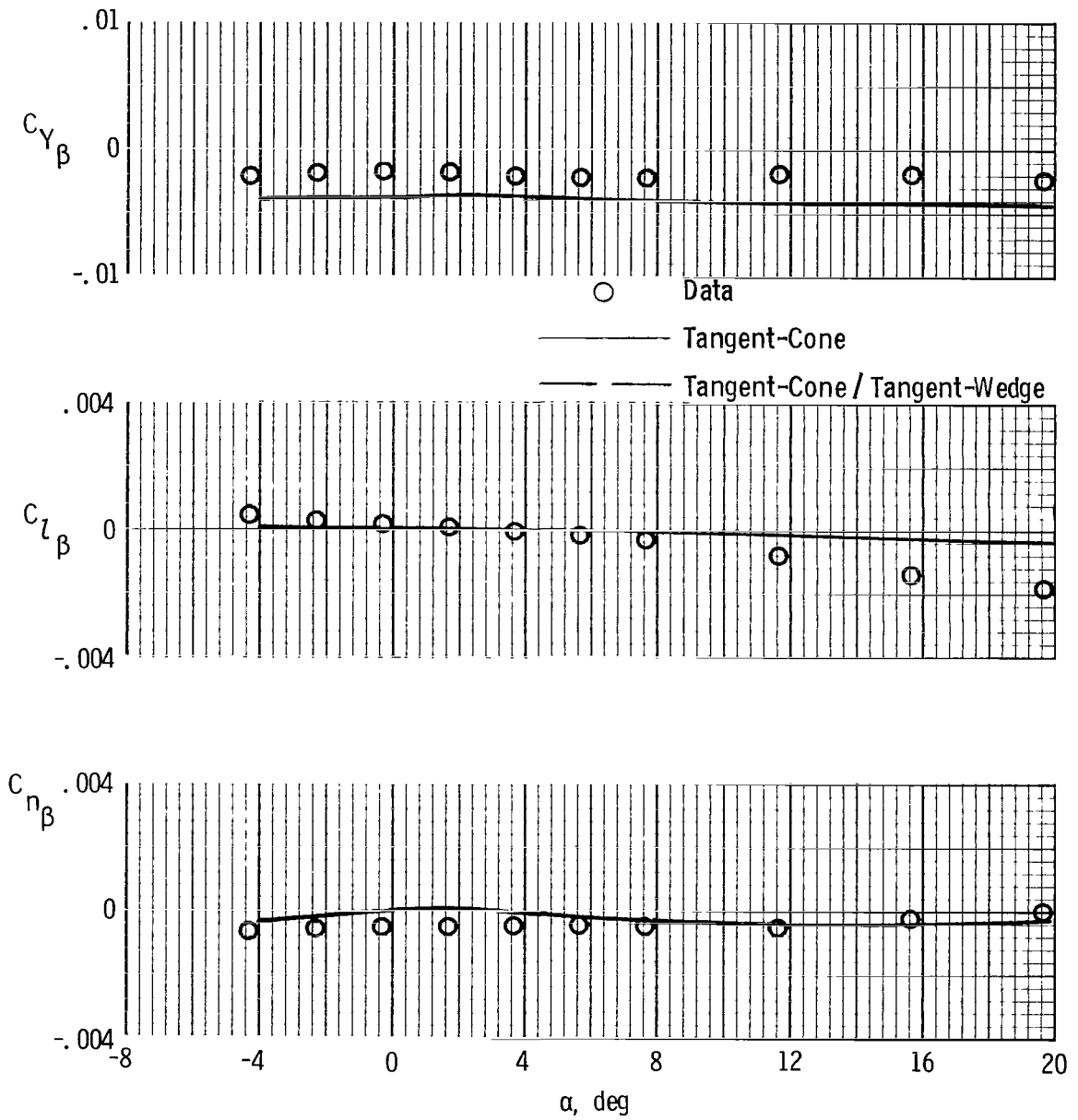
(c)  $M = 4.63$ .

Figure 28.- Concluded.



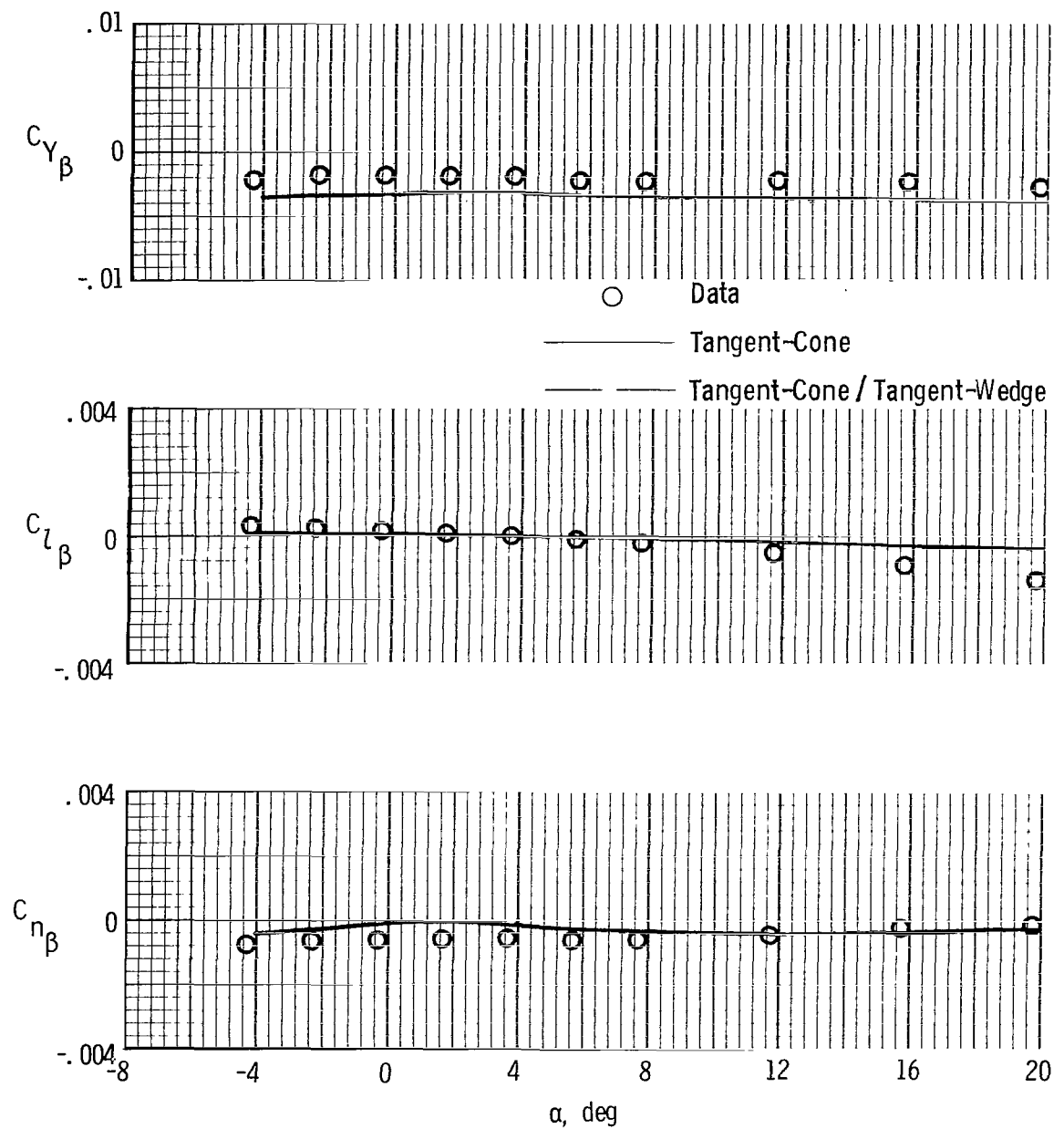
(a)  $M = 2.96$ .

Figure 29.- Comparison of theoretical and experimental lateral-directional aerodynamic parameters for BW<sub>1</sub>H<sub>1</sub> configuration.



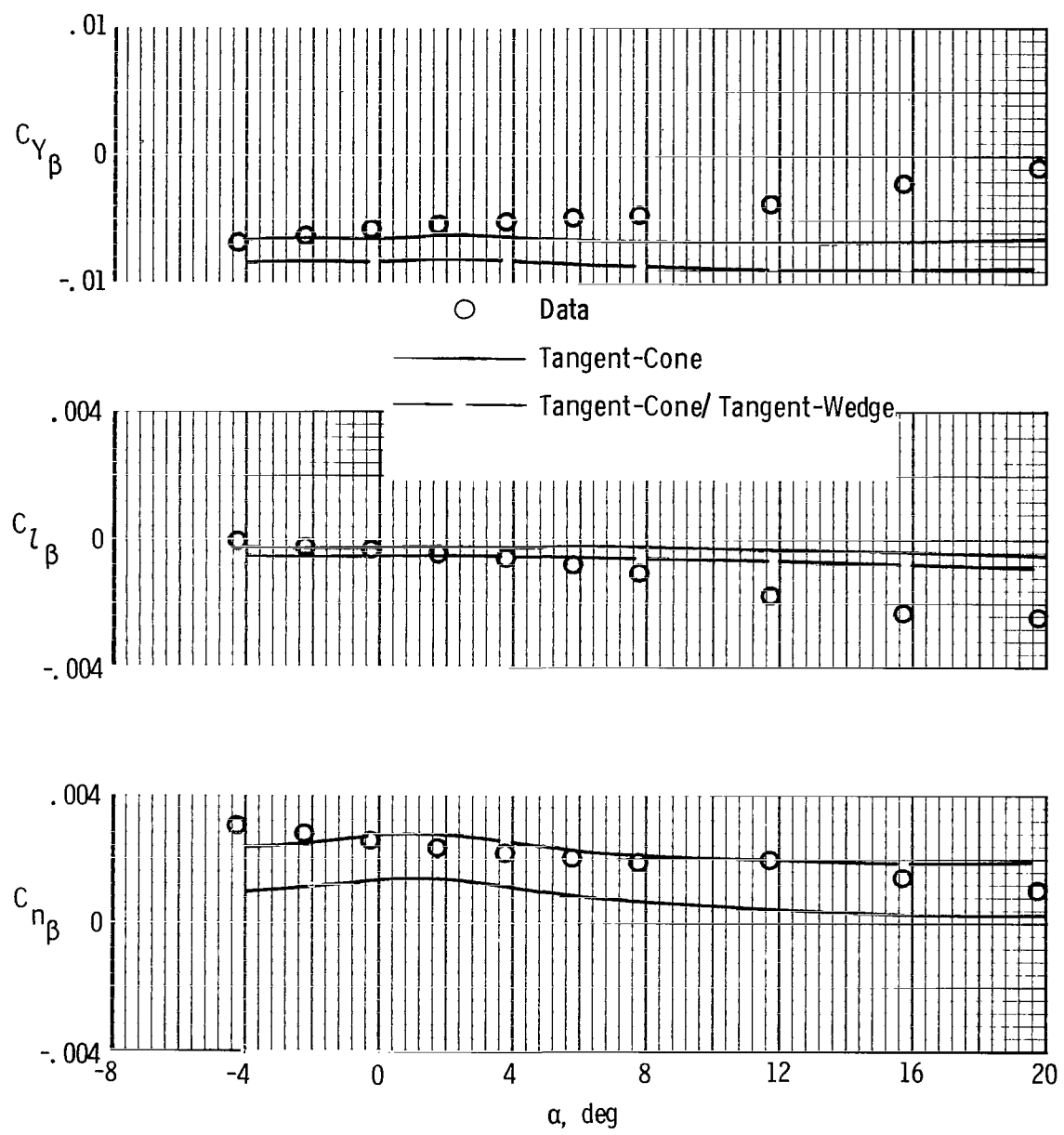
(b)  $M = 3.96.$

Figure 29.- Continued.



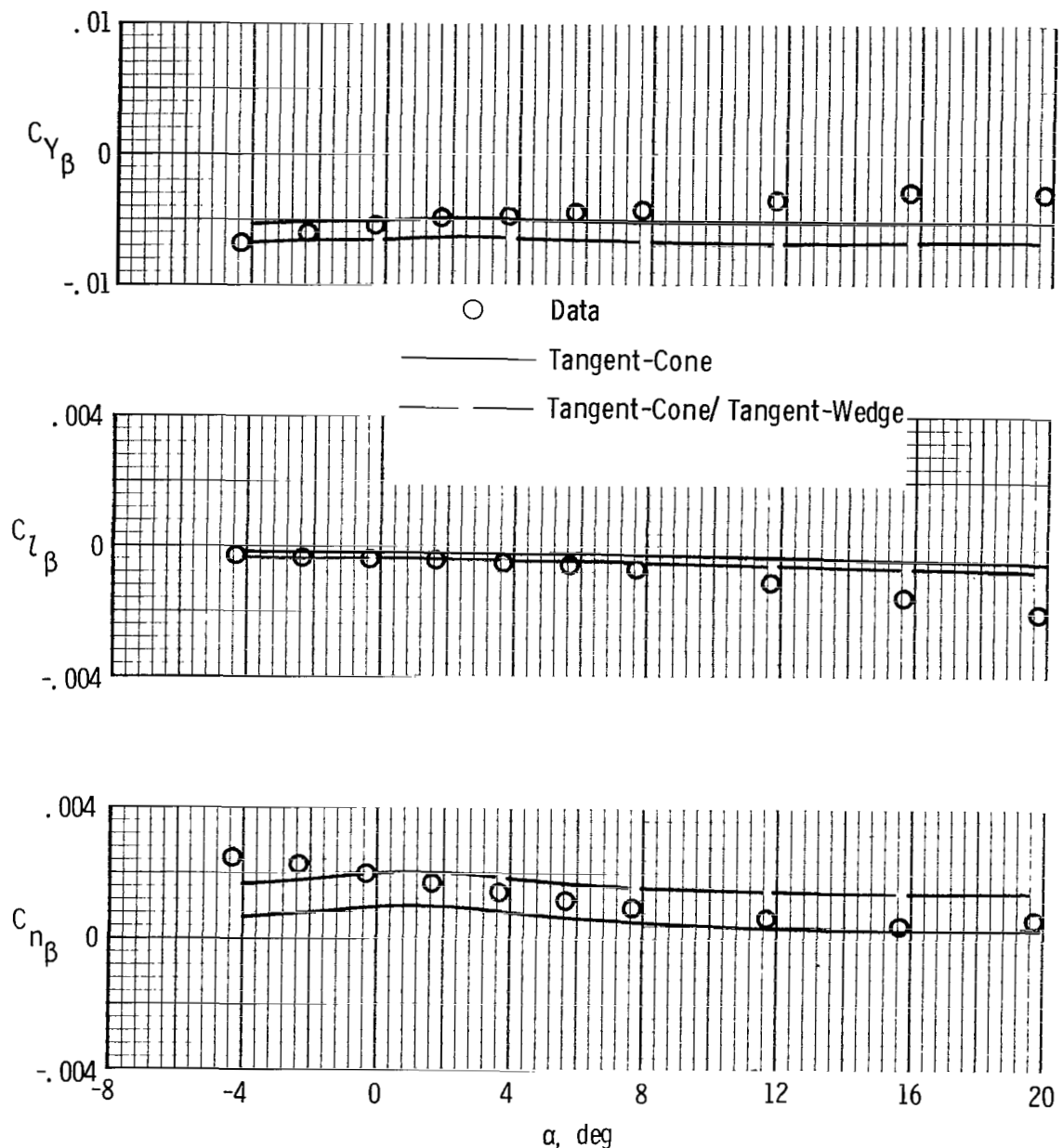
(c)  $M = 4.63$ .

**Figure 29.- Concluded.**



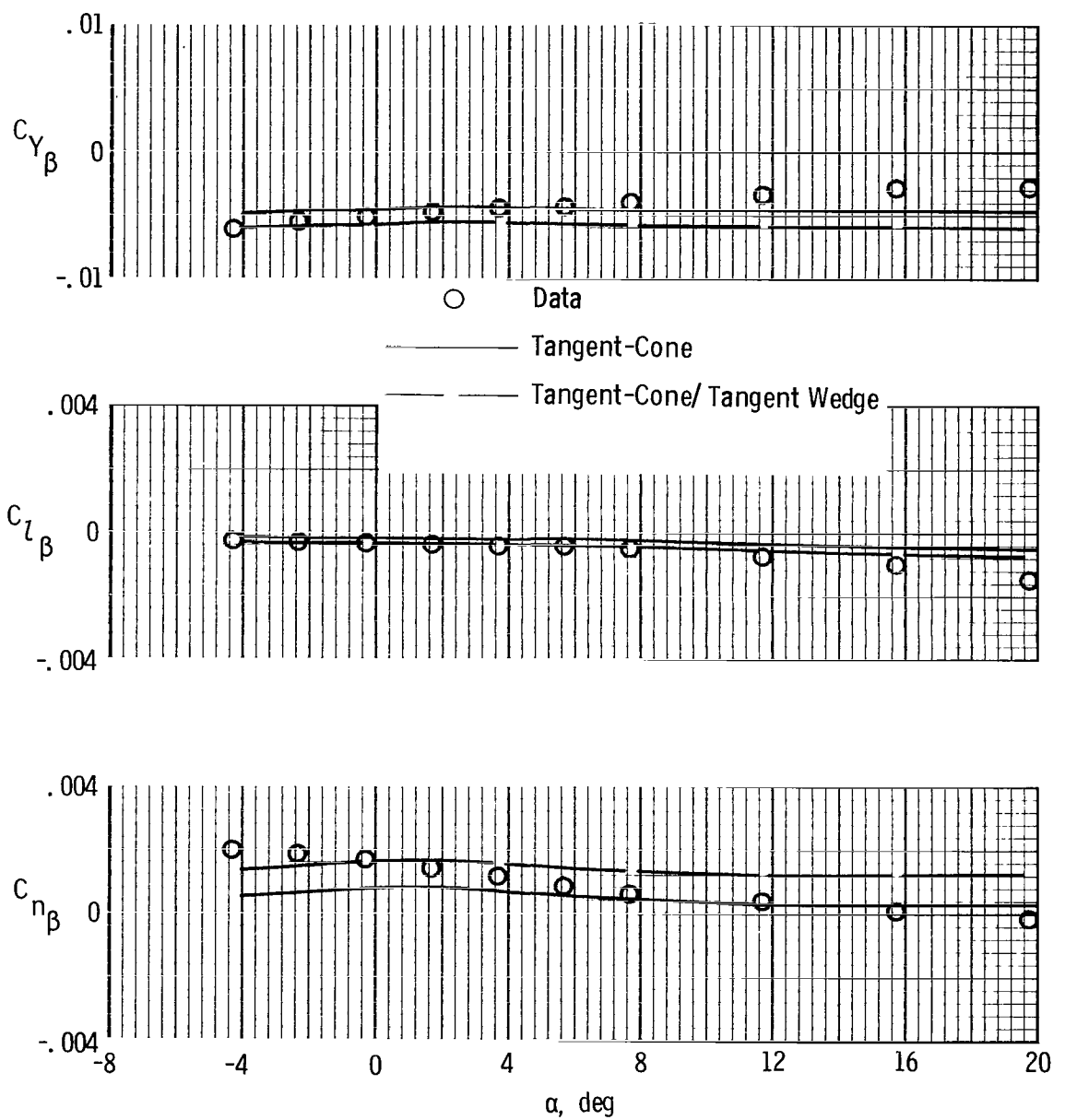
(a)  $M = 2.96$ .

Figure 30.- Comparison of theoretical and experimental lateral-directional aerodynamic parameters for BW<sub>1</sub>H<sub>1</sub>V<sub>C</sub> configuration.



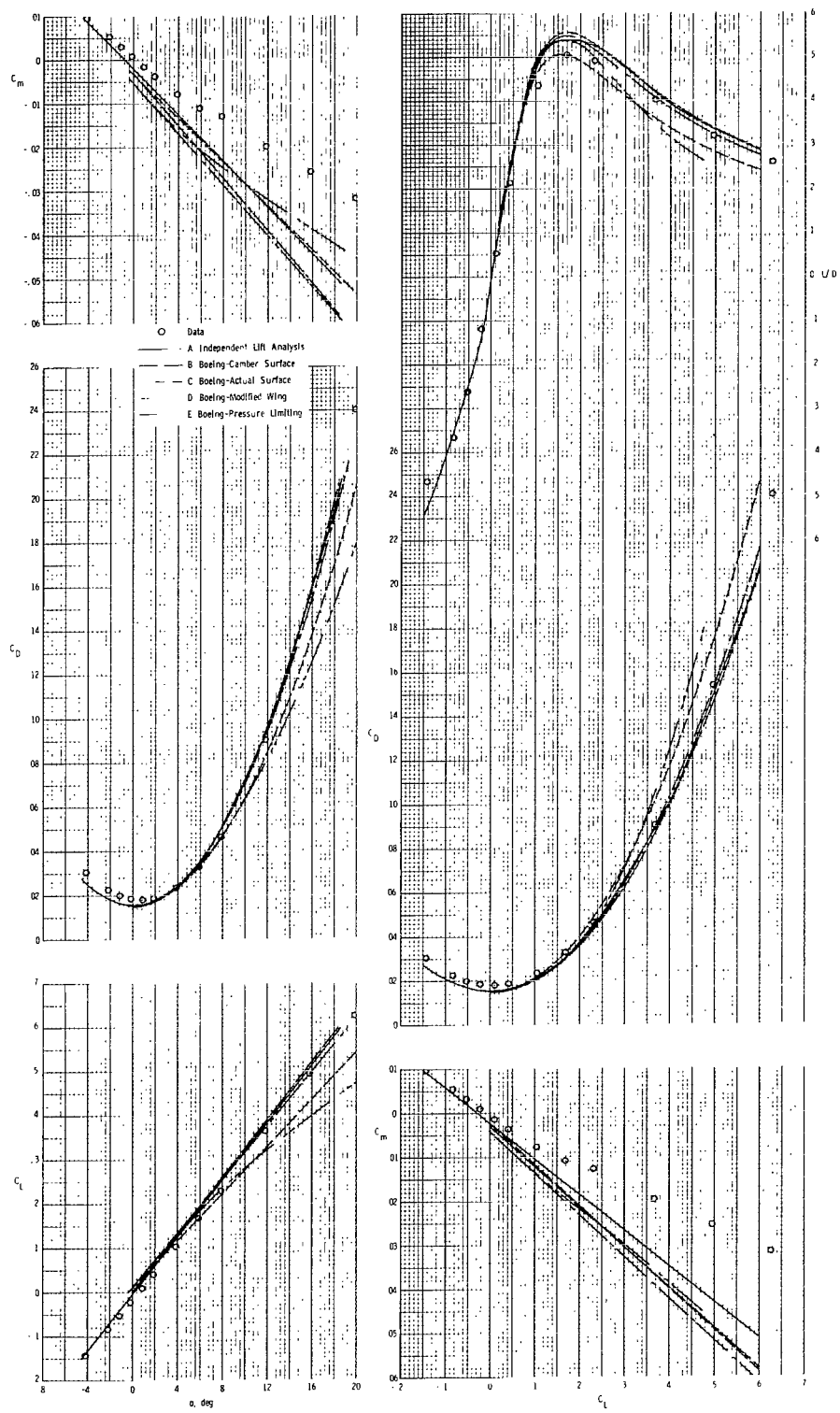
(b)  $M = 3.96.$

Figure 30.- Continued.



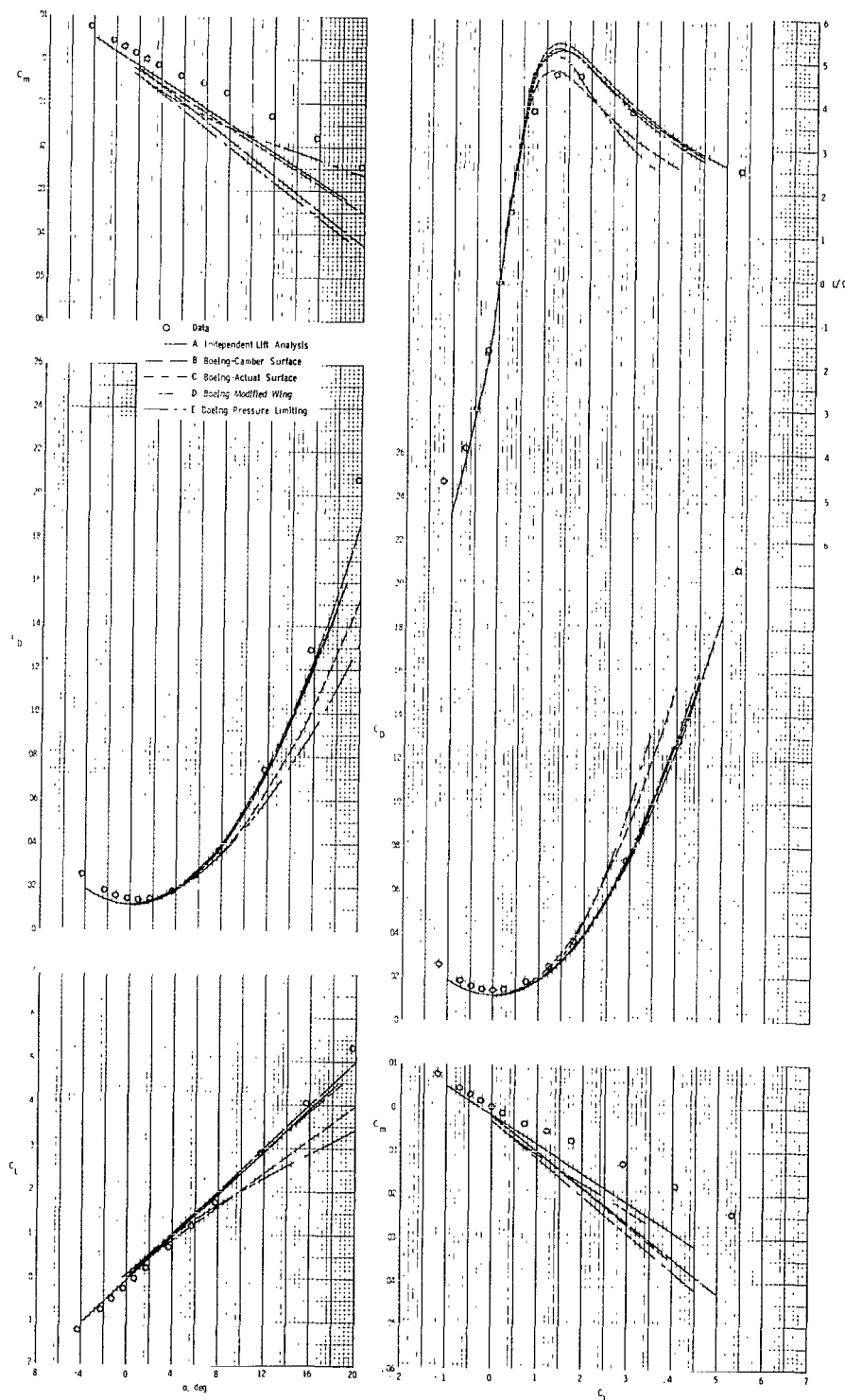
(c)  $M = 4.63.$

Figure 30.- Concluded.



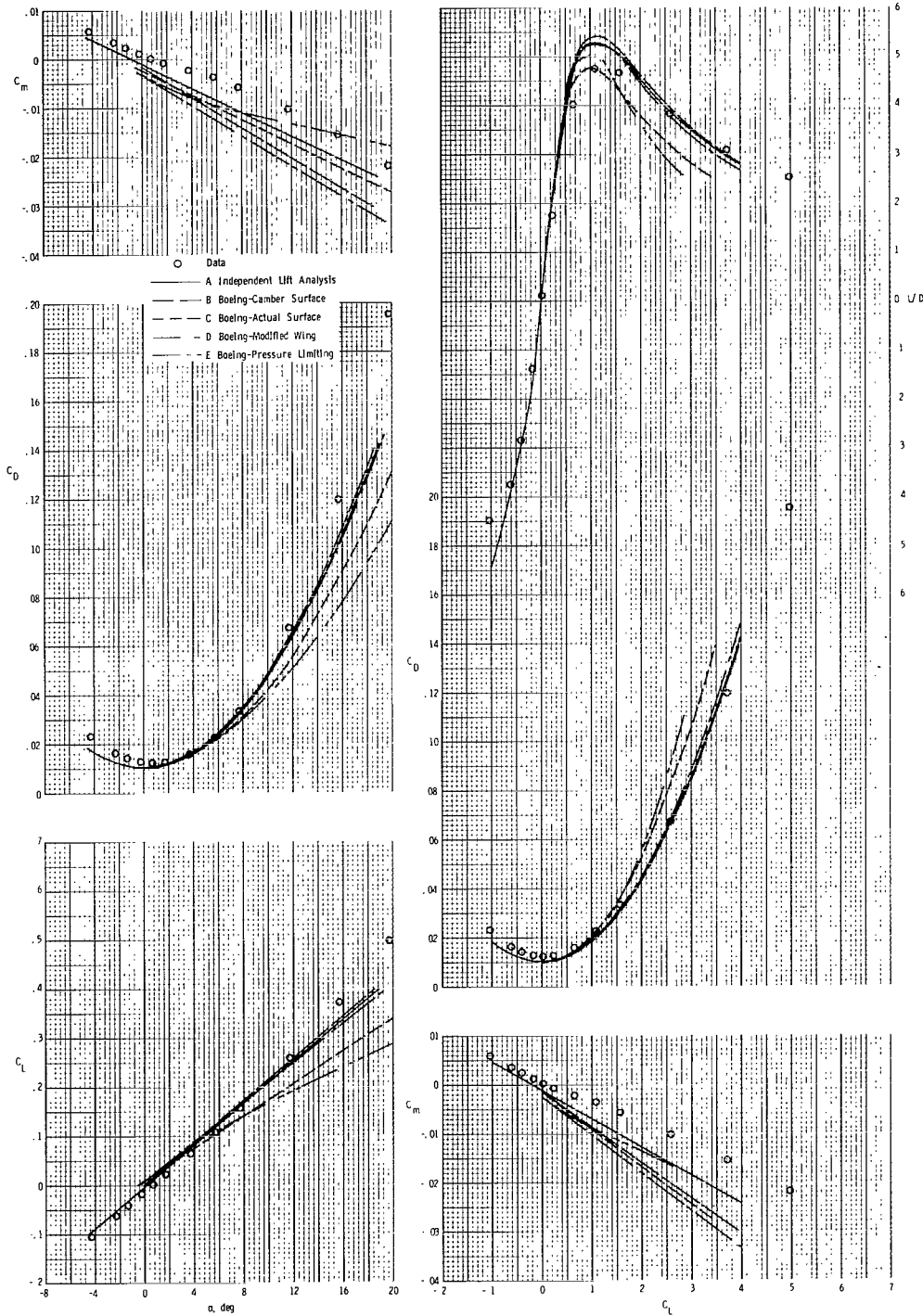
(a)  $M = 2.96$ .

Figure 31.- Evaluation of supersonic linearized theory for BW<sub>1</sub>H<sub>1</sub>V<sub>C</sub> configuration.



(b)  $M = 3.96.$

Figure 31.- Continued.



(c)  $M = 4.63.$

Figure 31.- Concluded.

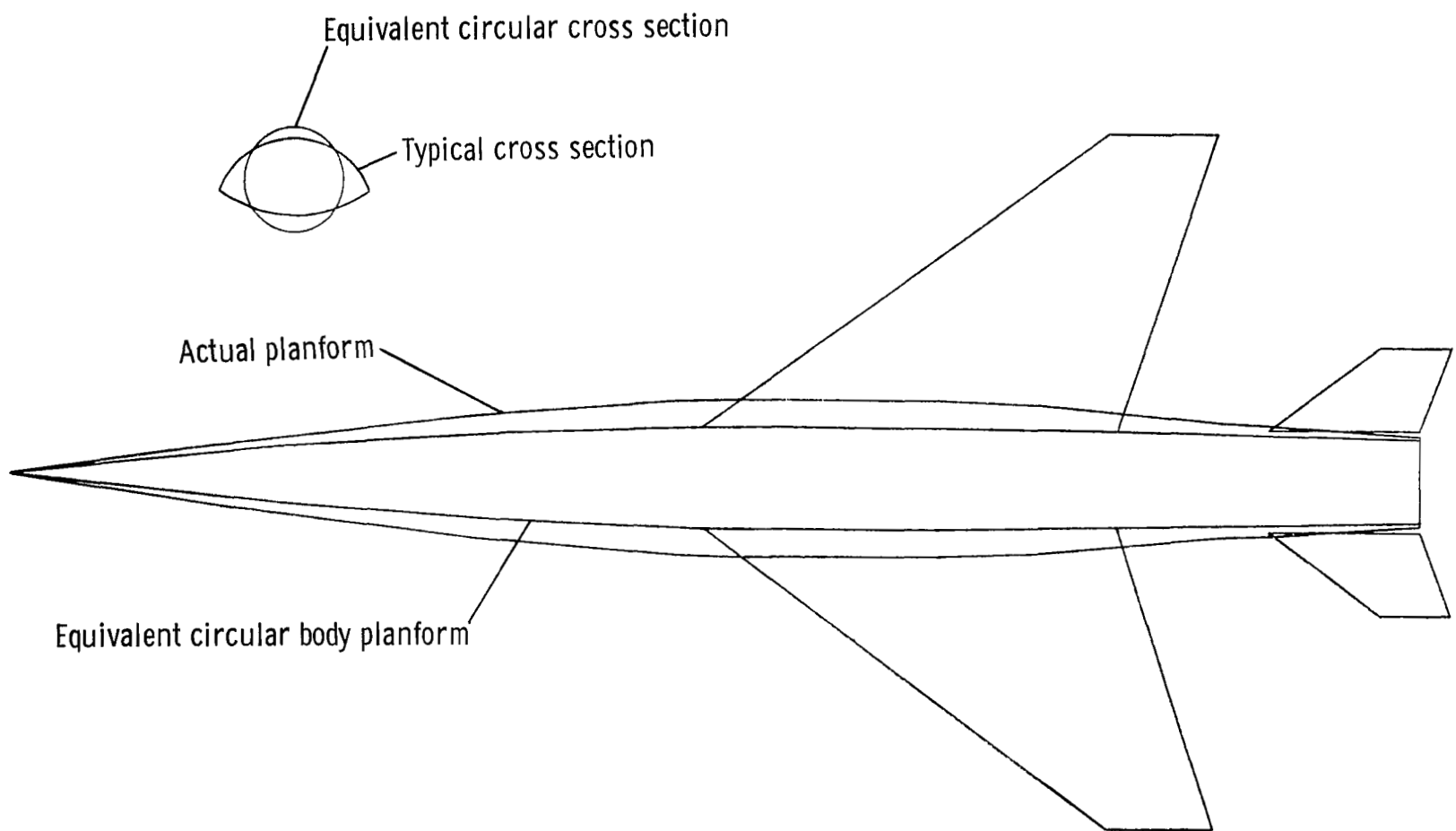


Figure 32.- Actual and equivalent circular fuselage planforms for BW<sub>1</sub>H<sub>1</sub>V<sub>C</sub> configuration.

1. Report No. <b>NASA TP-1767</b>	2. Government Accession No.	3. Recipient's Catalog No.	
4. Title and Subtitle  <b>EXPERIMENTAL AND THEORETICAL AERODYNAMIC CHARACTERISTICS OF TWO HYPERSONIC CRUISE AIRCRAFT CONCEPTS AT MACH NUMBERS OF 2.96, 3.96, AND 4.63</b>	5. Report Date <b>December 1980</b>		
6. Performing Organization Code <b>505-31-73-01</b>	7. Author(s)  <b>Jimmy L. Pittman and Gregory D. Riebe</b>	8. Performing Organization Report No. <b>L-13868</b>	
9. Performing Organization Name and Address  <b>NASA Langley Research Center Hampton, VA 23665</b>	10. Work Unit No.	11. Contract or Grant No.	
12. Sponsoring Agency Name and Address  <b>National Aeronautics and Space Administration Washington, DC 20546</b>	13. Type of Report and Period Covered <b>Technical Paper</b>	14. Sponsoring Agency Code	
15. Supplementary Notes			
16. Abstract  The longitudinal and lateral-directional aerodynamic characteristics for two Mach 5 cruise aircraft concepts have been determined for test Mach numbers of 2.96, 3.96, and 4.63. Estimates from hypersonic impact theory and first-order supersonic linearized theory were compared with data to indicate the usefulness of these methods. The method which applied tangent-cone empirical theory to the body and tangent-wedge theory to the wings and to the horizontal and vertical tails provided the best estimates. Comparisons for the configuration buildup showed, however, that the estimates for the various components could be significantly different from the data. The tangent-cone empirical theory applied to all components showed consistently poor agreement with data, and the linear theory estimates were accurate only for lift coefficient and drag coefficient at low angles of attack.			
17. Key Words (Suggested by Author(s))  <b>Supersonic aerodynamics Hypersonic aircraft Computational methods Flow-through nacelles</b>	18. Distribution Statement  <b>Unclassified - Unlimited</b>		
19. Security Classif. (of this report)  <b>Unclassified</b>	20. Security Classif. (of this page)  <b>Unclassified</b>	21. No. of Pages <b>113</b>	22. Price <b>A06</b>
<b>Subject Category 02</b>			

For sale by the National Technical Information Service, Springfield, Virginia 22161

NASA-Langley, 1980

National Aeronautics and  
Space Administration

Washington, D.C.  
20546

Official Business  
Penalty for Private Use, \$300

THIRD-CLASS BULK RATE

Postage and Fees Paid  
National Aeronautics and  
Space Administration  
NASA-451



1 1 1U,A, 112880 S00903DS  
DEPT OF THE AIR FORCE  
AF WEAPONS LABORATORY  
ATTN: TECHNICAL LIBRARY (SUL)  
KIRTLAND AFB NM 87117

**NASA**

POSTMASTER: If Undeliverable (Section 158  
Postal Manual) Do Not Return

---